

Copyright

by

Peter Basilio Zamora

2015

**The Dissertation Committee for Peter Basilio Zamora Certifies that this is the
approved version of the following dissertation:**

**MIXING DYNAMICS OF GROUNDWATER-SEAWATER SYSTEMS
AT THE LAND-OCEAN INTERFACE**

Committee:

M. Bayani R. Cardenas, Supervisor

John M. Sharp

Philip C. Bennett

James W. McClelland

Perran L. M. Cook

**MIXING DYNAMICS OF GROUNDWATER-SEAWATER SYSTEMS
AT THE LAND-OCEAN INTERFACE**

by

Peter Basilio Zamora, B.S.;M.S.

Dissertation

Presented to the Faculty of the Graduate School of

The University of Texas at Austin

in Partial Fulfillment

of the Requirements

for the Degree of

Doctor of Philosophy

The University of Texas at Austin

August 2015

Acknowledgements

I thank my advisor, committee members, and research group for their insights, guidance, support, and suggestions over the course of this research. I specifically thank Bayani Cardenas for his mentorship and patience. Special thanks to Kevin Befus for the discussions and occasional MATLAB advice. I thank my colleagues Kuldeep Chaudhary, Lichun Wang, John Warden, Wen Deng, Lizhi Zheng, Matt Kaufman, Eric Gultinan, Alyse Briody, Raquel Flinker, Travis Swanson, Mike Kanarek, and John Nowinski for constructive feedback during presentations and discussions. Field data and sample collection would not have been possible without the help of Nino Paulo Zamora, Raymond Rodolfo, Mark Lapus, Isabel Senal, Jack Rengel, Wei Wen Wong, Victor Evrard and Vera Eates. Special thanks to Perran Cook, Isaac Santos, Fernando Siringan and Ed Gomez for their collaboration and logistical assistance. I thank my family and my Texas family for their unwavering support, encouragement, and patience.

This research was funded through student grants from the Geological Society of America and the University of Texas at Austin-Geology Foundation.

MIXING DYNAMICS OF GROUNDWATER-SEAWATER SYSTEMS AT THE LAND-OCEAN INTERFACE

PETER BASILIO ZAMORA, PH.D.

The University of Texas at Austin, 2015

Supervisor: M. BAYANI R. CARDENAS

Subterranean estuaries are important coastal features where dissolved materials from groundwater and seawater can react and transform. Hence, they affect the quantity and quality of fluid and chemical fluxes across the sediment-water interface. Local geologic and hydrologic heterogeneities in coastal systems can modify this interaction and fluxes. I investigate groundwater-seawater mixing dynamics and groundwater discharge in geographically relevant coastal systems where groundwater upwells through permeable sediments, under small river estuaries, and at a site susceptible to episodic rise in the water table with heavy rainfall.

Using numerical simulations of variably-saturated density-dependent flow in porous media coupled with solute transport, I show that freshwater plumes and seawater recirculation cells develop where groundwater upwells from discrete freshwater outlets. Mixing zones that form along the freshwater plume-recirculation cell boundary change with tides and seasonal variations in the strength of the upwelling groundwater. Brackish fluxes increase with the waning strength of groundwater upwelling and sediment thickness but to a much lesser extent. Freshwater fluxes increase with stronger upwelling.

Using electrical resistivity (ER) as salinity proxy complemented with groundwater head and temperature profile measurements, I find cut banks to be persistent groundwater

discharge sites whereas point bars are predominant locations of hyporheic exchange underneath small river estuaries. These trends are consistent on an estuary-wide scale where sinuous reaches show high ER indicating groundwater discharge hotspots while straighter channel segments have resistivities similar to surface water suggesting the dominance of hyporheic exchange.

Time-series porewater salinity profiles along a beach cross section directly showed the flushing and freshening of the intertidal subterranean estuary within a 24 hour period. Subsurface temperature profiles, hydraulic head measurements, and ^{222}Rn in seawater concentration indicate consequent elevated groundwater discharge towards the coast. These demonstrate that episodic rainfall can rapidly elevate the groundwater table in permeable beach sediments which affects the chemical and thermal regime of the subterranean estuary. This can potentially deliver materials and energy cycled within the mixing zone in episodic doses to coastal areas akin to flooding of rivers and estuaries.

Table of Contents

List of Tables	xi
List of Figures	xii
Chapter 1: Introduction	1
1.1 MOTIVATION.....	1
1.2. THESIS ORGANIZATION.....	4
Chapter 2: Groundwater-seawater mixing dynamics and fluxes through sediments overlying zones of discrete seepage	6
2.1 ABSTRACT.....	6
2.2. INTRODUCTION	6
2.3. METHODS.....	9
2.3.1. Tracing SGD with ²²² Rn and seepage measurements	10
2.3.2. Numerical flow and transport simulations	13
2.3.2.1. Boundary and initial conditions and model scenarios	16
2.4. RESULTS	20
2.4.1. Rn-based seepage rates and seawater salinity.....	20
2.4.2. Direct seepage measurements and porewater salinity.....	23
2.4.3. Numerical simulation results	24
2.4.3.1. Case 1.....	25
2.4.3.2. Case 2.....	27
2.4.3.3. Case 3.....	29
2.4.3.4. Case 4.....	31
2.4.3.5. Porewater fluxes.....	33
2.5. DISCUSSION	36

2.5.1. Subsurface flow and mixing features.....	36
2.5.2. Effect of tides	37
2.5.3. Effect of outlet head variability	38
2.5.4. Influence of sediment thickness.....	39
2.5.5 Relationship of subsurface flow features and porewater fluxes	40
2.6. SUMMARY AND CONCLUSIONS	41
2.7 ACKNOWLEDGEMENTS.....	42
Chapter 3: Controls on the dynamics of the subterranean estuary and hyporheic zone of a river estuary determined from hydraulic, thermal and geophysical monitoring	43
3.1. ABSTRACT.....	43
3.2. INTRODUCTION	44
3.3. STUDY SITE AND METHODS	47
3.3.1. Study site background.....	47
3.3.2. Field methods and data processing	50
3.4. RESULTS	54
3.4.1. Subsurface temperature profiles	54
3.4.2. Groundwater hydraulic heads, Darcy fluxes, and salinity	56
3.4.3. Subsurface ER results	59
3.4.3.1. Time-lapse cross-channel underwater ER	59
3.4.3.2. Continuous resistivity profiling results.....	60
3.5. DISCUSSION	62
3.5.1. Constraining ER interpretation with forward modeling	62
3.5.2. Channel-scale porewater salinity	62
3.5.3 Estuary-scale porewater salinity	65

3.5.4. Controls on salinity of the subterranean estuary	66
3.5.5. Implications for material transformation	69
3.6. SUMMARY AND CONCLUSION	69
3.7. ACKNOWLEDGEMENTS.....	70
Chapter 4: Flooding of a subterranean estuary with episodic rainfall.....	71
4.1. ABSTRACT.....	71
4.2. INTRODUCTION	71
4.3. FIELD METHODS	73
4.3.1. Porewater Sampling.....	73
4.3.2. Hydraulic Head and Temperature Measurements.....	75
4.3.3. Tracing SGD with ²²² Rn	76
4.4. RESULTS	77
4.4.1. Porewater Salinity.....	77
4.4.2. Groundwater Heads and Potential Fluxes.....	79
4.4.3. Subsurface Temperature Profiles	82
4.4.4. Rn-based Seepage Rates	84
4.5. DISCUSSION	85
4.5.1. Subsurface Flow and Sources	85
4.5.2. Enhanced Coastal Groundwater Discharge with Episodic Rainfall.....	86
4.5.3. Subsurface Salinity Distribution and Flushing of the Intertidal Mixing Zone	87
4.6. SUMMARY.....	89
4.7. ACKNOWLEDGEMENTS.....	90
Chapter 5: Biogeochemical Implications	91
5.1 DISCRETE GROUNDWATER UPWELLING ZONES	92

5.2 SUBTERRANEAN ESTUARY UNDER AN ESTUARY	95
5.3 FLUSHING OF THE INTERTIDAL SALINE PLUME	99
Chapter 6: Summary	101
6.1 SYNTHESIS	101
6.2 KEY FINDINGS AND RECOMMENDATIONS	102
REFERENCES.....	103

List of Tables

Table 2.1:	Parameters and coefficients used in the numerical simulation	15
Table 2.2:	Tidal constituents, frequencies, and amplitudes used in the simulation ...	17
Table 3.1:	Hydraulic conductivity values from slug tests at each piezometer.....	58

List of Figures

Figure 2.1:	Study area and location of seepage meters and radon monitoring.....	12
Figure 2.2:	Conceptual model and simulated domain showing boundary conditions.	17
Figure 2.3:	Tide, salinity, and ²²² Rn trends	21
Figure 2.4:	Submarine groundwater discharge measurements from manual seepage meters.....	23
Figure 2.5:	Case 1 numerical model results	26
Figure 2.6:	Case 2 numerical model results	28
Figure 2.7:	Case 3 numerical model results	30
Figure 2.8:	Case 4 numerical model results	32
Figure 2.9:	Temporal flux trends from the simulated transient models	34
Figure 3.1:	Aerial image of Werribee Estuary and study reach	48
Figure 3.2:	In-stream piezometer stations and ER transect line.....	51
Figure 3.3:	Petrophysical model with the inverted resistivity section and model resolution.....	54
Figure 3.4:	Temperature time-series logs in in-stream piezometers	56
Figure 3.5:	January estuarine stage variation and in-stream piezometer water levels.	57
Figure 3.6:	Calculated vertical groundwater fluxes from in-stream piezometers	58
Figure 3.7:	Cross-channel ER profiles at different estuary stage.....	60
Figure 3.8:	Estuary-wide CRP for January and August 2012.	61
Figure 3.9:	Conceptual model of the porewater salinity dynamics	68
Figure 4.1:	Transect profile, piezometer, and thermistor array locations	74
Figure 4.2:	Porewater salinity profiles during neap tide with rain events.....	78
Figure 4.3:	Porewater salinity profiles during spring tide.....	79

Figure 4.4:	Piezometric heads and Darcian fluxes through time.....	80
Figure 4.5:	Interpolated groundwater heads through time.	81
Figure 4.6:	Interpolated vertical fluxes through time.	82
Figure 4.7:	Subsurface and seawater temperature profiles.....	83
Figure 4.8:	Radon concentration in seawater and net groundwater discharge	84
Figure 4.9:	Conceptual model during fair-weather and after strong rain events.....	88

Chapter 1: Introduction

1.1 MOTIVATION

Our perception of the importance of fluid interaction in the subsurface and associated fluid exchange near the land-ocean boundary has evolved with our understanding of its impacts and the processes that underpin it. In the old days, this interaction was mainly observed as peculiar submarine springs which were novel sources of freshwater to sailors. Even with the early knowledge of hydrogeology, these were known to be groundwater preferential flow paths through geologic strata extending beyond the shoreline [Sonrel, 1886]. Our more evolved understanding of fluid dynamics and flow in porous media in the last century turned the focus to the problem of larger scale saltwater wedges invading our coastal aquifers [Du Commun, 1828; Badon Ghijben, 1889; Herzberg, 1901; Wentworth, 1948; Cooper, 1959; Glover, 1959; Kohout, 1960]. Aided by advances in geophysics and computational power in the last few decades, the attention turned to temporally shorter and smaller scale processes such as the dynamics of freshwater-seawater mixing in the shallow subsurface and the potential environmental impacts of faster fluid exchange at the sediment-water interface (SWI).

The ubiquitous yet unseen phenomenon of groundwater discharge, more popularly Submarine Groundwater Discharge (SGD), contributes significant amount of dissolved materials that can influence the quality of our coastal waters [Johannes, 1980; Moore, 1996; Burnett *et al.*, 2001]. Prior to discharge, fresh, brackish, and saline groundwater transit through subsurface mixing zones or subterranean estuaries (STE) where both terrestrial and oceanic materials can react and transform [Moore, 1999]. Dynamic forcing mechanisms on both the terrestrial and oceanic end as well as the density difference between freshwater and saltwater drives subsurface mixing and fluid exchange across the

sediment-water interface at different spatial and temporal scales. Tides, waves, and episodic changes in sea-level influence mixing in the shallow STEs at diurnal to fortnightly time scales [Robinson *et al.*, 2007b, 2007c; Abarca *et al.*, 2013; Heiss and Michael, 2014]. Seasonal variations in recharge affect seaward groundwater gradients which allows the seasonal movement of the deeper STE or more popularly the “freshwater-saltwater interface” [Hubbert, 1940; Cooper, 1959; Michael *et al.*, 2005]. The influence of these driving forces is modulated by intrinsic properties, permeability, porosity, and storage of the aquifer.

Local geologic, geomorphologic, and hydrologic variability can modify the flow and fluxes at the land-ocean boundary at geographically relevant spatial and temporal scales. Geologic features including interbedded permeable-impermeable layers, fractures, and dissolution conduits create preferential flow paths which can focus groundwater flow and create freshwater discharge hotspots along coastal outcrops. Buried outlets can create groundwater upwelling zones that can promote freshwater-saltwater mixing in the subsurface. Shoreline geomorphology can modify the spatial distribution and strength of seaward groundwater flow by focusing flow in bay heads and diverging flow along headlands. The dynamic flow direction and velocity of coastal waters, especially in estuaries, affect hyporheic flow paths and deeper circulations in adjacent aquifers. Tidal and seasonal salinity variations also affect buoyancy driven subsurface mixing and fluid exchange. The mode of delivery of freshwater input in coastal rivers and recharge through beach and coastal watershed also affects fluid interactions and fluxes at the land-ocean boundary.

Seminal studies on STEs and SGD mostly consider an unconfined aquifer with a seasonally controlled seaward groundwater flow discharging at or near the shoreline. However, more studies report discrete upwelling sources of SGD though preferential

groundwater flow paths. Upwelling of groundwater in sediments can occur anywhere between the shoreline and the outer shelf where breaks in the aquifer confining unit or outflows of preferential groundwater flow paths leak groundwater into overlying sediments [Moore and Wilson, 2005; Bratton, 2010]. The presence of these buried groundwater outlets promotes subsurface mixing and formation of an STE beyond the shoreline and out into the shelf environment which can impact the biogeochemistry of the overlying offshore waters.

STEs underneath surface estuaries are unique mixing zones controlled by both fluvial and oceanic forces routed through bedform to channel scale morphologic features. The spatial variability of fresh groundwater discharge along estuarine shorelines can be influenced by shoreline curvature where flow is focused inside the bends and diverged along headlands [Linderfelt and Turner, 2001; Smith and Turner, 2001]. Current flow over different channel bedforms on the other hand controls shallow subsurface hyporheic exchange [Boano et al., 2014]. These scenarios are complicated by the bidirectional flow in estuaries and variability of surface water salinity over daily to seasonal time scales. This complex interaction between estuarine surface water and groundwater can influence subsurface transformation of dissolved materials as well as the timing and spatial distribution of benthic fluxes along the estuarine SWI.

STEs can be perturbed by episodic oceanic and terrestrial events that can disrupt or displace their biogeochemical functions. Sudden rises in sea level due to storms has been observed to elevate the seaside hydrostatic head which promotes the infiltration of seawater into the STE [Moore and Wilson, 2005; Anderson and Lauer, 2008; Smith et al., 2008; Wilson et al., 2011]. On the terrestrial end, perturbations like freshwater flooding from rapid recharge events such as rainstorms are rarely observed and studied. Although the overall contribution of groundwater discharge on the quality of coastal waters is maintained

through slower-longer term processes like seasonal recharge cycles [Michael et al., 2005], events like algal blooms have been linked with increased inputs of groundwater related to episodic heavy rainfall [Hu et al., 2006]. Thus, the frequency of these instantaneous chemical doses released through coastal groundwater discharge can substantially impact the quality of coastal waters and have persistent consequences.

In this thesis, I investigate the effects of local geologic and hydrologic heterogeneity on groundwater-seawater mixing dynamics in STEs and fluid fluxes across the sediment-water interface. I examine the influence of upwelling fresh groundwater from discrete seepage zones on the coastal STE and the link between bidirectional flow, variable surface water salinity, and channel morphology on the porewater salinity of adjacent STE's. I also and monitored an intertidal STE as it is flooded with fresh groundwater from episodes of heavy rainfall.

1.2. THESIS ORGANIZATION

Each chapter, excluding Chapters 1, 5, and 6, has been prepared or submitted for journal publication and has its own abstract, introduction, methods, results, discussion, summary, and references. Descriptions of main thesis Chapters 2, 3, and 4 are introduced in the succeeding paragraphs with highlights of important results. Chapter 5 is a synthesis of the main chapters and includes recommendations and future research directions. The biogeochemical implications associated with different aquifer conditions and coastal water scenarios are discussed in Chapter 6.

Chapter 2 examines groundwater-seawater mixing dynamics and fluxes in sediments influenced by groundwater upwelling. Using variably-saturated density-dependent numerical simulations of flow in porous media coupled with solute transport, I found that seawater recirculation cells and STEs along the plume-recirculation cell

boundary develop where there are freshwater upwelling plumes. The STEs widened with tides and seasonal changes in the strength of the upwelling groundwater. Brackish water fluxes from the STEs increased with the waning strength of groundwater upwelling whereas freshwater fluxes increased with upwelling strength. Sediment thickness increased the width of the STE but to a lesser extent relative to tides and upwelling variability.

Chapter 3 explores the influence of channel planimetry and estuarine surface water hydrodynamics on the hyporheic zones and STE of a small river estuary. By monitoring in-stream piezometric heads, subsurface temperature profiles, and subsurface salinities using electrical resistivity as proxy, I show that the cut bank along a meander reach is a zone where fresh groundwater discharge is persistent whereas the point bar is where hyporheic exchange predominates. This reach scale variability was observed on a larger scale estuary-wide ER survey where I find that sinuous reaches have higher ER values indicating groundwater discharge hotspots whereas straighter channel segments were more hyporheic flow dominated.

In Chapter 4, I observed an STE as it was flooded with freshwater from episodic rainfall. Using porewater salinity profiles, groundwater head measurements, and vertical temperature profiles along a shoreline perpendicular transect monitored through periods with and without rain events, I found that the intertidal mixing zone was flushed within a 24 hour period directly indicated by freshening porewater through time. The rapid recharge was observed as a sudden rise in groundwater head quickly followed by a slow recession. The intertidal STE is known to wane typically on fortnightly to seasonal time scales.

Chapter 2: Groundwater-seawater mixing dynamics and fluxes through sediments overlying zones of discrete seepage

2.1 ABSTRACT

Submarine groundwater discharge near discrete groundwater upwelling zones is not well understood. A field study was conducted supported by numerical flow and transport simulations tuned to the study site to understand this phenomenon. Field observations along a shoreline perpendicular transect included point measurements using seepage meters and integrated measurements using the natural groundwater tracer ^{222}Rn . Seepage and salinity measurements showed fluxes in the subtidal region which are as high and as fresh as those from the intertidal zone. Seepage rates and salinities also followed tidal trends. 2D numerical simulations of coupled groundwater flow and salt transport along a beach-ocean cross section with discrete freshwater outlets showed the development of freshwater upwelling plumes with seawater recirculation cells forming outside of the plumes. Mixing zones that discharge at the sediment water interface formed where the plumes meet the recirculating seawater cells. The upwelling freshwater plumes widened with a higher constant upwelling strength but this did not affect the width of the mixing zones. Models accounting for tides and seasonally variable upwelling rates have wider mixing zones and a wider range of porewater fluxes across the sediment-water interface. Sediment thickness had a minor effect on the width of both the freshwater plumes and the mixing zones.

2.2. INTRODUCTION

The relative importance of groundwater (GW)-seawater (SW) interaction on the chemistry of porewater released through submarine groundwater discharge has long been recognized [*Johannes, 1980; Charette, 2002; Slomp and Van Cappellen, 2004; Charette et al., 2005; Boehm et al., 2006; Charette and Sholkovitz, 2006; Kroeger et al., 2006, 2007;*

Loveless and Oldham, 2010]. Benchmark studies on the dynamics of subsurface mixing mostly considered unconfined aquifers with seaward groundwater flow which discharge at or near the shoreline. However, GW-SW mixing dynamics in porous materials receiving groundwater seepage from discrete preferential groundwater flow paths have received much less attention.

Albeit less ubiquitous than the typical along-shore groundwater discharge zones, sediment mantled groundwater outflows in coastal areas can be present anywhere between the shoreline and out into the outer shelf environment [*Moore and Wilson, 2005; Bratton, 2010*]. They can occur in places with submarine exposures of fractured or faulted aquifer confining units [*Burnett et al., 2001; Mälkki, 2003; Shaban et al., 2005; Bokuniewicz et al., 2008; Peng et al., 2008*], layered sedimentary rock aquifers dipping seaward with coastal outcrops [*Shaban et al., 2005; Lofi et al., 2013*], modern and paleo-rivers with submarine extensions [*Stieglitz, 2005; Mulligan et al., 2007*], lava tubes and lava sheet gaps in volcanic islands [*Peterson et al., 2009; Povinec et al., 2012; Ramessur et al., 2013*], coastal karst terrains with submarine conduits and outlets [*Fleury et al., 2007; Null et al., 2014*] as well as younger reefs undergoing incipient eogenetic karstification [*Fleury et al., 2007; Cardenas et al., 2010; Povinec et al., 2012; Null et al., 2014*]. The presence of these groundwater outlets brings terrestrially derived dissolved materials anywhere beyond the shoreline which can in turn impact the biogeochemistry of the overlying waters.

Permeable marine sediments underlain by discrete groundwater outlets are bounded by oceanic forces at the sediment-water interface and terrestrial groundwater at the discrete outlet. Onshore recharge controls the input of freshwater routed through preferential flow paths and into the overlying sediments. Along the SWI, currents and sea level oscillations associated with tides as well as wave action in shallow waters influence seawater infiltration [*Robinson et al., 2007c; King et al., 2009*]. These external drivers are all

modulated by the geometry and hydraulic properties of the sediments where groundwater and surface water interact. While the influence of these external forces and sediment hydraulic properties on freshwater-saltwater mixing has been extensively studied in unconfined coastal aquifers [Cooper, 1959; Volker and Rushton, 1982; Ataie-Ashtiani *et al.*, 1999; Robinson *et al.*, 2007c; Abarca and Prabhakar Clement, 2009; Lu *et al.*, 2009], systems which receive freshwater inflow from underlying groundwater preferential flow paths are not well understood. This work looks into the effect of various external drivers primarily fluctuations in the strength of groundwater outflow and tidal oscillations on GW-SW interaction and SGD through numerical simulations. Emphasis is given on the effect of these forcing mechanisms on the geometry, position, and fluxes across the SWI above the mixing zones where material transformations are likely to occur. Additionally, the influence of sediment thickness on the mixing dynamics is also explored.

Previous work on this type of system focused on mapping and quantifying porewater fluxes using shallow porewater vertical profiles, geophysical surveys, and seepage measurements. Povinec *et al.* [2012] reported rapid decrease in sediment bulk electrical conductivity towards a submarine spring associated with a strong upwelling of freshwater. In the same study, far field of the spring, they also observed a rapid response in the sediment bulk electrical conductivity and highly variable seepage rates with onshore precipitation in an area underlain by lava tubes. Bokuniewicz *et al.* [2008] also reported variable rates of SGD in Flamengo Bay, Brazil, which they attributed to fracture clustering and the effects of the underlying bedrock surface topography under a thin sediment cover. Rapid changes in bulk sediment electrical conductivity towards the point freshwater seepage source were also reported at the same site in Flamengo Bay [Stieglitz *et al.*, 2008]. Although these methods are useful in identifying point sources and magnitudes of SGD, the coarser resolution limits further analysis of the underlying mixing dynamics and

associated chemical fluxes which can occur at a finer scale. The gaps in studies based solely on field observations can be addressed by using numerical modelling. Although the veracity of numerical model results rely heavily on accurate representation of the site properties and pertinent boundary conditions, reasonable assumptions can yield valuable explanatory insights on the processes underlying field observations. This work combines numerical simulations with field measurements to understand GW-SW mixing dynamics in this environment.

The field investigation was conducted in the town of Bolinao, a peninsula in Pangasinan province in the northwestern Philippine archipelago, where freshwater submarine springs are present (Figure 2.1). The area is a major mariculture site especially for milkfish (*Chanos chanos*), a popular fish in the Philippines, and is close to a large protected zone of marine biodiversity. It also hosts an experimental research site for reef restoration. In the last decade, Bolinao has experienced several fish kills associated with algal blooms that were attributed to eutrophication from aggressive fish feeding [Azanza *et al.*, 2005; San Diego-McGlone *et al.*, 2008]. Adding to this problem is a projected increase in coastal population [McManus, 1997] which will likely lead to groundwater nutrient enrichment especially since all domestic waste is disposed in unregulated septic systems [Lapointe *et al.*, 1990].

2.3. METHODS

A field study was conducted in April 22-24, 2010 to assess the magnitude and temporal trends of fluxes across the SWI in an area receiving groundwater seepage from underlying geologic structures. The site is located along a pocket beach underlain by uplifted Plio-Pleistocene coralline limestone [MGB, 1974; De Ocampo, 1983; Maemoku and Paladio, 1992; Ramos and Tsutsumi, 2010] where submarine freshwater springs are

present. Annual rainfall is about 2500 mm which is mainly delivered by storms during the wet season [Rivera, 1997; Rollón *et al.*, 2003]. The 1 km² watershed does not have a well-developed surface water drainage except for an ephemeral stream east of the study site (Figure 2.1). The stream is active only during the passage of strong rain events. Groundwater recharge at the study site can occur in the same manner as tropical Pleistocene limestone aquifers where rainwater percolates through fractures and shafts in the karstified marine terraces [Jones *et al.*, 2000]. Anecdotal accounts suggest that water level in caves rise after rain events and that groundwater levels are generally higher during the rainy season. Locals also observe stronger flow from the freshwater springs along the beach with rain events which suggests a connection between recharge flow paths to conduits that feed the springs. Freshwater springs close to the beach-ocean transect are present year round and are most conspicuous during spring low tide (anecdotal accounts).

2.3.1. Tracing SGD with ²²²Rn and seepage measurements

Radon (²²²Rn) was used as proxy for the total groundwater discharge, fresh and recirculated, owing to its significant enrichment in groundwater. ²²²Rn in seawater was measured at the end of the seepage meter transect line in about 2-meter deep water (Figure 2.1). ²²²Rn concentration was continuously measured using a radon-in-air monitor (RAD7) attached to a chamber where seawater is sprayed and degassed [Burnett and Dulaiova, 2003]. The pump used to feed seawater to the chamber was submerged 1 m below the water surface where pumping was maintained at a rate of 4 liters per minute. The degassing chamber was equipped with a thermistor that logs the water temperature sprayed from the top of the chamber. ²²²Rn in water was measured every 30 minutes for 3 days representing two tidal cycles. Water temperature and water depth were also monitored using an In-situ TD logger installed 2 cm above the seafloor directly underneath the submersible pump.

The sensor was set at a logging interval of 2 minutes. Integrated groundwater fluxes through time were calculated using the method outlined in Burnett and Dulaiova [2003]. Briefly, ^{222}Rn inventories, the average radon concentration within a specified time interval multiplied by depth, were calculated at 3-hour intervals through:

$$\text{Inventory} \left[\frac{\text{Bq}}{\text{m}^2} \right] = \text{Rn} \left[\frac{\text{Bq}}{\text{m}^3} \right] \times Z [\text{m}] \quad (2.1)$$

The inventories were normalized by accounting for water level changes with tides where incremental change in depth at every time interval was added or subtracted with flooding or ebbing tides respectively through:

$$\text{Normalized Inventory} \left[\frac{\text{Bq}}{\text{m}^2} \right] = \text{Inventory} - \text{Rn} \left[\frac{\text{Bq}}{\text{m}^3} \right] \times \Delta Z [\text{m}] \quad (2.2)$$

Above, Rn is the measured radon concentration, Z and ΔZ is the water depth and incremental change in depth with tide respectively. Field condition was calm during the measurement hence atmospheric losses of ^{222}Rn were deemed to be minimal.

The net ^{222}Rn flux with time was calculated from the difference in the normalized inventory at given time intervals via:

$$\text{Net Rn Flux} \left[\frac{\text{Bq}}{\text{m}^2\text{s}} \right] = \frac{\Delta \text{Normalized Inventory} \left[\frac{\text{Bq}}{\text{m}^2} \right]}{\Delta t [\text{s}]} \quad (2.3)$$

^{222}Rn dilution due to mixing with ^{222}Rn depleted offshore waters, referred to here as mixing loss, was accounted for by adding the highest negative ^{222}Rn flux to the calculated net fluxes. The presence of measurable ^{222}Rn concentration suggest that benthic flux can compensate dilution which also suggest that the flux estimates are conservative

[Burnett and Dulaiova, 2003]. Finally, net groundwater discharge was calculated by dividing the Rn fluxes with groundwater ^{222}Rn concentration:

$$Flux \left[\frac{\text{m}}{\text{s}} \right] = \frac{Net\ Flux \left[\frac{\text{Bq}}{\text{m}^2\text{s}} \right]}{Groundwater\ Rn \left[\frac{\text{Bq}}{\text{m}^3} \right]} \quad (2.4)$$

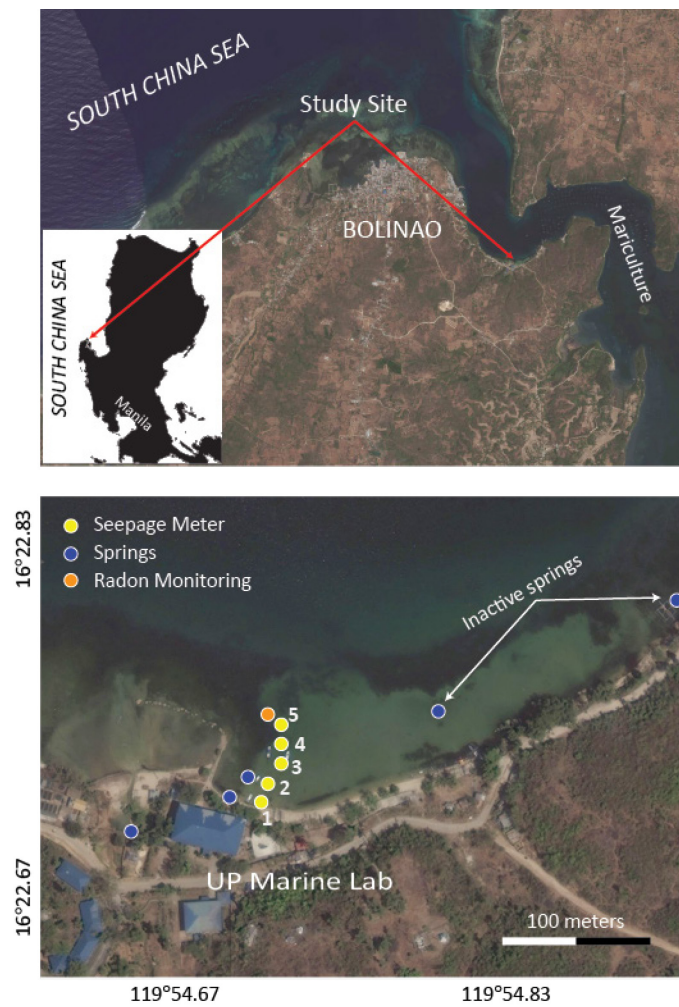


Figure 2.1. Study area (top panel) showing the watershed boundary and location of seepage meters and radon monitoring (bottom panel).

Spatial variation in groundwater fluxes through time were measured directly at points along a beach-ocean transect using Lee-type seepage meters [Lee, 1977] with 5 liter polyethylene collection bags. The transect length is about 100 m perpendicular to the high tide line. Two sets of seepage meters were installed in the intertidal and subtidal zone and one was installed right at the low tide line (Figure 2.1). The seepage meters were allowed to equilibrate for 24 hours prior to bag installation and sample collection. Seepage volumes were measured using a graduated cylinder. Salinity was measured from the seepage meter samples using a portable conductivity meter to determine the relative proportions of fresh groundwater and recirculated seawater discharge. Water samples from the seepage meters and from the springs were also collected and analyzed for ^{222}Rn . The time of sampling was noted to correct for ^{222}Rn decay from collection to analysis.

2.3.2. Numerical flow and transport simulations

The GW-SW mixing dynamics in sediment overlying groundwater seepage outlets (Figure 2.2) was modeled numerically using variably-saturated, density-dependent, porous media flow based on Richards Equation coupled with the advection-dispersion equation for solute transport:

$$\rho \left(\frac{C_m}{\rho g} + S_e S \right) \frac{\partial P}{\partial t} + \nabla \cdot \rho \left(-\frac{k_s}{\mu} k_r (\nabla P + \rho g \nabla Z) \right) = Q_m \quad (2.5)$$

$$\frac{\partial}{\partial t} (\theta c) + \nabla \cdot \rho (cu) = \nabla \cdot ((D + D_d) \nabla c) \quad (2.6)$$

where Z and P are the elevation and pressure heads respectively. Richards Equation was used in this study to account for flow in the intertidal zone which is variably saturated with tidal fluctuations. k_s denotes the permeability of the sediments at full saturation calculated from hydraulic conductivity (K_h) estimates from in-situ slug tests:

$$k_s = \frac{\mu K_h}{\rho g} \quad (2.7)$$

whereas k_r is the relative permeability which depends on the degree of saturation S_e via:

$$k_r = S_e^{0.5} \left(1 - \left[1 - S_e^{1/m} \right]^m \right)^2 \quad (2.8)$$

C_m is the specific moisture capacity which relates changes in water content (θ), expressed as effective saturation (S_e) with the pressure head:

$$C_m = \frac{\alpha m}{1-m} (\theta_s - \theta_r) S_e^{1/m} \left[1 - S_e^{1/m} \right]^m \quad (2.9)$$

$$\theta = \theta_r + S_e (\theta_s - \theta_r) \quad (2.10)$$

The relationship of the relative permeability with pore pressure is defined through empirical parameters n and α described by the van Genuchten [1980] model whose functions are shown below:

$$S_e = \frac{1}{\left(1 + |\alpha P|^n \right)^m} \quad (2.11)$$

$$m = 1 - \frac{1}{n} \quad (2.12)$$

where n which is related to m in Equation 2.12 and α are the fitting parameters which describes the shape of both the moisture and relative permeability functions. θ_s and θ_r are the saturated and the residual water contents of the porous medium, respectively. The van Genuchten model parameters n , α , θ_s and θ_r used in the simulation were based on the loamy sand texture class which is similar to the beach sand deposit at the study site. Values were taken from the Rossetta program's [Schaap *et al.*, 2001] look up table for general textural

classes. Other pertinent parameter values in the flow and transport models are presented in Table 2.1.

Parameter	Symbol	Value/Range	Unit
Permeability	k_s	1.8×10^{-12}	m^2
Storage	S	7.5×10^{-8}	1/Pa
Fluid density	ρ	1000-1027	Kg/m^3
Dynamic viscosity	μ	0.001	Pa·s
Molecular diffusion coefficient	D	1×10^{-9}	m^2/s
Longitudinal dispersivity	α_x	0.5	m
Transverse dispersivity	α_y	0.05	m
Gravitational acceleration	g	9.8	$m\ s^{-12}$
Reciprocal air entry pressure	α	3.5	1/m
Pore-size distribution parameter	n	1.75	-
Residual water content	θ_r	0.05	-
Saturated water content	θ_s	0.4	-

Table 2.1. Parameters and coefficients used in the numerical simulation.

The rise and fall of sea level on top of the domain with tides results in changes to the total stress through time which could also affect the magnitude of groundwater fluxes [Reeves *et al.*, 2000; Gardner and Wilson, 2006]. I account for changes in the total stress with tidal trends through the term Q_m in the governing equation (2.5). Change in the total stress for a given model time-step is taken as the difference in the tidal elevation (H_T) for the given time-step and implemented in the simulation as the term Q_m [Reeves *et al.*, 2000;

Gardner and Wilson, 2006; Wilson and Gardner, 2006]. The total stress changes in the simulation were set to apply only to inundated areas.

The concentration of the conservative solute in the transport equation (2.6) is given by c whereas u represents the Darcy velocity based on the Richards Equation. D is the molecular diffusion coefficient for the solute and D_d is the classic mechanical dispersion coefficient which is the product of the average linear velocity and the dispersivity tensor characterized by α_x and α_y which are the dispersivities in the x and y direction, respectively [*Bear, 2012*]. Density variation in the pore fluid with changes in salt concentration during mixing was accounted for using a density function:

$$\rho = \rho_o + c \left(\frac{\rho_s - \rho_o}{c_s - c_o} \right) \quad (2.13)$$

where ρ_s , c_s and ρ_o , c_o are the density and normalized concentrations of seawater and freshwater respectively.

2.3.2.1. Boundary and initial conditions and model scenarios

Tides were accounted for in the simulation using a tidal function with known amplitudes and frequencies of tidal constituents in the study area [*Rivera, 1997*]:

$$H_T = \sum A_i \cos \omega_i t \quad (2.14)$$

where H_T is the hydraulic head due to tidal fluctuation along the SWI (Figure 2.2). A_i and ω_i represent the tidal amplitude and frequency of the tidal constituents respectively. The site has a mixed tidal system which is predominantly diurnal transitioning to semi-diurnal only at neap tide. Values of the dominant tidal constituents (O_1 , K_1 , M_2 , S_2) are summarized in Table 2.

Tidal Constituent	ω_i [Rad/Hr]	A_i [Rad]
O ₁	0.243351	0.2136
K ₁	0.262516	0.3372
M ₂	0.505868	0.1232
S ₂	0.523598	0.0386

Table 2.2. Tidal constituents with frequencies and amplitudes used in the simulation.

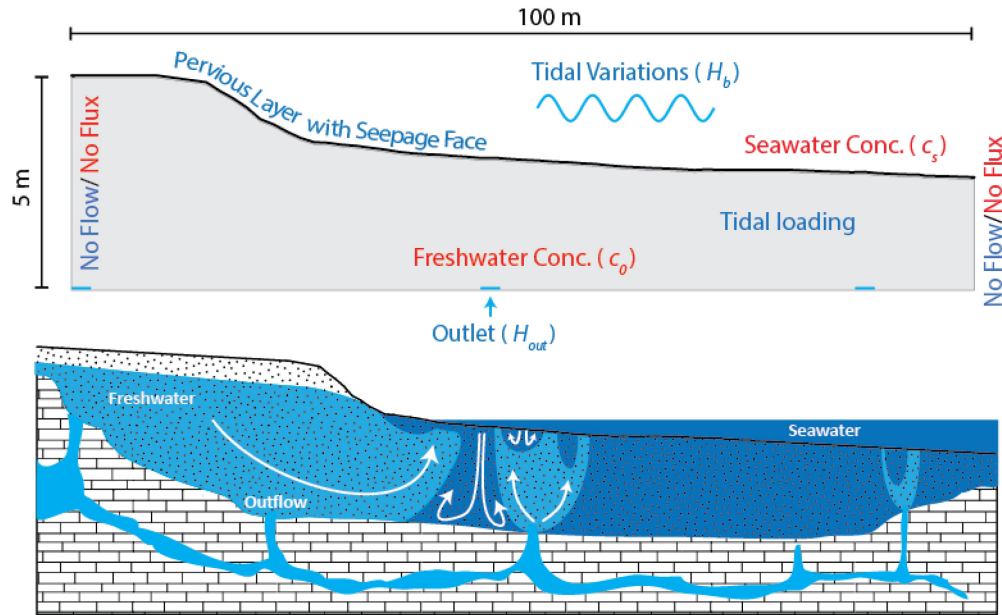


Figure 2.2. Conceptual model and simulated domain showing boundary conditions.

A head dependent flux boundary; similar to the general head boundary in Guo and Langevin [2002], was assigned to the top boundary representing the SWI (Figure 2.2) including the intertidal zone. This is implemented through the following:

$$-\mathbf{n} \cdot \rho \frac{k_s}{\mu} k_r (\nabla P + \rho g \nabla Z) = \rho R_b (H - H_b) \quad (2.15)$$

$$R_b = \frac{K_h}{L} \quad (2.16)$$

where H_b is the head in the external fluid (sea level) and H is the total head which is the sum of the pressure and elevation heads. R_b is a conductance term defined as the ratio of the saturated hydraulic conductivity (K_h) with a coupling length scale (L) [Chui and Freyberg, 2009]. n is the normal vector to the boundary. The flux along this boundary is determined by the difference between the head in the surface sediments (H) and sea level (H_b). Three scenarios can develop along the SWI with this type of boundary. When the tide is higher than the elevation head ($H_T > Z$), the flux along the SWI is determined by the head difference between the tidal elevation and the surface sediments. A seepage face along the SWI develops when the sediments are still saturated ($P \geq 0$) but with the tide level below the elevation head ($H_T < Z$). This is achieved by setting the external fluid head (H_b) along the surface of the seepage face equal to the elevation head ($H_b = Z$). This renders the pore pressure right at the seepage face to be at gauge level ($P = 0$) which properly represents the pressure along seepage face [Chui and Freyberg, 2009]. The flux along the seepage face in this case is the product of the pressure head and the conductance. When the SWI becomes unsaturated ($H < 0$) and the tide is lower than the elevation head ($H_T < Z$) it switches to a no flow boundary which is achieved by setting the value of R_b to zero when the pressure head becomes negative.

The freshwater outlets at the base of the model domain were also given a head dependent flux boundary condition. This allows both the heads and the fluxes along the boundary to adjust to dynamic changes in the subsurface [Konikow *et al.*, 2013]. The conductance (R_b) was set using the same settings with the SWI but with a head value dependent on relative strength of the outlet seepage which I will refer to here as the outlet head (H_{out}). The outlet head was also set to change with time to determine the effects of a dynamic water table associated with seasonal changes in recharge conditions.

An open boundary was assigned to the SWI where solute can flow in and out of the domain given by:

$$c = c_s \quad \mathbf{n} \cdot \mathbf{u} < 0 \quad (2.17)$$

$$-\mathbf{n} \cdot D_h \nabla c = 0 \quad \mathbf{n} \cdot \mathbf{u} \geq 0 \quad (2.18)$$

where D_h is the effective hydrodynamic dispersion coefficient (the sum of the molecular diffusion coefficient and mechanical dispersion coefficient), c_s is the concentration of the external fluid and c is the fluid concentration at the boundary. When the external fluid is entering the sediments (when tide level is higher than the head at the SWI), the solute concentration at the SWI takes the external fluid concentration (2.17). When the normal flux is outward of the domain, the dispersive flux is assumed to be insignificant relative to advection (2.18).

The conduits or fracture openings at the base of the domain were also assigned an open boundary condition but with the external fluid set to fresh water concentration ($c_s=c_o=0$). All other boundaries in the solute transport simulations were no-flux boundaries.

The model was created using a semi-rectangular domain with its upper boundary following the topographic profile generated from an elevation survey of a transect line perpendicular to shoreline (Figure 2.2). The section approximates the thickness (maximum of 5 m) and extent of the shoreface sand deposit overlying the fractured platform in the study area. In addition to the base case, thicknesses of 3 and 10 m were modeled to assess the effect of sediment thickness on the subsurface mixing dynamics. The model domain was discretized with a triangular mesh whose element size is less than twice the longitudinal dispersivity. The coupled partial differential equations were solved using the finite element package COMSOL Multiphysics®.

As it is relatively difficult to achieve convergence for steady state models of a variably-saturated density-dependent coupled flow and transport system, I conducted transient simulations at a longer time (spin up of 1000 days) for the non-tidal models and use the last time step as the quasi-steady state condition. Subsequent models with tides, varying sediment thickness and outlet head, were run for a total of 1030 days. The initial time step was set at 3 hours for the first 1000 days followed by a higher time resolution of 2 hours for the last 30 days. The results shown and analyzed are from the last 30 days of simulation. A total of 16 models representing different scenarios were simulated. Each model run took at least 48 wall-clock hours (for 5 models) for the simplest cases while simulations with dynamic boundaries took up to 33 wall-clock days (5 cases with tides, 3 cases seasonal water table and 3 with both dynamic boundaries). The models were run on a workstation with 32-cores and 256 Gb of RAM.

2.4. RESULTS

2.4.1. Rn-based seepage rates and seawater salinity

Seawater ^{222}Rn concentration measured across a tidal cycle ranged from 33 to 255 Bq m^{-3} (Figure 2.3) which is comparable to the previous ^{222}Rn measurements in the Philippines [Taniguchi *et al.*, 2008; Cardenas *et al.*, 2010; Senal *et al.*, 2011]. However, these values are lower compared to previous studies at known SGD sites with ^{222}Rn values ranging from 833 to 2.6×10^4 Bq m^{-3} [Dulaiova *et al.*, 2008]. The measurement error after correcting for moisture and temperature was reduced to 8.3 to 25 Bq m^{-3} . Although ^{226}Ra was not measured during the field campaign, more recent field measurements yielded values below 2.5 Bq m^{-3} including samples from springs discharging along the shoreline

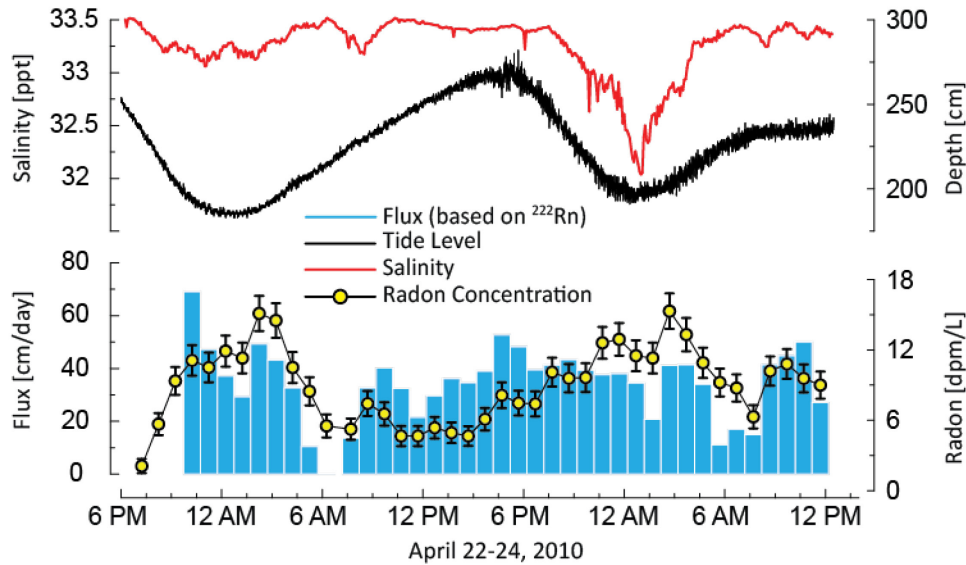


Figure 2.3. Tide and salinity trends at the end of the seepage meter transect line (location denoted by orange circle in Figure 2.1) during the 3 day field survey (upper panel). Measured Rn concentration in seawater through time and submarine groundwater discharge estimates based on 3 hour moving average Rn concentrations (lower panel).

which suggest low contribution from supported ^{222}Rn [I. Santos, pers. Comm.]. Survey conditions were relatively calm with a maximum wind speed of 3 m s^{-1} and wave amplitude not reaching more than 10 cm. Using these field values would yield a $3.5 \text{ Bq hr}^{-1} \text{ m}^{-2}$ maximum ^{222}Rn loss through atmospheric evasion [Turner *et al.*, 1996; Lambert and Burnett, 2003]. ^{222}Rn concentration began to increase during ebb tide peaking just after the lowest tide. Concentrations decreased at mid-flood tide with the lowest concentration occurring just before the highest tide level (Figure 2.3). This trend is similar to the patterns observed in areas with along-shore groundwater discharge. Higher ^{222}Rn concentration at lower tides is associated with stronger porewater fluxes and lesser dilution with offshore waters while the opposite occurs at higher tides. ^{222}Rn concentration from wells and springs collected within the watershed ranged from 833 to $3.08 \times 10^4 \text{ Bq m}^{-3}$, with an average of $4.6 \times 10^3 \text{ Bq m}^{-3}$. Groundwater samples collected in other studies in the Philippines have

similar ^{222}Rn concentration ranges [Taniguchi *et al.*, 2008; Cardenas *et al.*, 2010]. Porewater samples collected from seepage meters 1 and 3 yielded 2.9×10^3 and 3.1×10^3 Bq m^{-3} of ^{222}Rn , respectively.

Volumetric water fluxes were estimated using a three-hour running average of the hourly ^{222}Rn measurements. A conservative estimate of 30 cm d^{-1} of water flux was added to the calculated fluxes to compensate for dilution based on the highest negative ^{222}Rn flux [Burnett and Dulaiova, 2003] to account for ^{222}Rn dilution. Seepage estimates from the measured ^{222}Rn concentration ranged from $20 - 147 \text{ cm d}^{-1}$ with an average 73 cm d^{-1} using ^{222}Rn porewater values from the seepage meters. The overall temporal trend showed typical patterns with tides where high seepage rates occurred during ebb tide and were generally low during flood tide (Figure 2.3). The ^{222}Rn -based groundwater discharge shown in Figure 2.3 is based on the average seepage meter ^{222}Rn concentration of $3.0 \times 10^3 \text{ Bq m}^{-3}$. The flux magnitudes decrease by 50% using ^{222}Rn concentrations based on samples collected from springs and wells within the watershed.

A narrow salinity range of 32-33.5 ppt from a conductivity-temperature-depth logger deployed directly beneath the submersible pump was observed over the study period whereas offshore salinity is at 37 ppt. These values indicate that freshwater constitutes about 11 % of the total water volume at the site. Salinities are generally low during low tide and vice versa (Figure 2.3). This is caused by groundwater input through SGD as there are no immediate streams discharging into the site. The influence of rivers discharging along the shoreline southeast of the study site is also insignificant evident from channel salinities similar to offshore waters.

2.4.2. Direct seepage measurements and porewater salinity

Porewater flux from seepage meters ranged from 1 to 47 cm d⁻¹ with a mean of about 28 cm d⁻¹ (Figure 2.4). These values were well within the seepage range estimated from continuous ²²²Rn monitoring. However, the maximum seepage rate may have been underestimated as the bags were at full capacity during peak flux periods. Subtidal fluxes yielded a similar range of values compared to intertidal seepage rates (Figure 2.4). This trend is not consistent with the typical exponential decrease in seepage with distance from the shoreline reported in other studies [Bokuniewicz, 1980; Robinson *et al.*, 1998]. Freshwater input from discrete groundwater outlets are the likely source of additional seepage farther away from the shoreline. The average flux rates are 33 and 20 cm d⁻¹ for the intertidal and subtidal seepage meters, respectively.

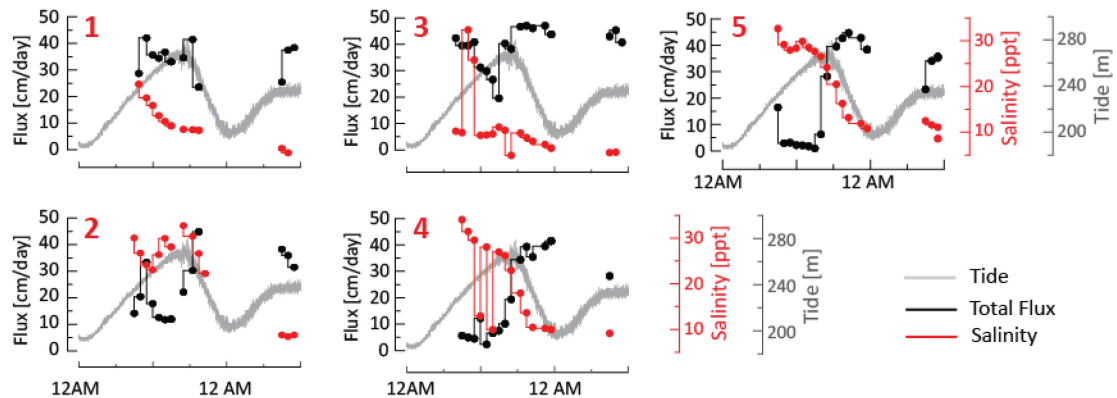


Figure 2.4. Submarine groundwater discharge measurements and salinities through time from manual seepage meters. Seepage meters 1 and 2 were placed in the intertidal zone and seepage meters 3, 4 and 5 were positioned in the subtidal region; seepage meter locations are shown in Figure 2.1.

Seepage rates increased around high tide in all seepage meters (Figure 2.4). The timing of the peak discharge occurred earlier compared to temporal patterns in other field and modeling studies. The typical temporal seepage trend begins to increase after high tide

[Robinson and Gallagher, 1999; Lambert and Burnett, 2003; Robinson et al., 2007a]. Higher discharge values at mid flood tide were also observed in all stations but were less conspicuous in the subtidal zone.

Porewater salinity from the seepage meters fall within an intermediate range of 5 to 33 ppt which is about 14 to 89 % seawater considering an open ocean salinity of 37 ppt measured during the sampling period. The brackish discharge suggests substantial mixing between freshwater and seawater occurring in the subsurface. Flux from seepage meter 1 located in the upper intertidal zone yielded a narrow range of 5-20 ppt whereas the rest fall within the overall salinity range. The lower salinity of manual seepage meter samples, particularly seepage meters 4 and 5 in the subtidal zone, is consistent with the presence of discrete freshwater outlets as salinities closer to seawater is expected moving farther away from the shoreline.

2.4.3. Numerical simulation results

In order to provide a mechanistic basis for the observations and to more broadly understand the mixing dynamics in permeable sediment overlying discrete zones of groundwater seepage, I simulated a beach section with 10 cm wide discrete groundwater outlets. The outlet size was based on the aperture of the freshwater spring just east of the beach transect (Figure 2.1). The outlets were placed at distances of -10 m, 30 m and 70 m at the base of the domain where freshwater can leak out through the overlying sediments (Figure 2.2). These locations represent freshwater outlets beneath the subtidal, intertidal and supratidal zones respectively and are used throughout the text to identify the outlet locations including the non-tidal simulations. Different boundary condition representing scenarios with constant outlet heads, with and without tides, and dynamic outlet head were simulated and assigned as Cases 1-4 (Figure 2.5-2.8). The base case represents a scenario

with a maximum sediment thickness of 5 m and an outlet head of 1 m above mean sea level.

I define mixing zones as regions in the subsurface with salinities between 10 to 90% seawater. In order to quantify the effect of various drivers on the mixing zones, an effective width was used as metric which is the mixing zone area normalized to the average sediment thickness. The effective mixing zone width normalizes for the effect of sediment thickness on the total area of the GW-SW mixing zones.

Simulation results from the subtidal region were used as representative for describing the effects of scenarios with constant and dynamic outlets as well as cases with varying sediment thickness. This location also represents a more isolated setting where the effect of flow from nearby outlets is limited. Hence, metrics reported in the succeeding sections are from the subtidal zone unless stated otherwise.

2.4.3.1. Case 1

This scenario simulates a condition where both the head at the discrete outlets and the surface water level are constant. The simulated base case produced freshwater plumes emanating from the intertidal and subtidal zone outlets (Figure 2.5). Freshwater from the supratidal outlet saturated the lower part of the onshore domain, flowed seaward and discharged along the shoreline, similar to a coastal unconfined aquifer (Figure 2.5B). The seaward freshwater flow joined the upwelling freshwater plume from the intertidal zone outlet forming a wider freshwater intertidal discharge zone (Figure 2.5A-C). Seawater recirculation cells formed along the outer boundaries of the intertidal and subtidal freshwater plumes. Mixing zones developed between the seawater recirculation cells and the freshwater plumes. The mixing zones are thinner closer to the base and widen towards

the SWI. The intertidal and subtidal mixing zones have a similar shape even with different sediment thicknesses at their respective locations.

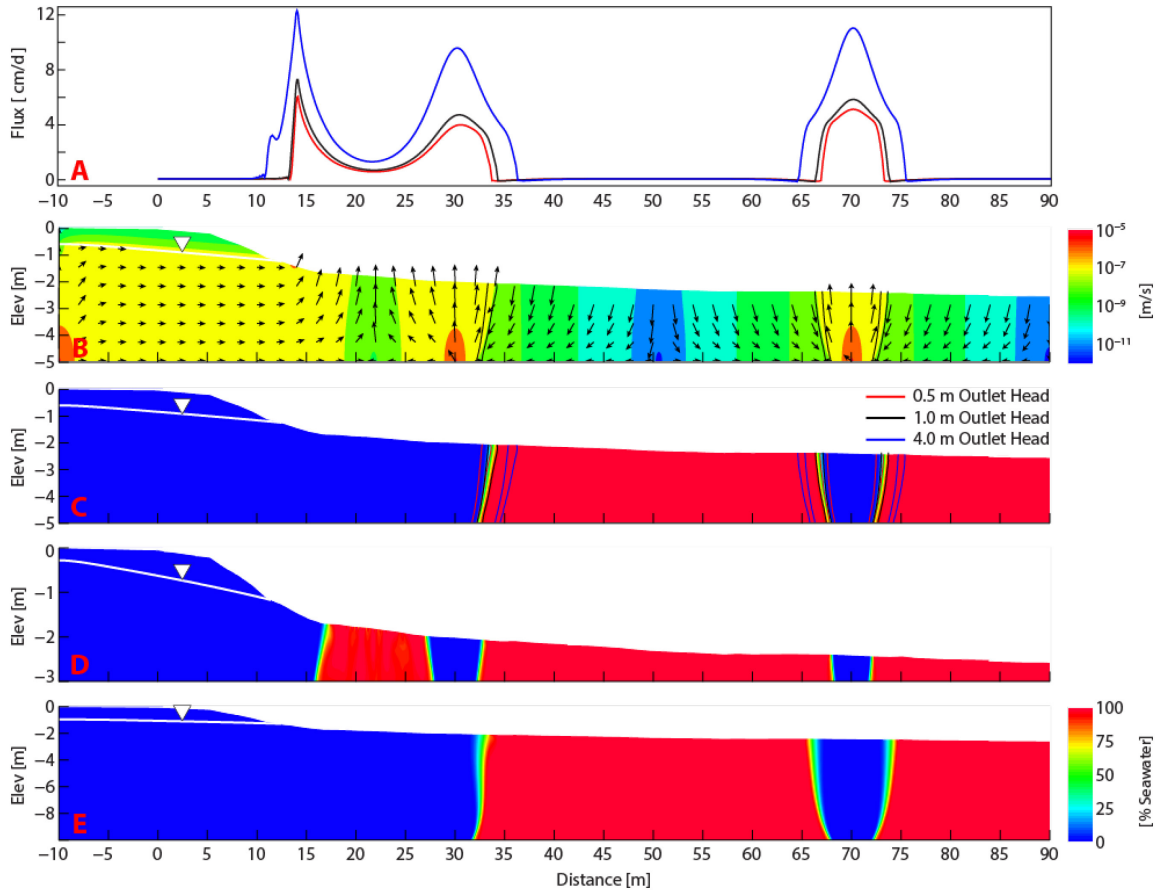


Figure 2.5. Seepage rates along the SWI, velocity vectors and magnitudes, and salinity distribution for Case 1 with no tidal oscillations and a constant outlet head. (A) Seepage rates along the SWI for the base case with 1 m outlet head, (B) velocity magnitude with arrows (not proportional to velocity) showing flow directions, (C) salinity distribution with contours showing the mixing zone boundary (10-90% seawater) at different constant recharge values, (D) salinity field for the domains with a maximum thickness of 3 m and (E) 10 m.

Models were simulated using different values of the outlet hydraulic head to determine the effect of groundwater seepage strength. Values of 0.5, 1 and 4 m above the mean sea level were used to represent seasonal changes in recharge conditions. The base model yielded mixing zones that varied slightly but with very similar cross sectional areas. The effective width of the subtidal mixing zone was constant at 0.6 m using different outlet head values. This suggests that the magnitude of a steady freshwater inflow does not substantially influence the size of the mixing zone. The freshwater plumes widened with an increase in the outlet head as indicated by the longer distance between the pair of mixing zones developed at the subtidal zone (Figure 2.5). The width of the plumes were 4.9, 5.9 and 9.3 m for corresponding outlet heads of 0.5, 1 and 4 m respectively.

The mixing zones varied linearly with sediment thickness. Effective widths at the subtidal zone are 0.4, 0.6 and 0.9 m for the domains with maximum sediment thicknesses of 3, 5 and 10 m respectively. The width of the freshwater plume along the SWI at the subtidal location also increased for all cases with values at 3.9, 5.9 and 6.5 m. An intertidal circulation cell also developed in the model with thinner sediments which separated the freshwater plumes from the supratidal and the intertidal outlets (Figure 2.5D).

2.4.3.2. Case 2

Case 2 represents scenarios with tidal variations and constant outlet heads. To assess the net effect of tidal fluctuations on GW-SW mixing dynamics, time averaged salinity and velocity magnitudes were calculated using the last 30 days of the transient models. At the subtidal zone, the salinity distribution and flow features observed in Case 1 were all retained in the model with tides (Figure 2.6A-C). However, a slight inward tapering at the top of the mixing zones was observed (Figure 2.6C). A saline plume was formed in the upper intertidal zone which is consistent with other models that

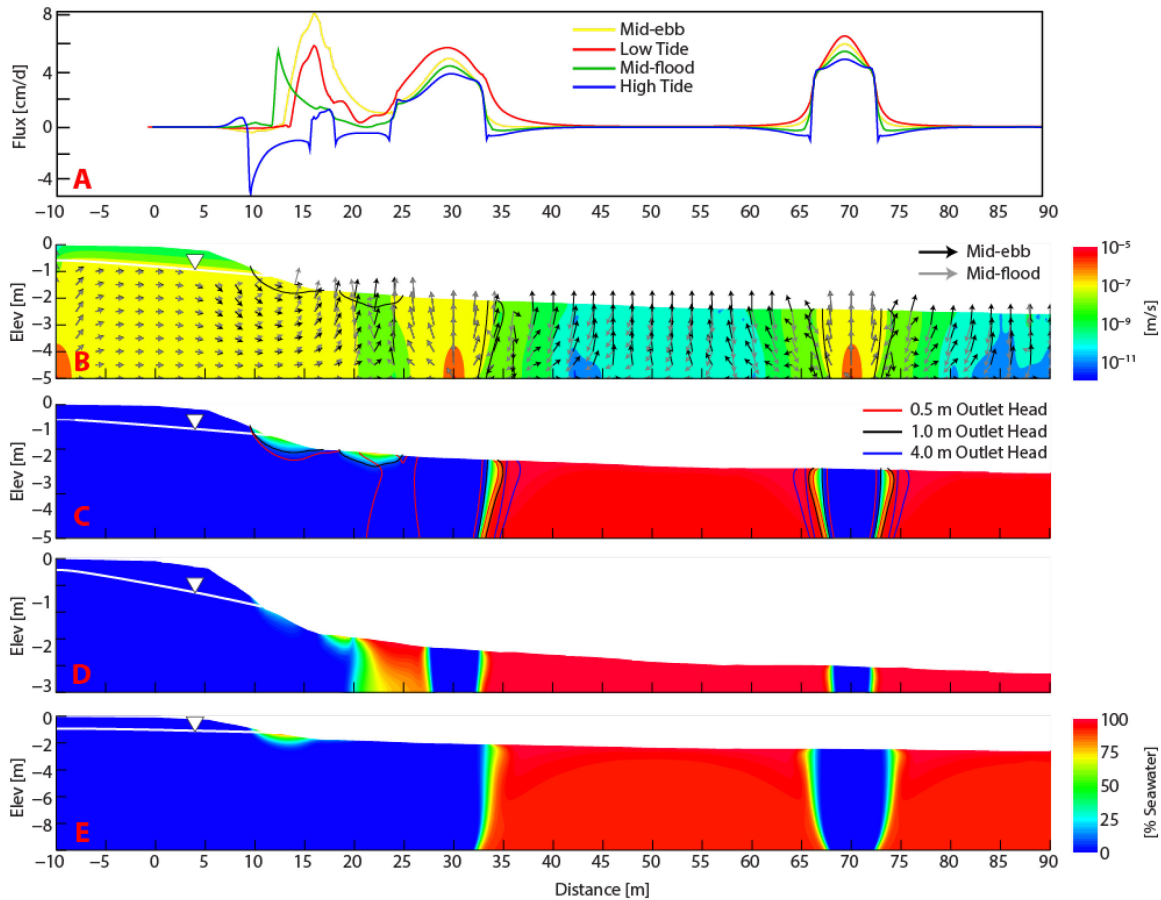


Figure 2.6. Seepage rate along the SWI, velocity vectors and magnitude, and salinity distribution for Case 2 with tidal oscillations and a constant outlet head. (A) Seepage rate distribution along the SWI for the base case with 1 m outlet head at different tide level, (B) phase averaged velocity magnitude with arrows (not proportional to velocity) showing flow directions for ebbing and flooding tide, (C) phase averaged salinity distribution with contours showing the mixing zone boundary (10-90% seawater) at different constant outlet head values, (D) phase averaged salinity field for the domains with a maximum thickness of 3 m and (E) 10 m.

incorporated tides in their simulation [Robinson *et al.*, 2007c; Abarca *et al.*, 2013]. Furthermore, the mixing zones along the edge of the freshwater plumes became twice as broad. There was no change in the general position of the freshwater plumes with tides. Consequently the freshwater boundary of the mixing zones (10% seawater) remained in

the same position as those in Case 1. However, the outer limit (90% seawater) moved farther away from the axis of the freshwater plume (Figure 2.6C). There was no change in the overall effective width of the mixing zones within a tidal cycle although some salinity variation in the upper few centimeters was observed (Figure 2.9A).

The upwelling freshwater plumes in Case 2 for simulations with different outlet heads are similar to their Case 1 counterpart. However, the intertidal saline plume did not develop in the scenario with a higher outlet head (4 m). The mixing zones at the edge of the freshwater plumes did not vary significantly with changes in the outlet heads but are consistently wider than those in Case 1 (Figure 2.6). Effective mixing zone widths at the subtidal zone with increasing outlet head are 1.1, 1.0 and 0.8 m respectively. The intertidal saline plume was also present in the simulation with a lower outlet head.

The width of the freshwater plume along the SWI increased with sediment thickness (3.8, 5.9, 6.7 m) similar to Case 1. Effective mixing zone widths at the subtidal region also increased with thicker sediments with values at 0.7, 1.0 and 1.3 m for the cases with maximum sediment thicknesses of 3, 5 and 10 m. The intertidal circulation cell also developed in the model with thinner sediments similar to Case 1 (Figure 2.6D).

2.4.3.3. Case 3

I simulated changes in the strength of the outlet seepage linked to seasonal changes in the water table elevation using a dynamic outlet head. The sinusoidal outlet head function was set to fluctuate between 0.5 to 4 m above the surface water level which are the minimum and maximum values used in Cases 1 and 2. Simulation results developed freshwater plumes and circulation cells similar to Case 1 and 2 (Figure 2.7B-C). The freshwater plumes in this scenario were much narrower at the base and tapered more at the top compared to the previous cases.

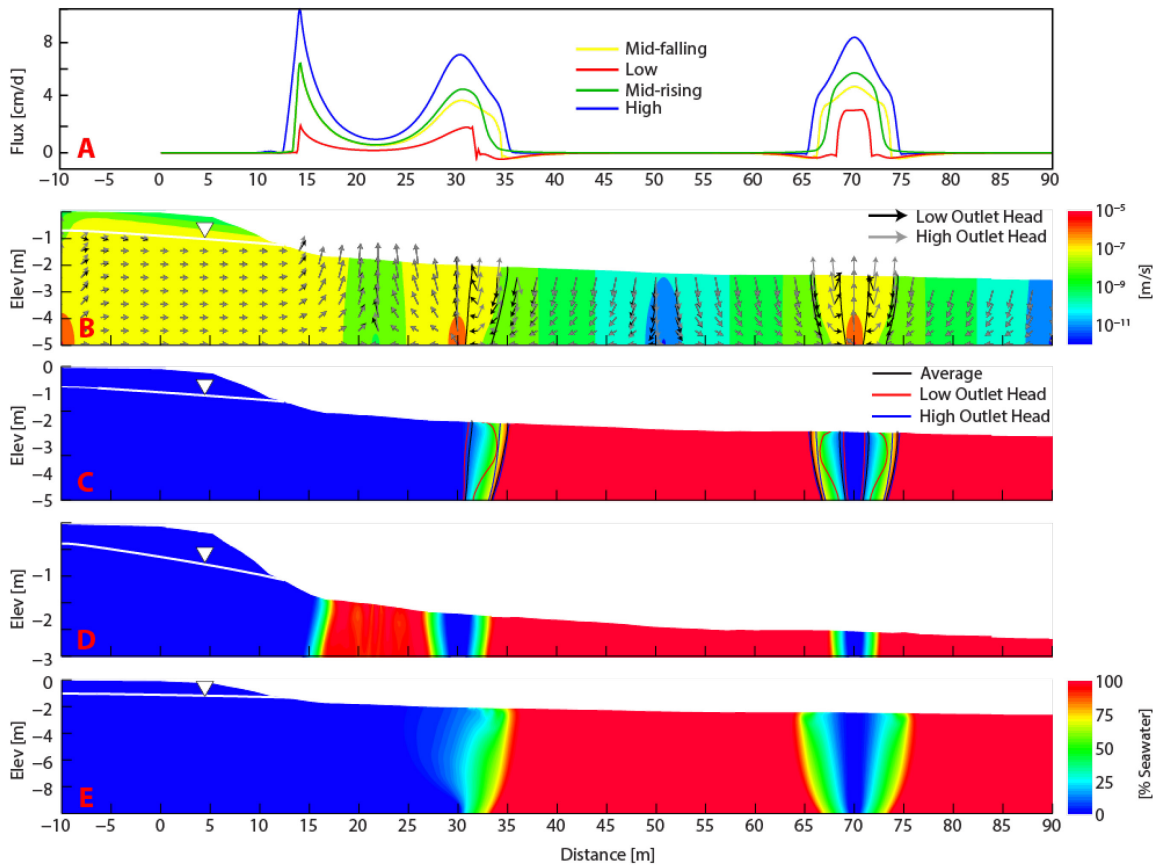


Figure 2.7. Seepage rate along the SWI, velocity vectors and magnitude, and salinity distribution for Case 3 without tidal oscillations and a dynamic outlet head. (A) Seepage rate distribution along the SWI at different outlet head level (B) average velocity magnitude with arrows (not proportional to velocity) showing flow directions for low and high outlet head values, (C) average salinity distribution with contours showing the mixing zone boundary (10-90% seawater) at low and high outlet head values, (D) average salinity field for the domains with a maximum thickness of 3 m and (E) 10 m.

The simulated mixing zones were generally wider and more variable than in Case 1 and 2. They were widest during lower outlet head levels and narrowest during peaks in the freshwater outlet head (Figure 2.7C). Smaller seawater circulation cells also developed at the top of the mixing zones when the outlet head is low (not shown in the figures). The effective widths range from 0.6 to 1.8 m for the mixing zones generated at the subtidal zone. The opposite trend was observed for the freshwater plume widths along the SWI

where values range from 1.6 to 7.8 m (Figure 2.9B). This range was slightly narrower relative to the simulated scenarios in Case 1 (0.9-8.1 m) with constant outlet heads. The timing of the widest freshwater plume lagged the outlet head peak by 30 days (Figure 2.9B).

Thicker sediments produced wider mixing zones and freshwater discharge plumes. The ranges in the mixing zone effective width at the subtidal region are 0.3-0.7 m and 1.0-2.7 m for the simulations with sediment thicknesses of 3 and 10 m respectively. The timing of widest mixing zone in thinner sediments leads the low outlet head while it is lagged in thicker sediments (not shown in figures). Freshwater discharge plumes for both scenarios have similar temporal trends with the base case. The values ranged from 1.5 to 4.7 m and 1.1 to 9.9 m for domains with thinner and thicker sediment cover respectively. The simulation with thinner sediments consistently produced the intertidal circulation cell found in Case 1 and 2 with similar sediment thickness (Figure 2.7D).

2.4.3.4. Case 4

Case 4 combined tidal oscillations with seasonal changes in the outlet seepage strength. Simulation results yielded freshwater plumes and seawater circulation cells that showed a similar configuration with Case 3. An intertidal saline plume similar to Case 2 and a circulation cell between the freshwater plumes from the supratidal and intertidal outlet were also formed (Figure 2.8). This scenario produced the widest mixing zones relative to all other cases.

In the subtidal zone, effective mixing zone widths varied from 0.7 to 2.3 m. Broader mixing zones were observed during low outlet head conditions and vice versa which was similar to Case 3 (Figure 2.8C). Variations in the mixing zone with tides was limited to the top few centimeters which was also observed in Case 2 evident from the variability of the

mixing zone width along the SWI (Figure 2.9C). Freshwater plume widths along the SWI ranged from 1.3 to 7.9 m at the subtidal region which were close to the range observed in Case 3. The intertidal circulation cell was also present even during periods with higher outlet heads.

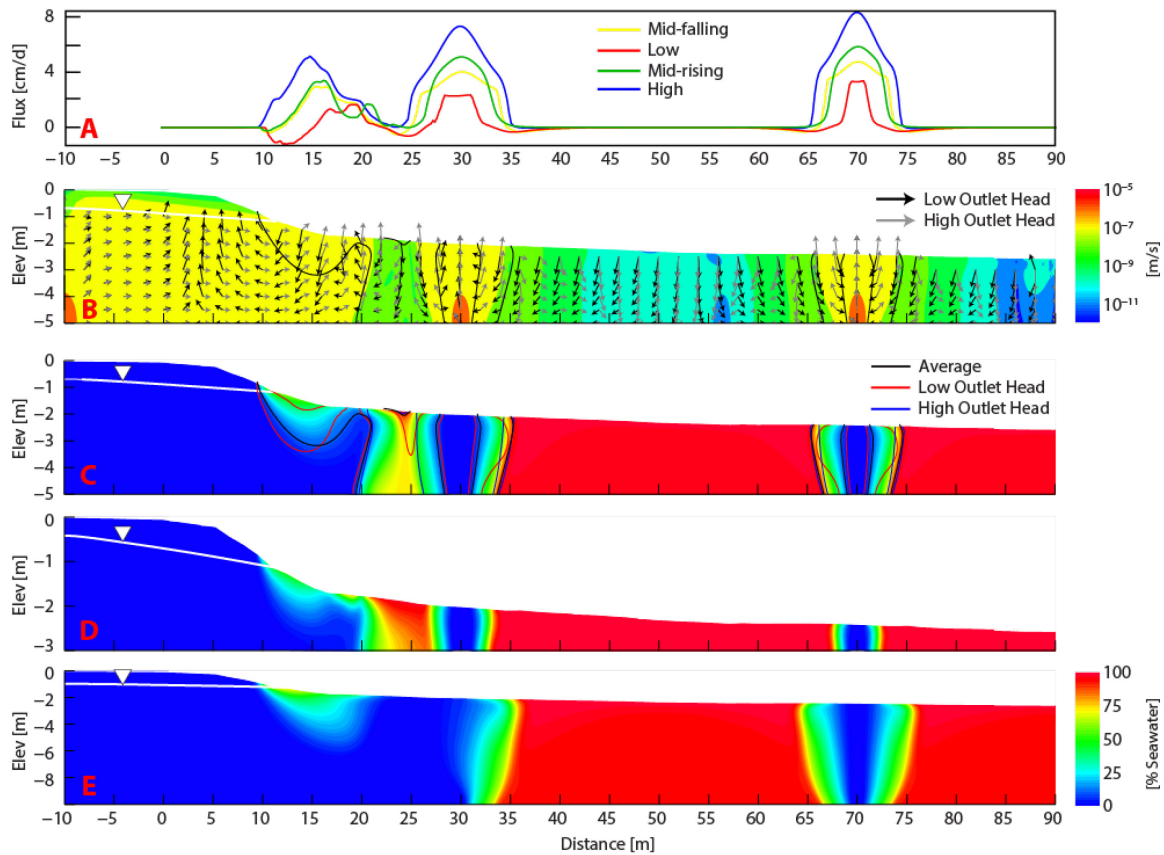


Figure 2.8. Seepage rate along the SWI, velocity vectors and magnitude, and salinity distribution for Case 4 with tidal oscillations and a dynamic outlet head. (A) Phase averaged (tidal) seepage rate distribution along the SWI at different outlet head level (B) average velocity magnitude with phase averaged vectors (not proportional to velocity) showing flow directions for low and high outlet head values, (C) average salinity distribution with contours showing the phase averaged mixing zone boundary (10-90% seawater) at low and high outlet head values, (D) average salinity field for the domains with a maximum thickness of 3 m and (E) 10 m.

Mixing zone and freshwater plume variability with sediment thickness were more similar to Case 3 than Case 2. The effective width at the subtidal region ranged from 0.6 to 1.5 m and 1.1 to 3.2 m for the models with maximum sediment thicknesses of 3 and 10 m respectively. The discharge plumes were consistently wider in thick sediments and vice versa. The intertidal circulation cell is consistently present in the thin sediments as with previous cases but did not develop in thicker sediments (Figure 2.8D- E).

2.4.3.5. Porewater fluxes

Freshwater fluxes were highest at the center of the plumes and gradually decreased towards the mixing zones in Case 1. The fluxes across the SWI were negative above the seawater re-circulation cells (Figure 2.5A). The seaward freshwater discharge from the supratidal outlet peaks right at the shoreline and sharply decayed seaward, as with typical unconfined aquifers discharging along shorelines [Robinson *et al.*, 1998, 2007b]. The average freshwater seepage rate along the SWI in the subtidal region for Case 1 were 4.5, 4.9 and 7.1 cm d⁻¹ for the scenarios with 0.5, 1 and 4 m outlet head, respectively. Fluxes with salinities between 10 and 90 % seawater did not vary much even in cases with higher outlet heads. The average brackish flux on top of the 1.3-1.4 m (total for the 2 pairs) mixing zone was between 2.0 to 2.2 cm d⁻¹ for all Case 1 scenarios. The average freshwater seepage rate for the case with thinner sediments was higher at 7.9 cm d⁻¹ than the thicker sediments at 3.9 cm d⁻¹. Both scenarios yielded similar average brackish water flux of 2.1 cm d⁻¹.

Similar spatial patterns were observed for porewater fluxes in Case 2 relative to Case 1 with only the fluxes along the upper intertidal zone changing with tides (Figure 2.6A). Seawater fluxes along the SWI above the circulation cells switched from infiltration to exfiltration from flooding to ebbing tide. The seepage rates however were 2 orders of magnitude lower than freshwater or brackish fluxes. Average freshwater seepage with tides

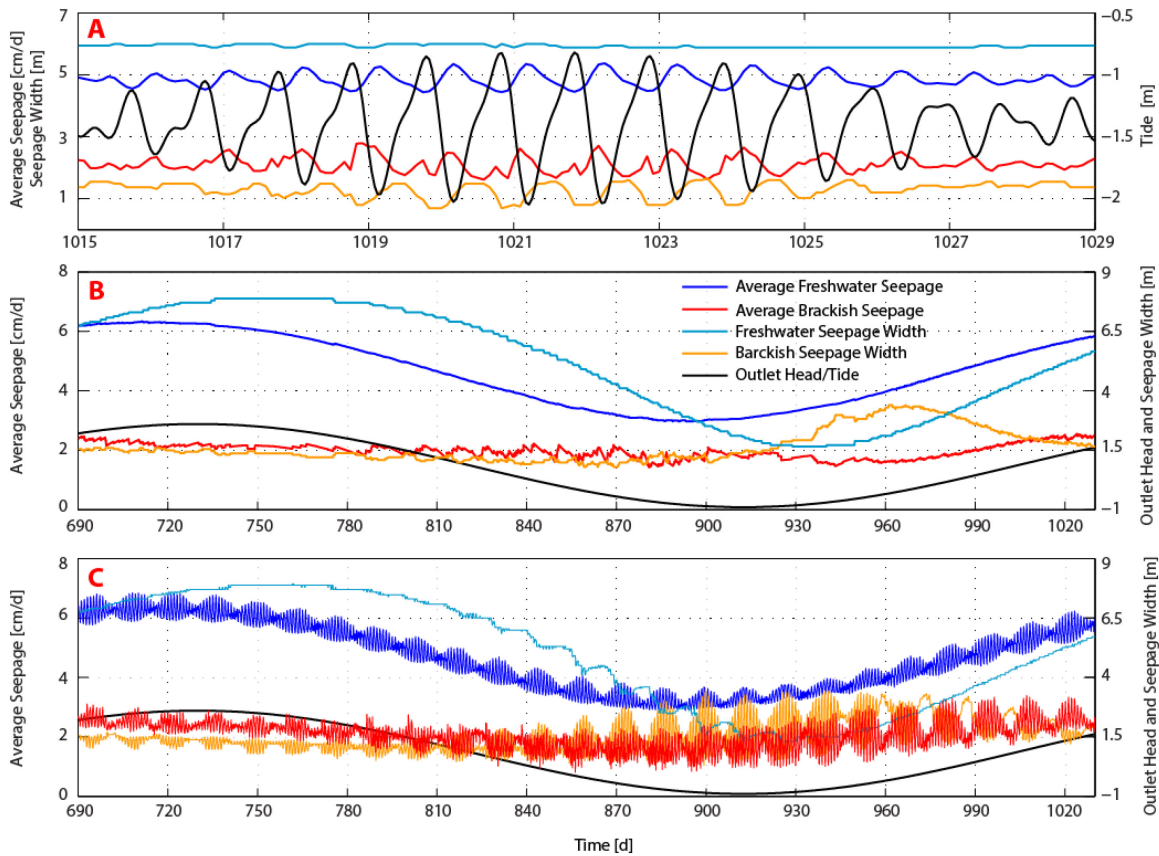


Figure 2.9. Temporal flux trends for the simulated transient models. (A) Case 2, (B) Case 3 and (C) Case 4.

had ranges of 4.0-5.0, 4.4-5.4 and 6.7-7.7 cm d^{-1} for models with outlet heads of 0.5, 1 and 4 m, respectively. The average brackish fluxes at the SWI yielded values between 1.6-2.9 cm d^{-1} for all cases with different outlet heads. The brackish discharge zone width along the SWI in the subtidal zone for all cases have the same range at 0.6 to 1.8 m. Freshwater fluxes showed an inverse trend with tidal heights (Figure 2.9A). Higher brackish peaked at high tide during periods with a higher tidal range. The peak progressively shifted towards low tide with decreasing tidal range. The field measurements showed similar trends to those of the average tidal range in the simulation (1019 d; Figure 2.9A). Freshwater fluxes were higher in simulations with thinner sediments ranging from 6.7 to 9.8 cm d^{-1} whereas

thicker deposits yielded a range of 3.5 to 4.3 cm d⁻¹. However, scenarios with thicker sediments had generally higher brackish fluxes with rates ranging from 1.8 to 2.9 cm d⁻¹ whereas the model with thinner sediment cover yielded rates of 1.2 to 2.7 cm d⁻¹.

Scenarios with a dynamic water table yielded spatial flux distributions similar to Case1 with values increasing and decreasing with the outlet head (Figure 2.7A). Freshwater seepage rates vary between 3.0 to 6.3 cm d⁻¹ and were higher with higher outlet heads and vice versa. The brackish flux led the freshwater seepage trend where it peaked at the middle of a rising outlet head. The seepage range is much narrower relative to the freshwater flux at 1.5 to 2.5 cm d⁻¹ for the base case. The total length of the subtidal brackish discharge zone fluctuate between 0.8 and 3.4 m and was wider during the rising outlet head phase (Figure 2.9B). The numerical models with thicker and thinner sediment cover had similar brackish seepage ranges at 1.3-2.3 cm d⁻¹ and 1.3-2.6 cm d⁻¹ respectively. Freshwater seepage decreased with sediment thickness. Fluxes in thinner sediments fluctuated between 3.9 to 10.9 cm d⁻¹ whereas flux ranged from 2.6 to 4.9 cm d⁻¹ with thicker sediments.

High flux values in Case 4 were also centered at the freshwater plumes in the subtidal zone and the average position of the seepage face in the upper intertidal zone (Figure 2.8A). Freshwater fluxes were similar with those in Case 3 ranging from 2.8 to 6.8 cm d⁻¹. Brackish seepage rates varied from 0.7 to 3.3 cm d⁻¹ which was also close to the values in Case 3. The width of the brackish discharge zone at the SWI varied between 0.3 and 3.5 m. Freshwater fluxes are generally stronger at higher outlet head values with the peak seepage rate coinciding with lower tides at the highest freshwater outlet head. Changes in the freshwater flux values were smaller with tidal changes compared to fluxes associated with seasonal fluctuations. Brackish fluxes also generally followed trends in the dynamic outlet head. Tidal effects were more conspicuous in periods of lower outlet head (Figure 2.9C). Brackish fluxes for scenarios with thicker and thinner sediment also yielded

similar ranges at 0.7-3.1 cm d⁻¹ and 0.7- 4 cm d⁻¹ respectively. However, freshwater seepage rates were consistently lower in thicker sediments with ranges of 2.8-12.4 cm d⁻¹ and 2.5-5.2 cm d⁻¹ for the models with thin and thicker sediments respectively.

2.5. DISCUSSION

2.5.1. Subsurface flow and mixing features

The general subsurface flow and mixing features described here were based on Case 1 simulations with no tidal variation and a constant freshwater outlet head. Freshwater upwelling plumes and seawater circulation cells were formed in permeable sediments underlain by discrete outlets of freshwater (Figure 2.5). The presence of the upwelling plumes in the simulations is consistent with reports of relatively fresh porewater in sediments surrounding known submarine springs (from a lava tube source) in Mauritius [Povinec *et al.*, 2012]. The plumes form as freshwater disperses away from the outlet sources but are then focused towards the SWI by the establishment of density-driven circulation cells along the periphery of the upwelling plumes. The symmetrical U plume shape particularly at the subtidal region is associated with the encroaching toe of recirculation cells on both sides of the plume. The density difference between seawater and freshwater allows the toe to advance which forms a stable configuration where the denser saltwater is below the upward flowing freshwater. This is also the mechanism that develops the saltwater wedge-freshwater lens system in coastal unconfined aquifers [Cooper, 1959; Abarca *et al.*, 2007]. The wider freshwater discharge zone closer to the shoreline (Figure 2.5) is the product of the combined effect of the seaward freshwater flow from the supratidal outlet and the intertidal zone plume. The wide freshwater discharge zone separates into a freshwater plume and smaller alongshore freshwater discharge tube in simulations with thinner sediments (Figure 2.5D) or with a lower landward water table

(Figure 2.6B). This suggests that freshwater discharge zones can be from single or multiple outlets depending on the strength of the freshwater discharge and the thickness of the sediments. This speaks of the complexities that may arise when different outlet spacing and aperture widths are used. In the case of Mauritius [Povinec *et al.*, 2012], length of the low bulk conductivity zone is around 20-80 m and highly heterogeneous around the main spring which suggest that there is likely more than one freshwater outlet with variable aperture size and distribution considering a thinner sediment cover in the order of 1 m.

Mixing zones (10-90% seawater) formed along the edges of the freshwater plumes and recirculation cells. These zones traced the boundaries of the plumes and recirculation cells following an inclined configuration which widens upward towards the SWI. Because flows between the freshwater plumes and the edge of recirculation cells are predominantly vertical (Figure 2.5B) lateral movement of salts would be mostly due to dispersion. Hence the widths of the mixing zones with a steady outlet head and no tidal effects would entirely depend on the magnitude of the porewater velocity along plume and recirculation cell boundary.

2.5.2. Effect of tides

The effect of tidal variability was examined from Case 2 where fluctuations in the head potential along the SWI with tides was implemented. The simulations also accounted for changes in the subsurface total stress with the changing water load due to tides on top of the domain. The freshwater plumes and seawater recirculation cells developed in this scenario were very similar to the case without tides. The most conspicuous effect of tides was the addition of the intertidal saline plume in the upper intertidal zone and wider mixing zones that tapered along the SWI. Seawater infiltration in the unsaturated upper intertidal zone during high tide allows the formation of the intertidal saline plume. The development

of the intertidal saline plume is a common feature for systems with tidal influence and have been reported in other simulations and field studies [Robinson *et al.*, 2007a; Abarca *et al.*, 2013]. The wider mixing zones with tides are due to the oscillating flow field induced by tidal fluctuations (Figure 2.6B). When the tide is rising, instantaneous velocities in the mixing zones are directed down and towards the freshwater plumes whereas velocity vectors point up and away from the plumes when the tide is ebbing. Furthermore, higher flow velocities on each side of the freshwater plume closer to the SWI were observed in Case 2 relative to the scenario without tides (Figure 2.5B and 2.6B). This increases the dispersion of salts which increases the width of the mixing zones. The mixing zones did not significantly change within a tidal cycle in the simulation except close to the SWI where the outer boundary (90% seawater) expanded and contracted with tides (Figure 2.9A). This is also consistent with the behavior of freshwater plumes reported in Mauritius [Povinec *et al.*, 2012] which did not change with tides. The tapered top of the mixing zone in the simulation with tides is due to seawater infiltrating when the environmental head at the SWI is higher than the head just beneath the SWI. Exfiltration occurs at ebb tide when the opposite trend occurs. This also suggests that the top of the mixing zone towards the edge of the seawater recirculation cell is very active at tidal time scales.

2.5.3. Effect of outlet head variability

Similarities in the general configuration and width of the mixing zone albeit using different outlet heads suggest that steady or constant rate of freshwater seepage from the outlets do not significantly influence the size of the mixing zone. This is despite of the width and position of the freshwater plume and seawater recirculation cells changing with the magnitudes of the outlet head (Figure 2.5C). This suggests that the flow conditions that disperses salt along the edge of the plumes are similar in all cases with steady outlet heads.

The dynamic outlet head in Case 3 yielded temporally changing configurations of the freshwater plumes and mixing zones. The mixing zones were wider during low outlet head and narrower at the peak outlet head. With a rising outlet head, flow vectors in the mixing zones are directed up and away from the freshwater plumes (Figure 2.7B). As the plumes widen with increasing freshwater input, the mixing zones are pushed farther and flushed on the freshwater side. The mixing zones narrow as the freshwater plumes widen. The mixing zones approximate the configuration of scenarios with a constant outlet head at the peak of the dynamic outlet head. When the outlet head is at a falling phase flow vectors in the mixing zone point towards the freshwater plumes and the density driven circulation pushes the mixing zones towards the freshwater plumes. As salt is dispersed towards the contracting freshwater plumes, the mixing zones expand occupying the outer edges of the freshwater plumes. Smaller scale density-driven circulation also formed near the SWI above the mixing zones and freshwater plumes while the water table is at its lowest (not shown in figures). This is caused by density instabilities overcoming the weak upward flow along the SWI.

2.5.4. Influence of sediment thickness

Simulation results using constant outlet heads (Case 1 and 2) with different sediment thicknesses indicate that freshwater plumes and mixing zones are slightly wider in thicker sediments. The slightly wider plumes form as more space in the subsurface is available to accommodate freshwater input as it diffuses upward. Mixing zones are also wider in thicker sediments that allow for longer flow paths leading to more dispersion of salt by the recirculating seawater. This is evident from the upward increase in width of the mixing zone in Case1 with no tidal and outlet head variation (Figure 2.5).

2.5.5 Relationship of subsurface flow features and porewater fluxes

Although no observed springs were present farther than 30 m from the high tide line during the field campaign, the lower porewater salinities measured from the seepage meters particularly in the subtidal zone require additional freshwater sources. This supports the idea that freshwater is leaking out of the underlying limestone even beyond the subtidal region albeit the absence of visible springs.

The values of the brackish point SGD measurements were an order of magnitude higher than the simulated instantaneous fluxes. However, the temporal trends in the seepage rates were observed in the simulation results. This suggests that the freshwater outlets at the study site has a more complex distribution. Seepage rates of higher magnitude are easily attained with the domain setup using an outlet head set at 15 m or higher. This value although high is not unrealistic as privately owned wells are only dug 10-15 m to reach freshwater at elevations of about 30-40 m. The high magnitude of seepage meter fluxes also suggest there could be a relatively high number of outlets distributed beneath the sediments in the study site.

Simulated freshwater fluxes yielded a tidal response similar to alongshore submarine groundwater discharge where fluxes are higher at low tide and vice versa [Robinson *et al.*, 1998, 2007a; Burnett and Dulaiova, 2003]. This universal response to tides is caused by the decrease and increase in the hydraulic gradient set up by the rise and fall of the water level along the SWI. Simulated brackish fluxes as well as field seepage measurements on the other hand have broader peaks and begin to increase right before high tide and decrease around low tide. This is caused by the focusing of the brackish discharge zone manifested by narrower brackish zone widths at the SWI at high to ebbing tide. Infiltration pushes the top outer side of mixing zone towards the freshwater plume at high tide which forces more brackish discharge in the narrower brackish discharge zone. During

ebb tide the infiltrated seawater is flushed back out together with brackish water while the squeezing effect of seawater infiltration on the brackish discharge zone is relaxed.

Simulated fluxes indicate that increasing the outlet head increases the freshwater seepage with no significant change in the brackish fluxes (Case 1 and 2). This is due to a quasi-steady state flow field in the vicinity of the freshwater plume once the freshwater plumes and circulation cells are established. Average freshwater fluxes followed the trend in the dynamic water table but with the widest freshwater plume occurring after the peak outlet head. The lag in timing of the highest average flux and widest plume width is likely due to the time required to flush the freshwater edge of the mixing zone and push away the recirculation cell. The average brackish discharge as well as its width along the SWI peaked on the rising phase of the outlet head (Figure 2.9B). This is due to the flushing of the wider subsurface mixing zone developed during periods when the outlet head was low.

2.6. SUMMARY AND CONCLUSIONS

I investigated groundwater-seawater mixing dynamics in permeable coastal sediment overlying areas of high terrestrially-sourced groundwater discharge, like those in overlying fractured or karstified carbonate platforms such as fringing reefs in tropical and tectonically active areas. Field observations, using methods based on local and point measurements, i.e., seepage meters, and integrated environmental tracer approaches, i.e., ^{222}Rn , were complemented by numerical flow and transport simulations both partly tuned to the field site.

This study shows that sediments covering areas of focused groundwater discharge create freshwater plumes, seawater recirculation cells, and freshwater-seawater mixing zones in the subsurface. The freshwater plumes form as freshwater disperses away from the outlet source and is focused towards the SWI by the establishment of density-driven

seawater recirculation cells. Mixing zones form along the edge of the freshwater plumes and recirculation cells. The numerical simulations also indicate that tides and water table dynamics and to a lesser extent the thickness of sediments influence the size of the freshwater plumes and the mixing zones.

Although efforts have been made to tune the simulations to field parameters, it was not the intention of this work to exactly match the conditions observed in the field as there is no information on the geometry of freshwater outlets and their position relative to the seepage meters. However, over-all trends in simulated fluxes along the SWI are in good agreement despite the actual magnitude of field measurements being underestimated in the simulations. This speaks to the complexity arising from local or point measurements such as seepage meters and spot salinity measurements and at the same time the lack of details provided by the integrated tracer measurements, such as Rn-based mass balance calculations. Temporal trends in both freshwater and brackish fluxes also suggest that perturbations from both land and sea forcing have immediate effect on freshwater-seawater the mixing dynamics and associated fluxes in this type of system.

2.7 ACKNOWLEDGEMENTS

The Coral Reef Targeted Research project under the Global Ecology Fund provided financial support for the conduct of this research. Additional supported was received from a National Science Foundation CAREER grant (EAR-0955750) to MBC, a Geological Society of America student grant to PBZ, and the Geology Foundation at the University of Texas at Austin. I thank Dr. Edgardo Gomez for providing the Rn monitor and for logistical assistance in this study and Dr. Isaac Santos for analyzing the samples for Radium.

Chapter 3: Controls on the dynamics of the subterranean estuary and hyporheic zone of a river estuary determined from hydraulic, thermal and geophysical monitoring

3.1. ABSTRACT

The subterranean estuary is broadly defined as the subsurface zone of mixing of saline and fresh groundwater in coastal areas. The seldom studied flow and transport processes in subterranean estuaries mediate biogeochemical and thermal processes. Groundwater flow and salinity dynamics were investigated at nested spatial and multi-temporal scales of the subterranean estuary underlying a small river estuary. Electrical resistivity (ER) surveying was conducted at the river-estuary transition zone through a tidal cycle and also across the entire estuary to map porewater salinity variation. Groundwater hydraulic measurements and vertical temperature profiling were also conducted within the sediment. Time-lapse ER across the channel at the river-estuary transition zone revealed a static resistive zone on the side of the channel with a pronounced cut bank. At the shallow portion of the opposite bank, zones that became less resistive with increasing estuary water level were observed. Groundwater head gradients indicating strong upward flux and pronounced vertical temperature gradients with colder temperatures deeper within the sediment indicate a stable zone of fresh groundwater discharge along the cut bank. Subsurface temperatures closer to that of surface water, head distributions indicating both groundwater efflux and influx, and higher porewater salinity indicate that shallow water areas close to the depositional bank were dominated by hyporheic circulation. The high ER near the cut bank was persistent in the estuary-wide ER profiles, which showed similar patterns in thalwegs/cut banks of sinuous portions of the estuary and low ER values in

shallower areas mainly in straighter estuarine reaches. A decrease in estuary-wide ER in highly resistive zones when the regional water table is lower, indicate infiltration of surface water into the sediment. This study highlights the importance of channel morphology and surface water-groundwater interaction on porewater salinity dynamics of the subterranean estuary underneath a river estuary. Understanding porewater salinity dynamics at different scales in subterranean estuaries can improve our understanding of material transformations and their contributions to measured chemical fluxes from coastal streams.

3.2. INTRODUCTION

River and oceanic hydraulic forcing converge in river estuaries creating a hybrid system, which has both dynamic flow and salinity. Underneath the estuary is a subsurface mixing zone where estuarine surface water circulates and interacts with groundwater. The subterranean estuary or STE is formally defined as a coastal aquifer where terrestrial groundwater measurably dilutes sea water that has infiltrated the aquifer through a free connection to the sea [Moore, 1999]. I extend this definition to the blanket of surface sediments as well as the porous materials on the banks and underneath river estuaries where surface water can recirculate or further mix with fresher groundwater. Groundwater and surface water mixing in STEs give rise to geochemical gradients that promote the development of benthic niches. Organisms in these zones perform biogeochemical functions, which have both ecological and economic importance. Salinity is a master variable influencing the community composition of benthic organisms and hence biogeochemical functions in the subterranean estuary [Underwood *et al.*, 1998; Coull, 1999; Dudley Williams, 2003; Coci *et al.*, 2005; Sahan and Muyzer, 2008; Santoro, 2010].

Despite its importance, we are just beginning to understand the drivers of porewater salinity variations in aquifers under estuaries.

The extent of groundwater-surface water interaction and circulation in aquifers adjacent to estuaries, which also includes hyporheic exchange or the shallow circulation of surface water intermittently through the sediments, is driven by surface water hydrodynamics, terrestrial groundwater gradients, and the density contrast between surface water and groundwater [Smith and Turner, 2001; Westbrook et al., 2005; Lenkopane et al., 2009]. Complex surface water hydrodynamics and salinity stratification in estuaries can overprint the effect of these drivers [Smith and Turner, 2001; Westbrook et al., 2005; Werner and Lockington, 2006; Lenkopane et al., 2009; Santos et al., 2012a]. Estuarine stage fluctuation with tides allows surface water to infiltrate along the intertidal zone forming a recirculation zone similar to an intertidal saline plume along coastlines [Robinson et al., 1998, 2007b, 2007c; Ataie-Ashtiani et al., 1999; Robinson and Gallagher, 1999; Li et al., 2008; Boufadel et al., 2011; Abarca et al., 2013]. Currents flowing over centimeter to meter scale channel bedforms and debris develops pressure variations along the sediment surface which induces hyporheic flow [Cardenas and Wilson, 2007b; Sawyer et al., 2011; Boano et al., 2014]. Furthermore, flow acceleration along river bends sets up a tilted free water surface which induces a subsurface cross channel flow [Boano et al., 2010, 2014]. Variations in magnitude and direction of currents in estuaries [Nidzieko et al., 2009] can induce a dynamic pressure distribution on the sediment surface which can influence the depth and residence times in hyporheic zones. This is further complicated by stratification or separation of water masses with different densities. Buoyancy driven fluid exchange due to density contrasts in groundwater and surface water can be magnified by surface water temperature variability and a wider range of salinity fluctuation that varies with tides and seasons in estuaries [Smith and Turner, 2001; Werner and Lockington, 2006;

Lenkopane et al., 2009; *Santos et al.*, 2012a, 2012b]. Persistent saline conditions allows more time for denser estuarine water to infiltrate into the underlying aquifer creating a convection cell similar to the groundwater salt wedge along coastlines [*Smith and Turner*, 2001; *Werner and Lockington*, 2006; *Lenkopane et al.*, 2009]. Periodically saline conditions can also develop smaller scale “salt fingers” when saltier water encroaches into the estuary but diffuses away when fresher river water pushes the saltwater seaward [*Webster et al.*, 1996; *Santos et al.*, 2012b].

Although hydrologic forces drive groundwater-surface water interaction at different scales and hence porewater salinity in subterranean estuaries, channel geomorphic features can influence the spatial variability and scale to which the interaction occurs [*Boano et al.*, 2014]. Geomorphologic features found in fluvial systems can exist in river estuaries as both may be a part of a larger fluvio-deltaic system. Bedforms and channel debris induce hyporheic flows in the order of centimeters to tens of meters scale depending on the water depth, geometry and spacing of the flow obstructing features [*Boano et al.*, 2014]. Point bars, meanders and island bars can induce groundwater-surface water interaction on a larger spatial and temporal scale. Furthermore, channel sinuosity as well as valley slope can focus and distribute groundwater flow, which affects the distribution and extent of groundwater-surface water interaction [*Cardenas*, 2009a, 2009b]. The spatial distribution of these geomorphologic features can be as complex as the estuarine hydrodynamics to which they are intimately related. However, the relative ease to which these geomorphic features can be mapped using standard surveys allows us to assess their influence on the extent of groundwater-surface water interaction.

The bulk electrical resistivity of sediments has been used extensively in coastal and fluvial settings to reveal porewater salinity structures in the subsurface and how they are linked to geologic, geomorphologic, and hydrologic controls [*Manheim et al.*, 2004; *Breier*

et al., 2005; *Swarzenski et al.*, 2006; *Swarzenski and Izbicki*, 2009; *Ward et al.*, 2010; *Cardenas et al.*, 2010; *Henderson et al.*, 2010; *Cardenas and Markowski*, 2011; *Befus et al.*, 2013, 2014; *Russoniello et al.*, 2013]. ER methods take advantage of the relatively high ER contrast between saltwater and freshwater making it an ideal geophysical tool in coastal and fluvial subsurface groundwater-surface water interaction studies. Porewater salinity signals in coastal bulk ER measurements however can be masked by geologic heterogeneities, water depth variation, and a dynamic surface water salinity [*Henderson et al.*, 2010; *Befus et al.*, 2014] which are ubiquitous in coastal environments. This effect is addressed through time-lapse ER surveys, as changes in the bulk ER through time mainly reflects changes in porewater salinity rather than changes in the electrical properties of the sediment matrix with corrections for surface water depth and electrical conductivity [*Swarzenski et al.*, 2006; *Henderson et al.*, 2010; *Dimova et al.*, 2012; *Befus et al.*, 2014].

I studied STE flow and porewater salinity dynamics underneath the Werribee River Estuary from channel to estuary-wide scale by measuring the bulk ER of the channel bed through time. The relationship between cross-channel scale ER variability and hydrologic conditions as well as channel geomorphology was investigated. These relationships were then used to determine porewater salinity dynamics throughout the whole estuary.

3.3. STUDY SITE AND METHODS

3.3.1. Study site background

The Werribee River Estuary is an 8.25 km long narrow salt wedge estuary at the end of the Werribee River located west of Melbourne in Victoria, Australia (Figure 3.1). Estuarine stage fluctuation is tied to the semi-diurnal tides in Port Phillip Bay with a tidal range of about 0.8 m. The average water depth is about 2 m and is deeper towards the mouth. Freshwater flow into the estuary is typically around 10^6 L d⁻¹ regulated by an

upstream weir which is the physical upper limit of the estuary. Annual rainfall over the estuary is about 450 mm but is generally around 1000 mm over the whole watershed. The wettest period is between the months of October to February but there is no well pronounced month to month variability in rainfall. Sediments along the channel are generally muddy in the lower estuary, which is around 4.5 km from the mouth of the estuary. The bottom is firm in the mid and upper estuary consisting of clay or sand, which progressively coarsens to gravel farther upstream towards the weir.

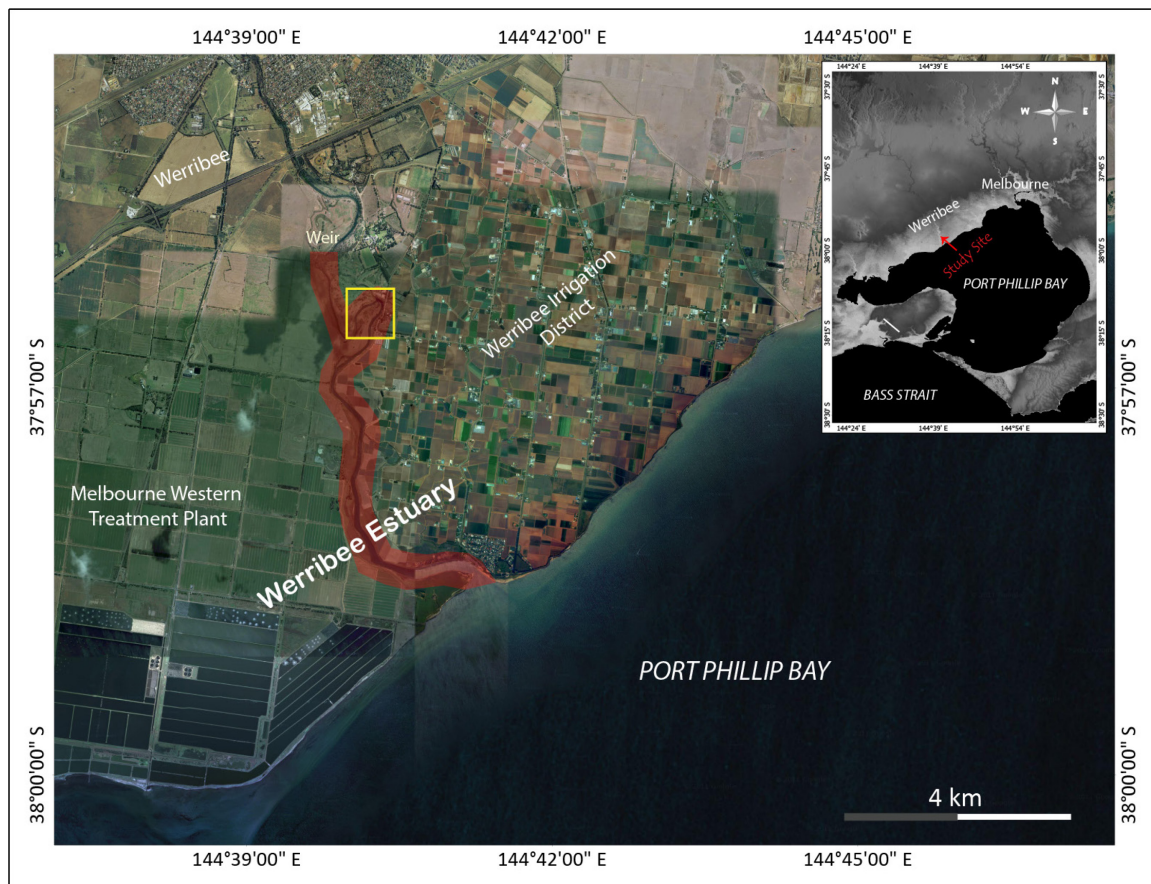


Figure 3.1. Aerial image of Werribee Estuary (highlighted in red). Study reach (yellow box; Figure 3.2). Inset: Port Philip Bay and vicinity.

The Werribee River Estuary cuts through deltaic sequence of the younger Werribee Delta Deposits in relatively flat coastal terrain. Cliffs along the upper estuary exposes sand and gravel channel deposits intercalated with finer grained strata with a general fining upward trend. The exposed Werribee Delta Deposit sequence at the study site is about 10 m above sea level and extends to about 5-8 m below mean sea level based on drill logs close to the study site. Underlying the deltaic sediments are the Newer volcanic deposits, mainly basalt flows, which act as a leaky confining unit over sedimentary strata of the older Werribee Formation. The sand and gravel units within the Werribee Delta Deposits crop out slightly above sea level and continue down to the basalt and serves as the main surficial aquifer tapped for irrigation [Salzman, 2010].

Groundwater recharge in the immediate area surrounding the estuary comes from two main sources, direct recharge from rainfall and irrigation water from the Werribee Irrigation District on the eastern side (Figure 3.1). An estimated 5-10% of the annual rainfall is recharged into the aquifer (Port Phillip and Westernport Groundwater Flow Systems). Li [2012] reported that 10-30% of the recharged groundwater along the east bank plains comes from irrigation water based on oxygen isotope data. Barnett et al. [2005] suggested that treatment lagoons and effluent irrigation also presents an important recharge mechanism along the western bank.

The Werribee delta aquifers have been extensively pumped for irrigation in the last decade resulting in seawater intrusion with the water table dropping dramatically [Barnett et al., 2005]. Recent efforts to regulate groundwater pumping and the use of recycled water to augment irrigation allowed for the water table to recover. However, issues of declining water quality, particularly elevated salinity and nutrient concentration, developed with the use of recycled water.

3.3.2. Field methods and data processing

Fieldwork was conducted in January 2012 along a meandering reach at the upper Werribee River Estuary with a pronounced cut bank and thalweg on its east bank. Piezometers were manually installed along the cut bank (F and G), at the middle of the meander bend (D), along the point bar (H and E), and along the edge of a collapse deposit at the cut bank (A, B and C; Figure 3.2). One inch diameter steel piezometers with a 20 cm screen from the drive point were installed 50 cm below the sediment surface. Arrays of four thermistors attached to a steel rod were placed inside the piezometers. The thermistors were spaced to correspond to depths of 0, 15, 30, and 50 cm below the sediment-water interface. The thermistor arrays measure water temperature inside the pipes which thermally equilibrate within a few minutes (typically <10 minutes) to the external ambient temperature [Cardenas, 2010]. The steel rod was pre-wrapped with electrical tape at each thermistor to reduce measured temperature signal from the rod. The temperature sensors, which are accurate to 0.25 °C and have a resolution of 0.03 °C, were connected to HOBO U12 four channel data loggers. Temperature data were collected for 18 hours taking measurements every 5 minutes. The piezometers were also equipped with vented conductivity, temperature, and depth probes (CTD ; In-Situ Inc. Aqua Troll 200) with sub-centimeter accuracy and 0.25 °C and 0.03 °C temperature accuracy and resolution. CTD sensors were also installed outside of two piezometers (C and B) right at the sediment surface to monitor changes in the surface water level and temperature though time. The location and elevation of the piezometers relative to a pre-set base station were surveyed using a Sokkia SET 610 total station. Temperature and water level data were recorded every 10 minutes by the CTDs. Slug tests were conducted at each piezometer after the removal of the installed sensors at the end of the survey. Each test was analyzed using

AQTESOLV following Bouwer and Rice [1976] and Springer and Gelhar [1991] to determine sediment hydraulic conductivity.

Potential porewater flux across the sediment-water interface was calculated following Darcy's Law:

$$q_z = k \frac{dh}{dz} \quad (3.1)$$

where q_z is the vertical flux with positive values indicating flux out of the sediments and negative values indicating flux into the sediments, k is the hydraulic conductivity of the sediments, and dh/dz is the vertical hydraulic head gradient. The vertical gradient is the ratio of the difference between the water level inside the piezometer and surface water level and the distance of the screened interval from the sediment-water interface, which is at 0.5 m.



Figure 3.2. In-stream piezometer stations and ER transect line. Piezometer labels indicate the sediment substrate. Ponds on the point bar can be seen east of the piezometer locations.

Time-series underwater ER survey was conducted to determine temporal changes in subsurface bulk ER, which reflects changes in porewater salinity. This method assumes that short term changes in the bulk electrical properties are mainly associated with changes in the pore-filling fluid rather than the sediments themselves. The survey was conducted across a segment of the estuary channel trending north to south (Figure 3.2). The ER cable with 56 graphite electrodes spaced every 1.5 m was placed along the bottom of the channel and aligned with piezometers H, E and F. Subsurface ER was collected every hour using an eight-channel resistivity system (SuperSting R8 from Advanced Geosciences, Inc.). A dipole-dipole array mode was used for all of the time lapse ER measurements which is generally sensitive to both horizontal and vertical resistivity changes. Bathymetric survey was done using a Lowrance GPS-Sounder connected to a laptop recording depth and position every 2 seconds. The ER transect profile was extracted from the interpolated bathymetry of the reach.

An estuary-wide longitudinal continuous resistivity profiling (CRP) was conducted prior to the time-lapse survey to determine regional trends in subsurface ER. The same SuperSting R8 system was used for the survey using floating graphite electrodes. An 11 electrode ER cable with 5 m spacing was towed behind a boat collecting ER data every 2 seconds. ER, location, depth, and surface water conductivity along the survey line were collected simultaneously with the SuperSting R8 connected to the Lowrance GPS-Sonar system and a CTD hanging on the side of the boat. The boat was set to cruise at about 0.5 m s^{-1} . The same survey was repeated in August following the January survey track.

Both underwater time-series and CRP data inversion were undertaken using RES2DINV using a robust constraint [Loke and Barker, 1996]. Point measurements of surface water resistivity for the underwater ER survey does not give an accurate representation of the average surface water resistivity due to stratification and separation

of water masses in the estuary. To determine an optimum surface water resistivity, each of the time series data was inverted using a range of surface water resistivity values, the inversion result which best represented the average surface water resistivity during each ER snapshot and typically close to the point measurement values in the field was selected. CRP inversion on the other hand only requires an average surface water resistivity, which averages around 0.4 Ωm during both the January and August survey. Model resolution was also calculated during the inversion to determine how well the modeled ER values represent the actual subsurface electrical signals.

Forward modeling was conducted to further understand limitations in the inversion results and aid in the interpretation of the tomograms. The forward models were created and synthetically surveyed using RES2DMOD [Loke, 1999]. Three zones with different ER were created, with each zone corresponding to sediments having low, intermediate and high porewater conductivity. Archie's Law [Archie, 1942; 3.2] was used to calculate bulk ER (ρ_b) of sediments saturated with different fluid resistivity values (ρ_f) assuming a bulk sediment porosity of 0.4 (n) and a shape factor of 1.3 (m) which is typical of unconsolidated coarse sediments. An additional high resistivity zone representing the basalt layer ($\rho_b = 1000 \Omega\text{m}$) at depths of about 13-15 m was incorporated in the model (Figure 3.3). The conductive zones with a bulk resistivity of 2 Ωm represents sediments saturated with relatively conductive porewater while the resistive block was given a value of 40 Ωm similar to saturated sediments with relatively fresh porewater. The high and low ER blocks are placed on an intermediate resistivity field of 10 Ωm representing sediments with intermediate porewater ER.

$$\rho_b = \rho_f n^{-m} \quad (3.2)$$

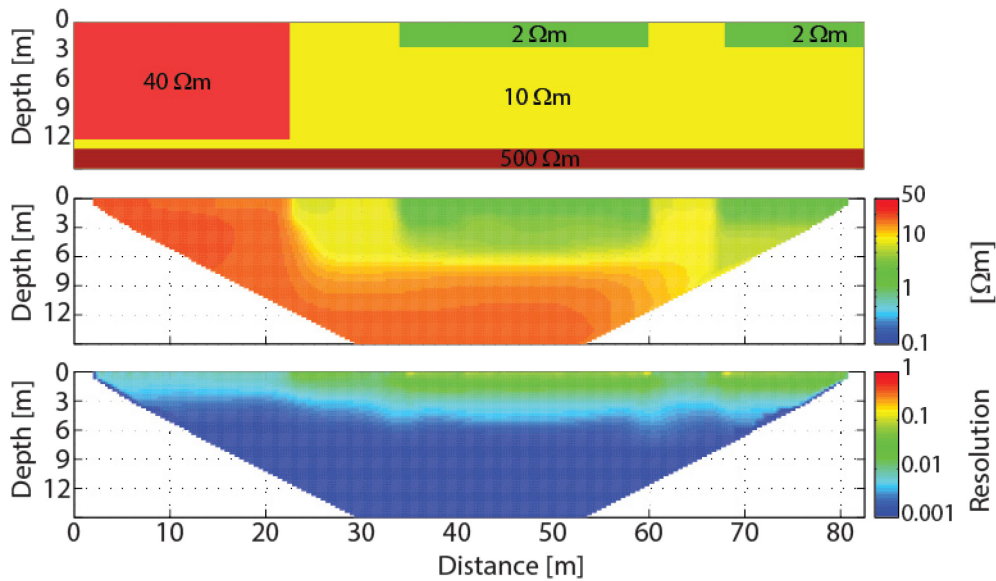


Figure 3.3. Diagram of the 2D petrophysical model with the inverted resistivity section and model resolution. The model includes a 2 meter water layer with an ER value of $0.3 \Omega\text{m}$ (not shown in the diagram).

3.4. RESULTS

In the ensuing discussion, I refer to the west side of the across-channel transect (see Figure 3.2) as the point bar or depositional area and the east side as the cut bank, thalweg, or erosional bank, following convention for meandering rivers.

3.4.1. Subsurface temperature profiles

The estuarine surface water temperature fluctuated between 19.4 to 20.8 °C during the field campaign. These values are well within the annual air temperature range of 8 to 25 °C within the area. Groundwater temperature from boreholes on the east bank ranged from 16 to 18 °C and warmer in summer months based on monitoring data (Figure 3.2; <http://data.water.vic.gov.au/monitoring.htm>). Water temperature inside the in-stream piezometers ranged from 16.6 to 21.5 °C. Thermistor arrays in piezometers B, F, and G have temperature spreads of 2 to 4 °C with temperatures increasing from the bottom sensors to the top. Piezometers A at the edge of a collapse deposit on the cut bank, D at the center

of the channel, and H and E on the depositional bank have 1 °C spreads with the bottom sensors warmer than the ones closer to the sediment surface. Piezometer C values were out of bounds which was likely due to the failure of the logging device during strong winds on the second day of the field campaign.

Temporal trends in sensors installed at 0, 15 and 30 cm from the sediment-water interface generally mimicked the trend in surface water temperature, which was warmer from high to ebb tide and cooler during flood tide (Figure 3.4). During ebb tide after the storm surge, temperatures on the top three sensors in piezometers A, D, H, and E were similar to surface water. Temperatures in these piezometers decreased at low tide with the upper sensors cooling down faster than the bottom thermistors. The sensors at 0 and 15 cm in Piezometer B, installed on the collapse deposit at the cut bank, generally followed the surface water temperature trend whereas thermistors at 30 and 50 cm followed a general decreasing trend. The upper two sensors in piezometer F, which was located on a steep slope along the cut bank, showed similar trends with B but with the bottom thermistors showing a slightly decreasing trend. The upper 3 thermistor in piezometer G followed the surface water temperature trends but with sensors at 0 and 15 cm having higher values relative to the sensor at 30 cm. The bottom thermistor at piezometer G yielded the lowest temperature among all temperature arrays (Figure 3.4).

Estimates of thermal diffusivity using porosities between 20 to 40% assuming sediments composed of mafic minerals were in the order of $2.8-3.8 \times 10^{-7} \text{ m}^2 \text{ s}^{-1}$. Using these values, a 1 °C thermal pulse lasting 12 hours would decay to 37% (e-fold change) at about 6-7 cm below the sediment surface if heat were transported purely by conduction. It follows that the conductive contribution of the pulse at 15, 30 and 50 cm should be 0.13, 0.017, and less than 0.001 °C, respectively.

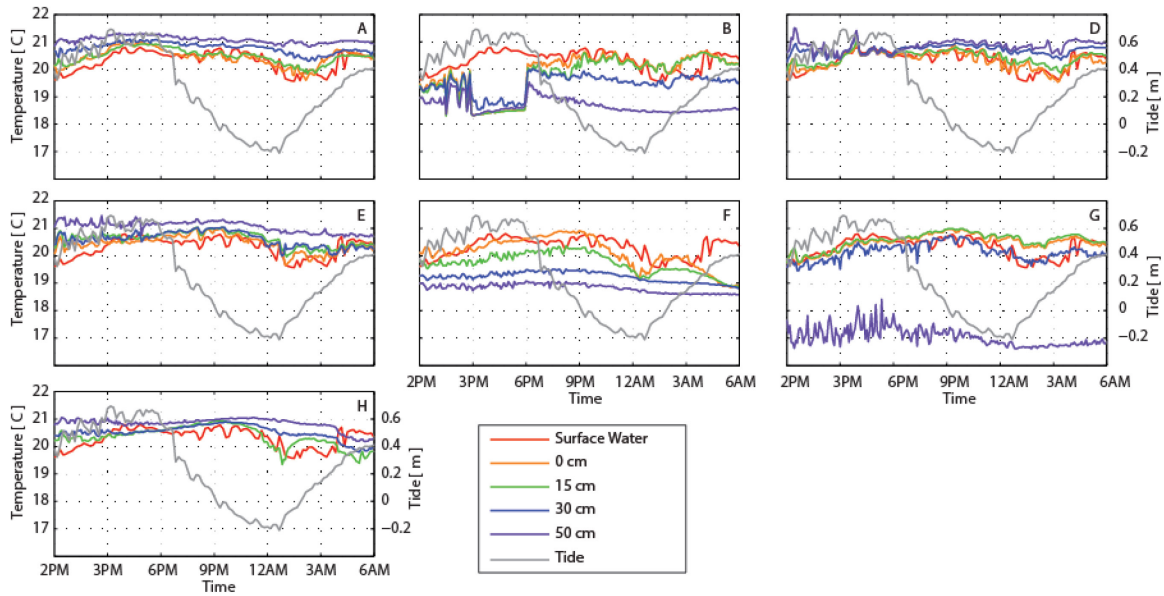


Figure 3.4. Temperature time-series logs in in-stream piezometers. Locations are shown in Figure 3.2.

A storm passed through the site between noon to 6 pm during the 2nd day of the survey (January 11, 2012). Piezometers B (sensor and logger) and D (sensors) were inundated by the surge that occurred at high tide seen as a square temperature anomaly in B and uniform temperature values in D between 3-6 pm. Data on inundated piezometers during the passage of the storm were not included in the interpretation.

3.4.2. Groundwater hydraulic heads, Darcy fluxes, and salinity

Water level inside the in-stream piezometers generally followed fluctuations in the surface water level. Piezometers B, E, G, and H had consistently higher values than surface water through time (Figure 3.5). Piezometers A, C, and D had generally lower water levels but moved above the surface water level after the storm surge.

Sediment hydraulic conductivity estimated from the slug test data varied from 4.1 to 91 m d^{-1} , with an average of 41 m d^{-1} (Table 3.1). These values are typical for sand to gravel sized sediments which were the substrate observed during the piezometer

installation. Potential porewater fluxes ranged from -8 to 42 m d^{-1} with the positive fluxes having higher range of values. Pre-storm surge range for the positive fluxes is 0.05 - 7.6 m d^{-1} and -6.06 to -0.17 m d^{-1} for negative fluxes. The average positive and negative flux before the storm surge are 3.6 and -1.9 m d^{-1} respectively (Figure 3.6). The post storm surge fluxes ranged from -6 and 40 m d^{-1} with an average of 15 m d^{-1} . Piezometers E along the point bar and G at the cut bank, showed the highest positive flux whereas piezometer D at the center of the channel had the highest estimated negative flux.

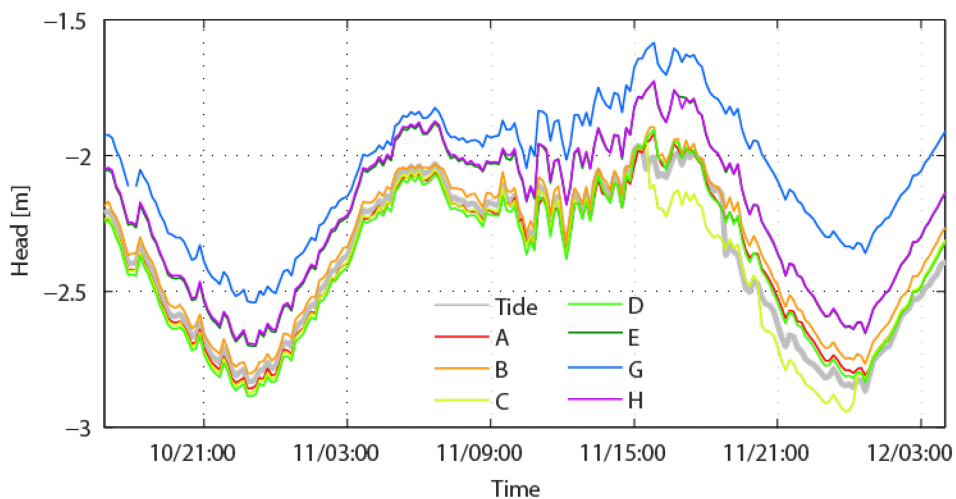


Figure 3.5. Estuarine stage variation for the January survey and water levels inside the in-stream piezometers. Locations are shown in Figure 3.2.

Nested boreholes located 30 m east of the cut bank had water table elevations of 1.86 and 1.54 m above the Australian Height Datum during the January survey. This gives a water table gradient of 0.05 - 0.06 m m^{-1} which yields a flux of about 0.2 - 5.0 m d^{-1} using the hydraulic conductivity range from the slug tests. These are well within the range of positive groundwater fluxes based on the in-stream piezometers particularly the pre storm surge values.

Station	Slug Test 1 [m d ⁻¹]	Slug Test 2 [m d ⁻¹]	Ave. Salinity [ppt]
A	5.9	4.1	6.5
B	61.5	62.4	3.3
C	4.7	5.3	33.4
D	48.6	77	29.0
E	76.3	91	32.4
F	25.3	11.1	-
G	27.9	27.5	1.8
H	61.4	68.9	35.0

Table 3.1. Hydraulic conductivity values from slug tests at each piezometer.

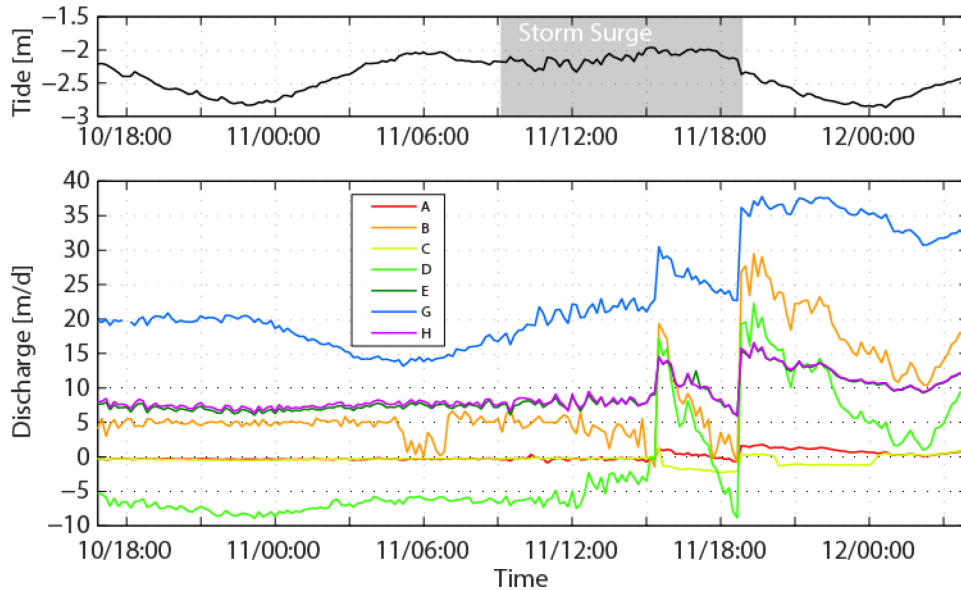


Figure 3.6. Calculated vertical groundwater fluxes from in-stream piezometers. Positive values indicate upward flux while negative values indicate infiltration into the sediments.

The passage of a storm caused sudden fluctuations in the groundwater heads causing the fluxes to spike and drop within a 3 hour span coincident with high tide. Fluxes after this period remained positive in all piezometer stations except for C which was located in a muddy sand substrate.

The salinity inside piezometers A, B, and G were all below 10 ppt whereas C, D, E, and H have values higher than 30 ppt (Figure 3.6; Table 3.1). Groundwater salinity from the boreholes was at 2 ppt whereas estuarine water values ranged between 22 to 33 ppt during the field campaign [Wong *et al.*, 2013]. Salinity values within the piezometers did not vary significantly throughout the field campaign.

3.4.3. Subsurface ER results

3.4.3.1. Time-lapse cross-channel underwater ER

A cross-channel time series ER survey was conducted (January 10-11) to determine reach scale subsurface ER changes with estuarine surface water elevation and flow variability. The bulk ER field shows four general zones of resistivity. The eastern erosional bank shows a highly resistive zone (Zone I) $>10 \Omega\text{m}$ from the bottom of the profile to the sediment-water interface (Figure 3.7a). The resistive zone was persistent throughout the entire time series (Figure 3.7). A low ER zone (Zone II) with values between 0.2-2 Ωm occupies the mid-channel section. Zone II became more conductive with higher estuarine water level but became less conductive at high tide. Another low ER zone (Zone III) was observed on the depositional west bank in the shallowest portion of the section (0.2-2 Ωm). Like the middle conductive zone, this 0.5-1.5 m deep zone became less resistive during higher water level including high tide. Underneath and pinching out at a slope break separating zones II and III is an intermediate resistivity zone (Zone IV) with bulk ER values between 1 to 10 Ωm . This zone was relatively stable throughout the duration of the time series survey but became more conductive towards the center of the channel during high water.

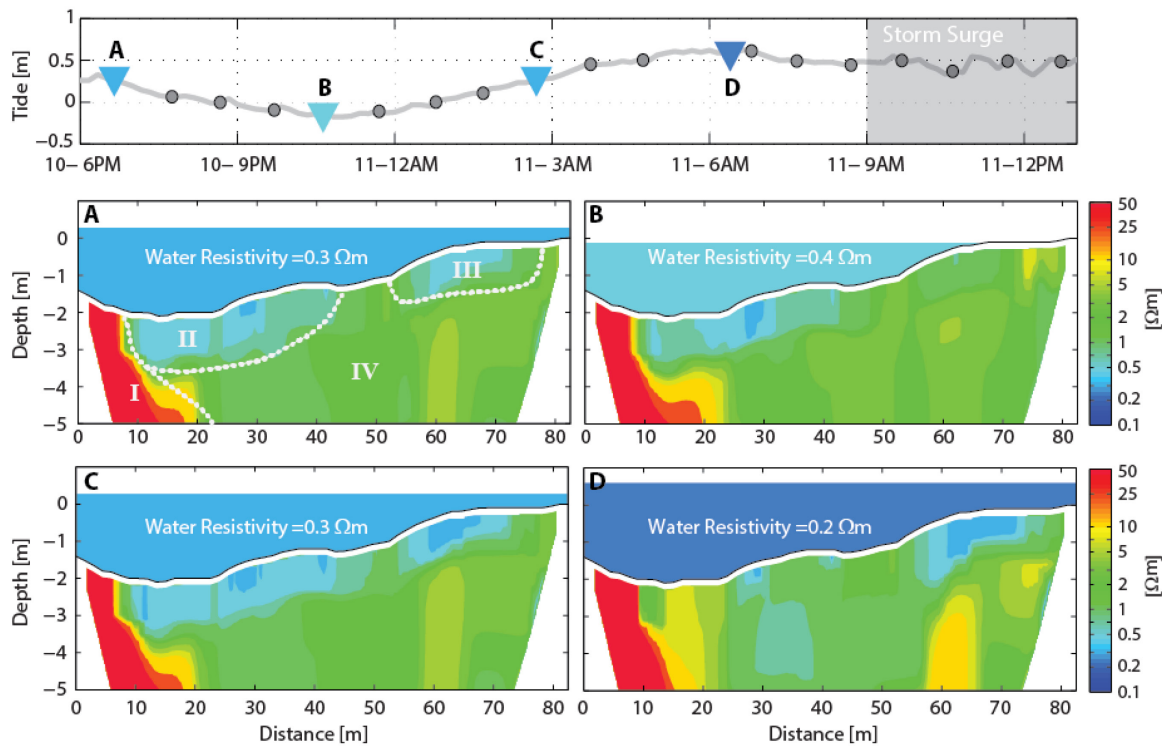


Figure 3.7. Cross-channel ER profiles at different estuary stage (upper panel). A) Mid-ebb tide ER with zone names indicated with roman numerals B) Low tide ER C) Mid-flood tide ER D) High tide ER. The ER value label and color of water column used in the sections are the values used in the inversion and does not depict homogeneity in the water layer. Transect location is shown in Figure 3.2.

3.4.3.2. Continuous resistivity profiling results

A 6 km estuary-wide survey was conducted in January and August 2012 to capture larger scale seasonal changes in subsurface bulk ER (Figure 3.8). Although we followed similar tracks for both surveys the longitudinal bathymetric profiles did not exactly match but showed generally similar depths. This was expected considering a GPS position accuracy of 5-15 meters along a channel with high depth variability. Tidal elevations were at 0.6-0.7 m and 0.8-1.0 m above Australian Height Datum for the January and August campaigns respectively. The longitudinal ER profiles showed a general increase in ER values from the mouth of the estuary to the end of the profile line (Figure 3.8). The increase

occurred around 2.5 km from the mouth of the estuary. ER values of less than 1 Ωm were mostly found in the upper subsurface in January but became more common and penetrate deeper beneath the SWI during the August survey. Segments with ER values greater than 10 Ωm that are continuous to the sediment-water interface were observed in the deeper waters of the estuary beginning from about 2.6 km from the mouth to the end of the transect for the January survey. These high ER blocks appear to be at deeper depth below the SWI during the August campaign (Figure 3.8).

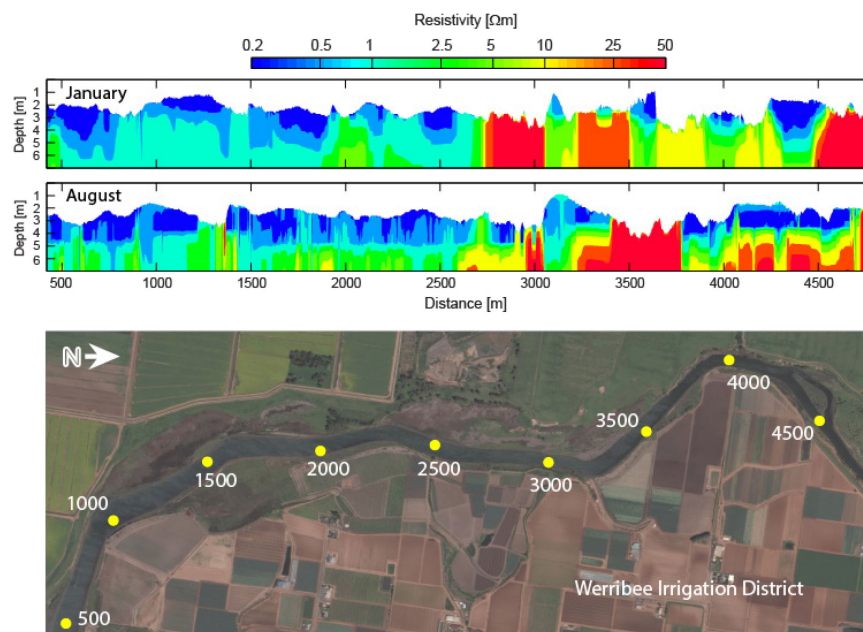


Figure 3.8. Estuary-wide continuous resistivity profiles for January and August 2012. The yellow dots on the image in the lower panel indicate the approximate location along the survey line.

3.5. DISCUSSION

3.5.1. Constraining ER interpretation with forward modeling

A forward model with four different ER zones, corresponding to the imaged zones with a basalt layer (1000 Ωm) around 13-15 m was first conducted (Figure 3.3). The two conductive layers represent sediments saturated with relatively conductive porewater (2 Ωm) while the resistive block was given a value similar to saturated sediments with relatively fresh porewater (40 Ωm). The background resistivity was set at 10 Ωm representing sediments with intermediate porewater resistivity. The inverted idealized profile imaged the conductive zones relatively well however the basalt and the resistive block did not appear to be well resolved. This suggests that the ER surveys cannot distinguish between estuarine sediments with relatively fresh porewater and resistive bodies like basalt layers. The model resolution plot showed a large drop in sensitivity in the lower 5 m of the inverted tomogram (Figure 3.3). Hence the ER interpretations were mostly constrained to within 5 m below the sediment-water interface.

3.5.2. Channel-scale porewater salinity

The high resistivity values in Zone I ($>10 \Omega\text{m}$) east of the channel thalweg is suggestive of either sediments saturated with relatively fresher porewater or the basalt unit underlying the deltaic deposits. The top of the Newer Basalt is at 13 m below sea level based on borehole logs, hence Zone I is likely fresher water saturated sediments (Figure 3.2). The lower salinity and persistent positive groundwater flux values at stations B and G are consistent with a fresh groundwater discharge zone (Figure 3.6). Furthermore, the magnitude of fluxes within these piezometers are also within the expected range based on the gradient estimated from borehole water levels. The low temperature values in thermistors at 50 cm below the sediment bed at location G and F (17-19 $^{\circ}\text{C}$) along the cut bank corroborates the idea of an area of fresh groundwater discharge as groundwater

temperature from the boreholes are at 16.7-16.9 °C. The tidally independent fluxes at locations A and C, also along the cut bank, suggest that estuarine water may also be entering along the shoreline despite the groundwater gradient being inclined towards the estuary from the east bank. These piezometers are located at the tip (A) and upstream (C) of the collapse section that forms a small point bar along the cut bank. The upstream segment of point bars are zones where surface water can enter via hyporheic infiltration even in gaining conditions [Cardenas, 2009b]. Porewater salinity at location C is similar to surface water which indicate entry of estuarine water upstream of the collapse section. Salinity at location A (6.5 ppt) is relatively fresh but slightly higher than B (3.3 ppt) which is at the same location but farther away from the shoreline. This suggests mixing between fresher groundwater and more saline surface water closer to the shoreline at the tip of the collapse sector at the cut bank.

The low ER values in Zones II and III in the middle of the channel and at the shallow area along the point bar indicate sediments with relatively conductive porewater which is likely channel water percolating through the surface sediments (Figure 3.7a). This is evident from the decrease in the bulk ER during higher water level when saltier water is flowing over the channel. The persistent positive fluxes in piezometers H and E approximately along Zone II however, is not consistent with a downward infiltration of estuarine water (Figure 3.6). A more saline groundwater source other than surface water is unlikely as a higher resistivity zone lies beneath Zones II and III. This suggests that saline estuarine water is entering the subsurface through bedforms and discharging where the piezometers are located. Temperature measurements in the upper 30 cm in these piezometers have very similar values with surface water whereas the bottom sensor at 50 cm is warmer and stayed almost constant through the whole time series. Since the conductive temperature penetration is less than 10 cm into the sediments the similarity in

temperature in the upper 30 cm is consistent with the inflow of surface water. Furthermore, an average vertical flux rate of 3 m d^{-1} would flush porewater at 0.5 m depth in about 2 hours which should make temperatures near the sediment surface similar to deeper groundwater. The temperature profiles also suggest a shallow (<50 cm) hyporheic zone along this channel segment. Channel velocities in the order of $5\text{-}20 \text{ cm s}^{-1}$ can induce a hyporheic depth of flow of about 10-50 cm in meter-long bedforms even with ambient upward groundwater flow [Cardenas and Wilson, 2007a]. This is in the same order as the depth of hyporheic zones interpreted based on the temperature and ER data. The scale of hyporheic exchange in this area may be similar to those of channel bedforms like ripples and dunes influenced by channel flow hydrodynamics [Boano *et al.*, 2014].

The bulk ER values in Zone IV underneath Zones II and III suggest sediments with intermediate porewater salinity. The warmer temperature of bottom sensors in the middle and shallow bank suggests a warmer groundwater that is different from the low temperature groundwater on the cut bank (farm irrigation area). The west bank is an elongated point bar with numerous small ponds which are either enclosed or have open connections to the estuary (Figure 3.2). The river connected ponds fill up at high water and slowly drain at ebb and hence may serve as saltier water recharge zones. The enclosed ponds are likely only filled with rain or overtopped during river floods and hence serve as a relatively fresh water source. Both the open and closed shallow ponds warm up during daytime and hence are warmer water recharge sources. The higher water level upstream of the point bar also sets up a larger scale hyporheic flow path across the point bay. Mixing of warmer ponded water and the surface water entering upstream of the point bar is the likely source of the slightly more resistive but warmer temperature groundwater within Zone IV. The presence of recharge ponds enhances the downward groundwater gradient along the point bar which

can bring water recharged from the point bar deeper before coming back up out into the channel.

3.5.3 Estuary-scale porewater salinity

The range of resistivity values in the regional scale survey reflects those of the smaller scale cross-channel ER. The relatively low to high resistivity trend of the longitudinal profile reflects the influence of estuarine water salinity to the sediment porewater in the shallow subsurface. Reports using numerical estuarine flow simulation indicate that the bottom water of the Werribee Estuary remains relatively salty even at higher discharge [Lloyd *et al.*, 2008]. Although clay minerals might be more abundant in the lower estuary, it is several orders of magnitude more resistive than saltwater hence the resistivity trend may be reflective of porewater salinity rather than the relative abundance of clay minerals. The high resistivity blocks coincidental with deeper bathymetry in the upper estuary are within sinuous segments along the channel which are likely areas where lateral discharge of fresh groundwater is focused. Deeper portions at the lower estuary also have a much higher resistivity relative to areas with shallow bathymetry. This is consistent with the observations in the cross-channel scale survey with the high resistivity zone along the deeper erosional bank. Shallow areas with mostly low resistivity values suggests zones where surface water can flow through via hyporheic exchange.

The apparent increase in the depth of conductive zones in the August survey suggest deeper penetration of surface water into the subsurface. This scenario can be caused by a relative increase in flow velocity which enhances hyporheic exchange or a decrease in the water table gradient along the banks of the estuary. River discharge in January was $0.05 \text{ m}^3 \text{ s}^{-1}$ and was slightly higher at $2.3 \text{ m}^3 \text{ s}^{-1}$ in August 2012. Water level data from several groundwater monitoring stations showed only a slight decrease in groundwater level from

January to August (<http://data.water.vic.gov.au/monitoring.htm>). However, the months prior to the January survey had much higher groundwater levels compared to the months prior to the August survey. This indicates stronger fresh groundwater flux in January than in August which would allow more surface water infiltration in the latter month. The higher groundwater level prior to January follows the seasonal rainfall peak which is also a time of frequent irrigation (Nov-Apr). The off-peak irrigation season (May-Oct) is also when Werribee River water is extracted reducing the flow of freshwater into the estuary which in turn reduces the downstream fresher water flow velocity, which ultimately decreases hyporheic exchange. However in estuaries with bi-directional flow, the upstream flow may increase when tides come in which in turn should enhance hyporheic exchange with more saline water. Saltier water can also encroach farther upstream and stay longer in the estuary with lower freshwater input. The longer residence time of denser surface saltwater on top of relatively fresher porewater in estuarine sediments can also induce density-driven flow into the subsurface [*Santos et al.*, 2012b].

3.5.4. Controls on salinity of the subterranean estuary

Channel-scale spatial variability of porewater salinity at the study site is influenced by the near-bank groundwater hydraulic gradient, sources of groundwater, surface water flow, and channel morphology. Higher head gradients on the erosional bank sustain a groundwater discharge zone that is stable on a tidal time scale. Monitoring of radon (^{222}Rn), a geochemical tracer of groundwater, a few hundred meters downstream of the ER transect line yielded consistently high concentrations which increased during lower estuarine stage and decreased during high water [*Wong et al.*, 2013]. ^{222}Rn concentrations measured upstream of the transect were substantially lower confirming the area to be a groundwater discharge hotspot. A steeper and deeper channel also increases the wetted area along the

bank where fresh groundwater can exfiltrate. Mixing of groundwater recharged from ponds on top of the point bar and surface water infiltrating upstream of the point bar allows for deeper penetration of the mixed waters prior to discharge downstream of the point bar (Figure 3.9). This mixed zone is responsible for the intermediate resistivity signal in the middle of the section and the slightly warmer porewater temperature. Variability in the estuarine water level, which dictates the flow direction appears to only impact shallow areas predominated by hyporheic exchange. The inflow of more saline water during rising estuarine water level increases porewater salinity at the upper estuary in the shallow hyporheic zones but does not appear to get flushed out during ebb. Surface water stratification during the January field campaign occurred during ebb to low tide where fresher surface water lie on top of a more saline water in the deeper portion of the channel [Wong *et al.*, 2013]. The effect of this can be observed as a more conductive hyporheic zone in the middle of the channel relative to the shallow hyporheic zone on the depositional bank during mid-ebb and low estuarine stage (Figure 3.8a and 3.7b). Hence hyporheic mixing predominantly controls porewater salinity in shallower segments of reach (Figure 3.9). However, the high ^{222}Rn concentration within the reach affirms the relative importance of groundwater discharge focusing along bend over hyporheic exchange in the shallower part of the reach [Wong *et al.*, 2013].

Estuary-wide porewater salinity is controlled by larger scale channel morphology (sinuosity), estuarine surface water salinity and water table elevation relative to the estuary. The consistent occurrence of high ER zones close to channel bends and deeper waters indicate stronger groundwater discharge along these features. This is likely associated with focusing of groundwater flow towards the apex of sinuous stream [Smith and Turner, 2001]. Cut bank erosion and deepening along outer bends also increases the area where groundwater can seep from (i.e., larger wetted perimeter). The longitudinal increase in

subsurface ER upstream is consistent with sharper bends and steeper cut banks in the mid to upper estuary which promotes fresh groundwater focusing. This is consistent with monitored low ^{222}Rn distribution along the lower estuary, which is thought to be derived from fresh groundwater discharge rather than hyporheic exchange in the WRE [Wong *et al.*, 2013]. The overall decrease in resistivity during the August survey is due to generally weaker groundwater inflow to the estuary, which enhances surface water infiltration. Furthermore, low stream flow in the month preceding the August survey reduced the freshwater input, which enhanced saltwater migration further upstream allowing more time for the surface water to infiltrate. Saltwater also lingers in the lower estuary due to generally deeper waters [Lloyd *et al.*, 2008]. This prolonged salty surface water period may also be conducive for the development of density-driven infiltration of estuarine water.

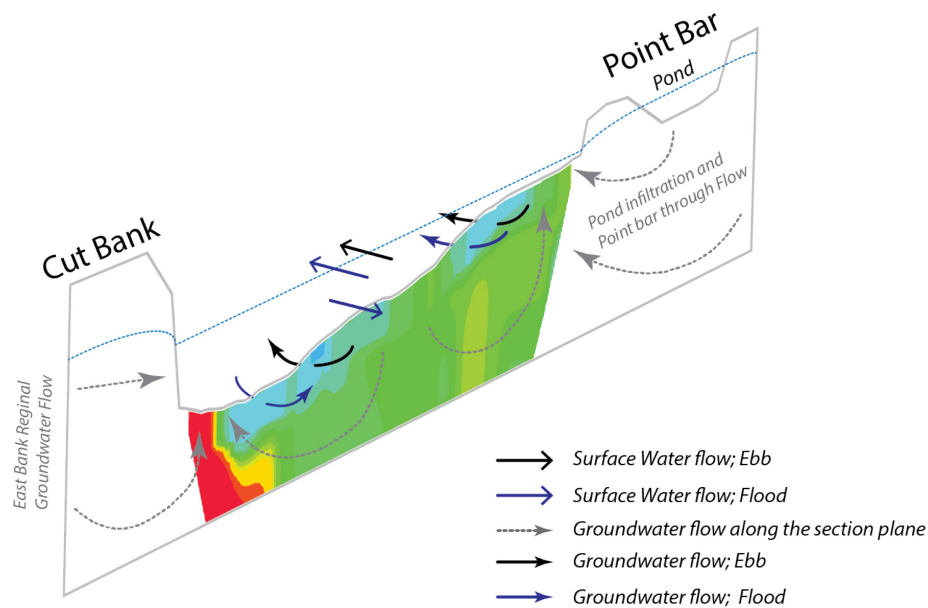


Figure 3.9. Conceptual model of the porewater salinity dynamics across the channel showing groundwater sources and flow paths. Background electrical resistivity section from Figure 3.7A.

3.5.5. Implications for material transformation

There is a great deal of interest in the role of STEs as sites of intense biogeochemical transformation of constituents such as nutrients and greenhouse gases [Kroeger *et al.*, 2007; Santos *et al.*, 2009]. In previous work on the Werribee estuary it has been argued that there is limited transformation of materials coming from regional groundwater discharging to the estuary. This is due to the very constricted nature of the STE as groundwater is discharged rapidly into the estuary [Wong *et al.*, 2013]. The present work shows that whilst there clearly is an STE juxtaposed with a fresh groundwater discharge hotspots, the high groundwater gradient along the cut bank allows for faster pore water velocities which may limit material transformation. Such an observation is analogous to recent work which shows that transport zonation of porewater within ripples can lead to limited transformation of nitrogen within ripples [Kessler *et al.*, 2013]. This highlights the importance of understanding not only reaction and discharge rates within STEs, but also the controls of different scales of geomorphologic, geologic, and hydrodynamic complexity.

3.6. SUMMARY AND CONCLUSION

I investigated porewater salinity dynamics within a subterranean estuary underneath a small river estuary at a reach and estuary-wide scale. Subsurface electrical resistivity was used to infer porewater salinities. Geophysical interpretations were compared with a forward model that accounted for the presence of resistive subsurface features and changes in water depth and salinity. I observed an estuary-wide longitudinal subsurface salinity pattern consistent with the longitudinal surface water salinity structure within the estuary. Deeper channel segments associated with channel bends with cut banks are locations of resistive porewater which represent groundwater discharge hotspots. Shallow channel segments are zones dominated by shallow hyporheic exchange with

shorter (tidal) time scale variability. Seasonal changes in the water table and the strength of freshwater flow within the channel can influence estuary wide porewater salinity. The results of the study highlight the importance of groundwater-surface water interaction and channel geomorphic features on porewater salinity zonation at different scales within an estuary. Understanding porewater salinity dynamics at different scales in STEs can improve our understanding of material transformations and their contribution to measured chemical fluxes from coastal streams.

3.7. ACKNOWLEDGEMENTS

This study was supported by the National Science Foundation (EAR-0955750), the Geology Foundation at the University of Texas at Austin and the Australian Research Council grant DP1096457. I thank Victor Evrard, Vera Eate and Wei Wen Wong for assistance during the field survey. Special thanks to M. H. Loke and Kevin Befus for their invaluable suggestions in the analysis and inversion of the electrical resistivity data.

Chapter 4: Flooding of a subterranean estuary with episodic rainfall

4.1. ABSTRACT

The response of a subterranean estuary to episodic rainfall events along the Bolinao Peninsula in the Philippine Islands was studied. The beach water table, underlain by karstified Pleistocene bedrock with discrete discharge outlets, responded rapidly to strong rain events. Groundwater response was marked by a quick rise in the water table followed by a slow recession. Subsurface temperature profiles, hydraulic head measurements, and ^{222}Rn monitoring indicated consequent elevated groundwater discharge towards the coast. Time-series porewater salinity profiles directly showed the flushing of the STE. This study demonstrates that rapid recharge from heavy rainfall can cause seaward groundwater gradients to rapidly increase that in turn affect the chemical and thermal regime of the STE and potentially deliver dissolved materials like nutrients in large doses to coastal areas. This is similar to material inputs from flooding of rivers and estuaries.

4.2. INTRODUCTION

The mixing zone between fresh groundwater and saline seawater near the land-ocean interface, also known as the subterranean estuary, is an important subsurface feature where both terrestrial and oceanic materials are cycled [Moore, 1999; Slomp and Van Cappellen, 2004]. Fresh groundwater, brackish water, and recirculated seawater from this zone are released through submarine groundwater discharge (SGD) carrying dissolved materials back to the ocean. This process is typically slow but occurs in any coastline where the groundwater gradient is seaward [Burnett *et al.*, 2003] or upward across the sediment-water interface (Chapter 2). Similar to surface freshwater-seawater mixing zones like estuaries, the STE is episodically perturbed by oceanic and terrestrial forces that can disrupt

or displace its biogeochemical functions. Events like storm surges have been observed to raise the hydrostatic head at the ocean boundary that can promote the infiltration of seawater in the STE [Moore and Wilson, 2005; Anderson and Lauer, 2008; Smith *et al.*, 2008; Wilson *et al.*, 2011]. However, on the terrestrial end, perturbations like freshwater flooding from high recharge events such as rainstorms, shifts to wet monsoons, heavy diurnal rainfall, or even artificial recharge associated with agricultural irrigation are rarely observed and studied.

Although the larger scale contribution of groundwater discharge on the quality of coastal waters is usually linked with slower-longer term processes like seasonal recharge cycles [Michael *et al.*, 2005], visible ecological impacts of coastal groundwater discharge are mostly tied with episodic events [Lapointe and Matzie, 1996; Smith *et al.*, 2008; Jiang *et al.*, 2010; Wilson *et al.*, 2011; Santos *et al.*, 2013]. Increased groundwater discharge with heavy rainfall in the Tuckean Swamp in Australia was reported to immediately decrease surface water acidity and also increase the N to P ratio weeks after the event [De Weys *et al.*, 2011; Santos *et al.*, 2013]. Hurricanes passing through Florida delivered high amounts of rainfall which triggered algal blooms by increasing the nutrient discharge associated with submarine springs [Hu *et al.*, 2006]. Hence the frequency of these rapid chemical doses released through coastal groundwater discharge can substantially impact the quality of coastal waters with lasting consequences.

There is a general consensus of increasing extreme rainfall frequencies in many places around the world [Haylock and Nicholls, 2000; Zhai *et al.*, 2005; Goswami *et al.*, 2006; Allan and Soden, 2008; Cai *et al.*, 2014]. Coastal aquifers can respond rapidly to these recharge events especially in places where the shallow aquifer permeability is high or where groundwater preferential flow paths are present [Kim, 2003; Hwang *et al.*, 2005; Burnett *et al.*, 2008; Povinec *et al.*, 2012]. I report field observations of a tropical STE,

located on a beach with sandy sediments mantling a karstified limestone bedrock, as it is flooded with freshwater from several days of episodic rain. My goal is to characterize the sensitivity of the STE to rain events. I address the question: Can and how does an STE flood due to up-gradient or ‘upstream’ forcing and what are its indicators?

4.3. FIELD METHODS

A field campaign was conducted from June 23-30, 2011, which coincided with the beginning of the wet season in the Philippines. The field site is located along a pocket beach underlain by uplifted Plio-Pleistocene coralline limestone [Figure 4.1; *MGB*, 1974; *Maemoku and Paladio*, 1992; *Ramos and Tsutsumi*, 2010]. The site receives an average annual rainfall of 2500 mm which is mainly delivered through episodic rain events like storms during the wet season [*Rivera*, 1997; *Rollón et al.*, 2003]. Surface drainage in the 1 km² watershed is not well-developed with the lone ephemeral stream active only during the passage of strong rain events. Groundwater recharge in the area can be through diffuse infiltration through soils or discrete recharge through karstic features similar to other tropical Pleistocene marine terraces undergoing active karstification [*Jones and Banner*, 2003a, 2003b]. The dominance of the latter mode of recharge is supported by local accounts that water level in caves rises after rain events and with a generally higher groundwater level during the rainy season. Groundwater discharges along the shoreline through springs or offshore through both diffuse and discrete submarine groundwater discharge (SGD).

4.3.1. Porewater Sampling

Porewater salinity is a commonly used tracer for surface water-groundwater exchange in coastal areas where porewater salinities similar to surface water indicate infiltration and vice versa [*Burnett et al.*, 2006; *Robinson et al.*, 2006, 2007b; *Abarca et*

al., 2013]. I installed multi-port porewater samplers along a beach-ocean transect perpendicular to the shoreline and monitored salinity in two time-series sampling campaigns (Figure 4.1). The sampling ports were spaced to collect porewater at 0, 0.15, 0.3, 0.6, 0.9 and 1.2 m below the sediment-water interface. Each port was covered with a fine mesh screen to prevent sediments from clogging the ¼ inch vinyl tubing connected to the ports. Porewater samples were collected every 3 hours during each field campaign which covered rainy and non-rainy conditions. Each campaign encompasses a tidal cycle with samples collected within a span of 2 hours. Twenty six 150 ml porewater samples were collected at each sampling time using a 50 ml syringe. Assuming a sediment porosity of 40% the effective sampling radius is about 7 cm. The salinity of each sample was measured using a conductivity meter.

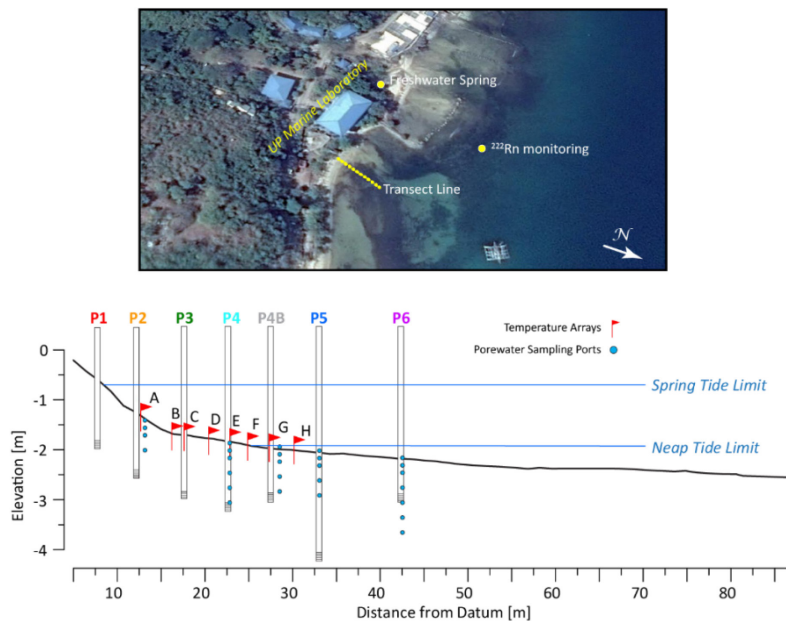


Figure 4.1. Transect profile, piezometer, and thermistor array locations (lower panel). Upper panel showing the beach transect. Refer to Figure 2.1 for a regional map of the study site.

4.3.2. Hydraulic Head and Temperature Measurements

Potential porewater fluxes were estimated by comparing the environmental head in the subsurface relative to the surface water level which represents the head at the SWI. Piezometers were installed along the multi-port transect offset laterally by 2 m and driven between 0.5 to 2 m below the SWI. The screened area for each piezometer was 20 cm long and located at the bottom end. Vented water depth probes with conductivity and temperature sensors (CTD; In-Situ Inc. Aqua Troll 200) with sub-centimeter depth and 0.25 °C and 0.03 °C temperature accuracy and resolution were placed inside each piezometer. CTDs were also installed outside of two piezometers to monitor tidal changes and ambient seawater temperature through time. The instruments were set to collect data every 15 minutes. Topographic data along the transect and at each piezometer was surveyed using an electronic auto-level.

Slug tests were conducted at each piezometer after the removal of the installed sensors at the end of the survey and analyzed using AQTESOLV to determine in-situ hydraulic conductivity of the sediments following Bauwer [1976] for unconfined aquifers. Potential porewater fluxes across the sediment-water interface were then calculated following Darcy's Law:

$$q_z = k \frac{dh}{dz} \quad (4.1)$$

where q_z is the vertical flux with positive values indicating flux out of the sediments and negative values indicating recharge into the sediments, k is the hydraulic conductivity of the sediments estimated from the slug test, and $\frac{dh}{dz}$ is the vertical hydraulic head gradient.

The vertical gradient is the ratio of the difference between the water level inside the piezometer and surface water level and the distance of the screened interval from the SWI.

Subsurface temperature profiles have been widely used to assess groundwater-surface water exchange [Anderson, 2005; Boano *et al.*, 2014]. Temperature logger arrays attached to a steel rod and positioned at 0, 15, 30, 60, and 90 cm below the SWI were installed alongside the piezometer transect offset by 1 m. The steel rods were pre-wrapped with electrical tape to reduce the temperature signal measured by the thermistors. The sensors, which are accurate to 0.25 °C with a resolution of 0.03 °C, were connected to HOBO-U12 four channel data loggers. Temperature was logged every 15 minutes.

4.3.3. Tracing SGD with ^{222}Rn

^{222}Rn was used as proxy for the total groundwater discharge, fresh and recirculated, owing to its significant enrichment in groundwater. ^{222}Rn in seawater was measured from a water supply pump that collects seawater from a pipe at the edge of the narrow shelf in about 5-meter deep water (Figure 4.1). ^{222}Rn concentration was continuously monitored using a radon-in-air monitor (RAD7) attached to a degassing chamber. The degassing chamber was equipped with a thermistor that logs the water temperature sprayed from the top of the chamber. ^{222}Rn in water was measured every hour throughout the field survey. Integrated groundwater fluxes through time were calculated using the method outlined in Burnett and Dulaiova [2003]. Briefly, ^{222}Rn inventories, the average radon concentration within a specified time interval multiplied by depth, were calculated at 3-hour intervals through:

$$Inventory \left[\frac{\text{Bq}}{\text{m}^2} \right] = Rn \left[\frac{\text{Bq}}{\text{m}^3} \right] \times Z [\text{m}] \quad (4.2)$$

The inventories were normalized by accounting for water level changes with tides where incremental change in depth at every time interval was added or subtracted with flooding or ebbing tides respectively through:

$$Normalized\ Inventory \left[\frac{\text{Bq}}{\text{m}^2} \right] = Inventory - Rn \left[\frac{\text{Bq}}{\text{m}^3} \right] \times \Delta Z [\text{m}] \quad (4.3)$$

Above, R_n is the measured radon concentration, Z and ΔZ is the water depth and incremental change in depth with tide respectively. Field conditions were calm during the measurement hence atmospheric losses of ^{222}Rn were deemed to be minimal.

The net ^{222}Rn flux with time was calculated from the difference in the normalized inventory at given time intervals via:

$$Net\ Rn\ Flux\left[\frac{Bq}{m^2s}\right] = \frac{\Delta\ Normalized\ Inventory\left[\frac{Bq}{m^2}\right]}{\Delta t\ [s]} \quad (4.4)$$

^{222}Rn dilution due to mixing with Rn depleted offshore waters, referred to here as mixing loss, was accounted for by adding the highest negative ^{222}Rn flux to the calculated net fluxes. The presence of measurable ^{222}Rn concentrations suggests that benthic flux can compensate dilution which also suggest that the flux estimates are conservative [Burnett and Dulaiova, 2003]. Finally, net groundwater discharge was calculated by dividing the ^{222}Rn fluxes with groundwater ^{222}Rn concentration:

$$Flux\left[\frac{m}{s}\right] = \frac{Net\ Flux\left[\frac{Bq}{m^2s}\right]}{Groundwater\ Rn\left[\frac{Bq}{m^3}\right]} \quad (4.5)$$

4.4. RESULTS

4.4.1. Porewater Salinity

Porewater salinity measurements from the two campaigns yielded values between seawater and groundwater which reflects mixing of these end members in the subsurface. Porewater values ranged from 0.4 to 34 ppt whereas groundwater and seawater were around 0.3-1 ppt and 20-35 ppt respectively. Groundwater salinities were based on the measurements from three shallow wells 10 m away from P1 (Figure 4.1), which is right on the highest tidal elevation, during the field survey. The profiles showed increasing salinity

from close to the groundwater endmember at the bottom to close to seawater values towards the SWI (Figure 4.2 and 4.3). The rainy period which coincided with neap tide yielded higher porewater salinities at deeper sampling ports relative to the second campaign with no rain. The second campaign which was at spring tide had a sharper increasing upward salinity trend with the saltier porewater limited only in the upper 20 cm.

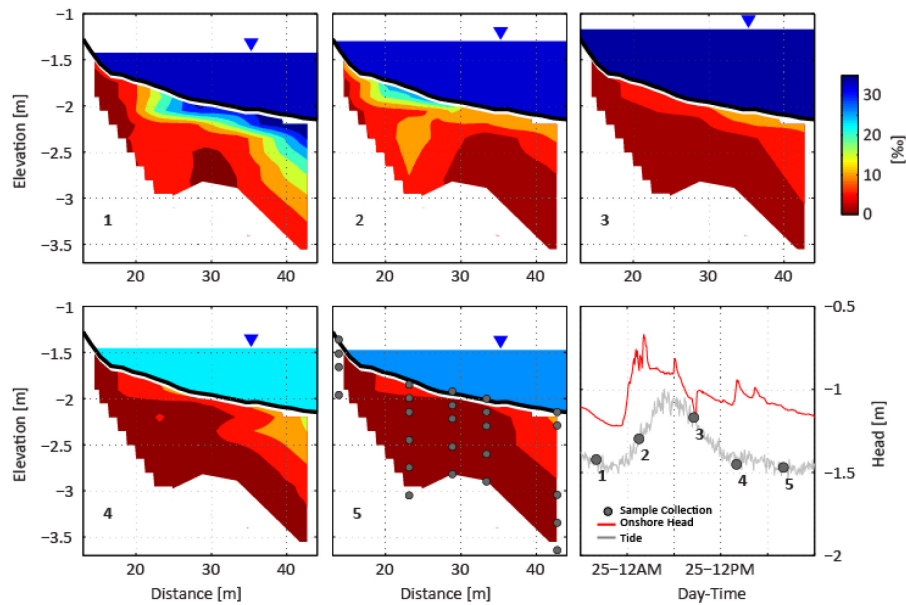


Figure 4.2. Porewater salinity profiles during neap tide with rain events.

A freshening trend was observed for the samples collected during the rainy period even at neap tidal conditions (higher low tide and lower high tide) where sea level is at a relatively high position (Figure 4.2). Salinity values higher than 5 ppt were found in ports deeper than 30 cm during the first two sampling times. The third sampling time (12 hours after the first collection) which coincided with high tide but at the end of a rain event yielded samples which are less than 10 ppt (Figure 4.2). The freshening trend continued at ebb tide where a few more rain events occurred.

During the period with no rain, porewater samples collected deeper than 20 cm yielded values less than 5 ppt (Figure 4.3). Salinity in the upper 20 cm increased with the rising tide and freshened at ebb. Salinities greater than 10 ppt in the upper 20 cm were found only at high tide. Low tide porewater samples were all below 5 ppt (Figure 4.3).

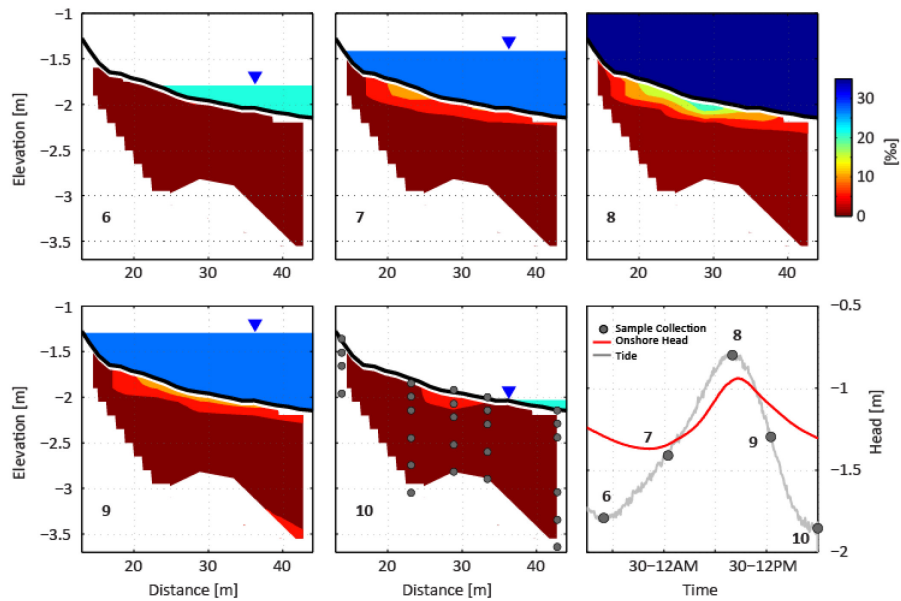


Figure 4.3. Porewater salinity profiles during spring tide.

4.4.2. Groundwater Heads and Potential Fluxes

Groundwater head measurements from the piezometers generally followed trends similar to tidal variations with a slight damping and lag (Figure 4.4). Fluctuations that coincided with rainfall events were observed only at the onshore piezometer (P1). Piezometers 4 and 6, which are 15 and 35 m away from the P1, had consistently higher heads relative to tide level. Piezometer 2 at the upper intertidal zone and 5 m from P1 also yielded values higher than tides that were occasionally exceeded by higher tides. Piezometers 3 and 5 on the other hand had consistently lower water levels relative to seawater throughout the survey period (Figure 4.4). Interpolated hydraulic head profiles

showed a seaward inclined beach water table throughout the field campaign (Figure 4.5). The seawards-inclined water table gradient increased during rain events (Figure 4.5). The water level at P1 responded to at least five rain events and were observed as sharp rises followed by slower recessions. Multiple peaks within a single rain event were also observed which were likely associated with fluctuations in the rain intensity. Piezometers that were inundated by tides (P2-P6) did not show any sharp response to rain events.

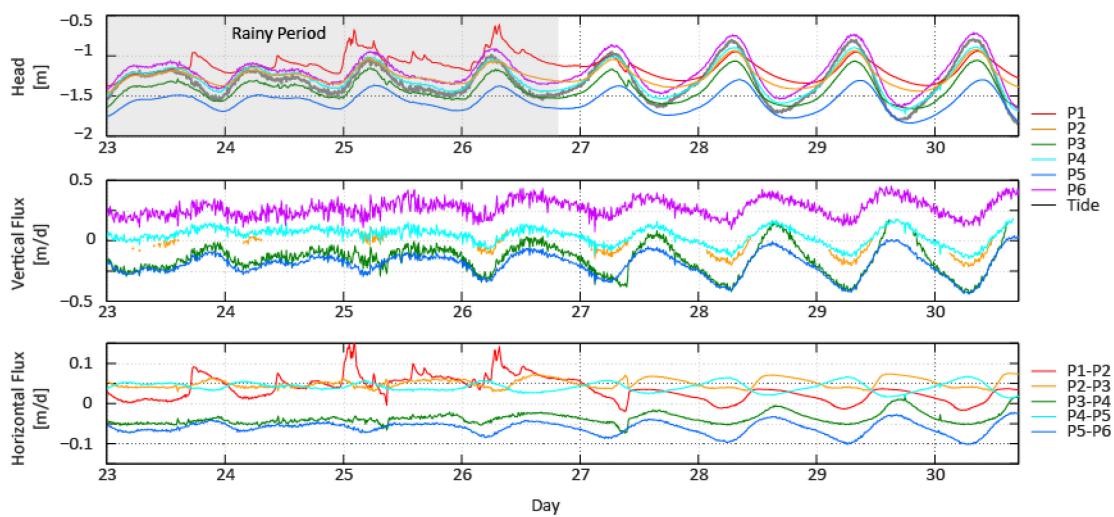


Figure 4.4. Piezometric heads and vertical and horizontal Darcian fluxes through time.

The hydraulic conductivities calculated from slug tests on Piezometers 1, 2, 3, and 4 yielded values of 2.1, 1.9, 1.5, and 0.7 m d^{-1} respectively. Slug test data from Piezometer 5 and 6 were not analyzed due to data logging failure during the test. Using an average hydraulic conductivity of 1.5 m d^{-1} to determine potential vertical and horizontal fluxes from the measured groundwater heads the calculated vertical Darcian fluxes range from -0.5 to 0.45 m d^{-1} where negative values indicate downward flux into the subsurface whereas positive values indicate upward discharge across the sediment-water interface. P6, which is the seaward-most piezometer, maintained positive vertical fluxes throughout the survey

and yielded the highest potential fluxes between 0.25 to 0.45 m d⁻¹. P4 fluxes were also mostly positive during the rainy neap tide campaign and fluctuated between positive and negative during spring tide (Figure 4.4). P3 and P5 both maintained downward fluxes with occasional shift to positive flux at the lowest low water during spring tide. Interpolated vertical fluxes along the transect line showed positive fluxes centered at P4 and P6 throughout the field campaign (Figure 4.6). This suggests a steady discharge of porewater which could be associated with discrete groundwater sources underneath the sediments.

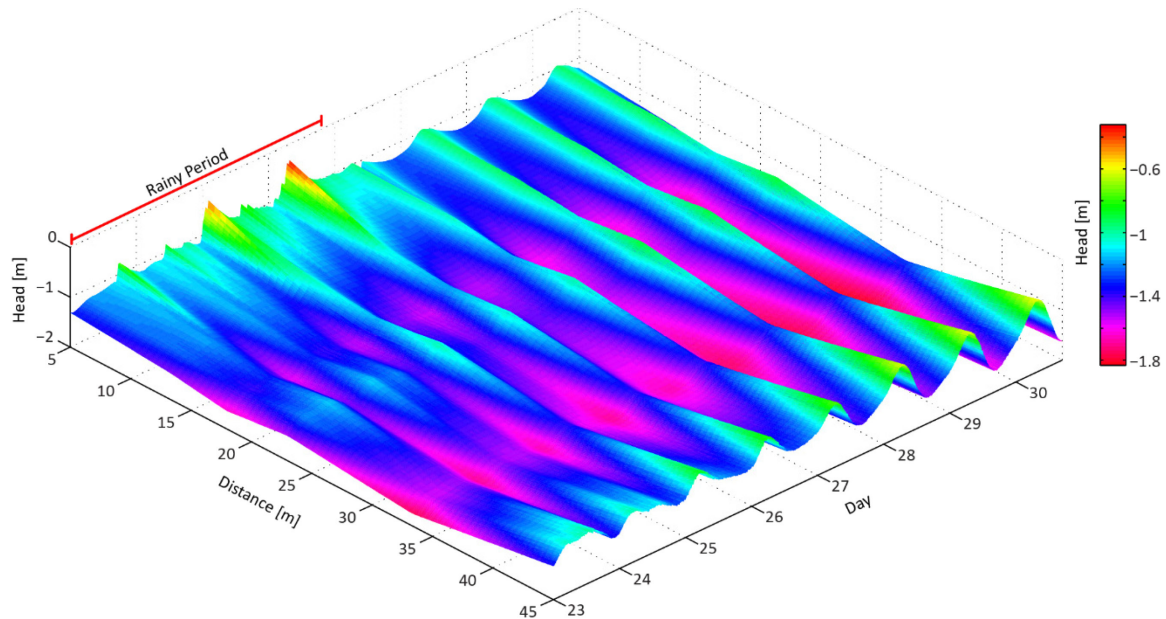


Figure 4.5. Interpolated groundwater heads through time.

The flux potential between neighboring piezometers was also calculated to determine horizontal flow directions and fluxes. Horizontal potential fluxes ranged from -0.1 to 0.15 m d⁻¹ where positive values are directed seaward and vice versa (Figure 4.3). The landward piezometer pair P1-P2 as well as the intertidal pair P2-P3 yielded seaward horizontal fluxes. Lower intertidal pair P3-P4 and P4-P5 yielded potential fluxes directed away from P4 whereas the subtidal zone pair P5-P6 indicated landward flow. The lower

range in horizontal fluxes relative to vertical seepage suggested a vertical gradient dominated system.

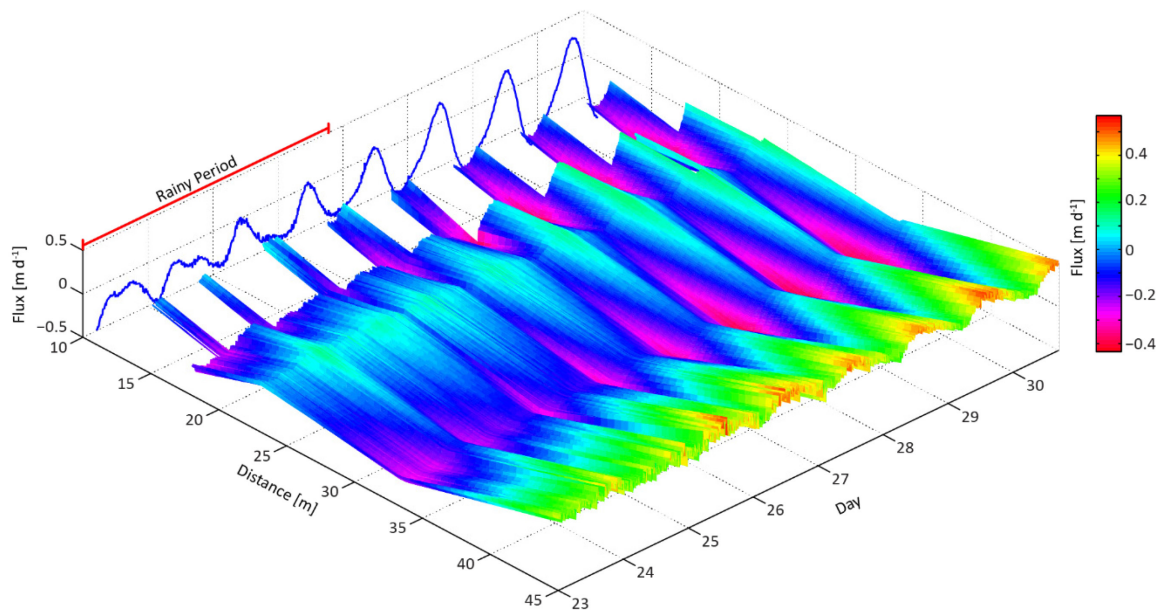


Figure 4.6. Interpolated vertical fluxes through time.

4.4.3. Subsurface Temperature Profiles

Subsurface temperatures fluctuated between 26.5 to 31.0 °C whereas seawater temperature ranged from 25.0 to 33.5 °C. The temperature ranges were well within the air temperature spread between 22.0 to 34.0 °C during the field survey (Weather Underground). Surface water temperatures were lower during the rainy half of the field survey relative to the latter period. This was well reflected by the sensors located at the SWI in all arrays (Figure 4.7). Sensors located at 50 cm below the SWI yielded temperatures between 28.5 to 29 °C whereas sensors at 15 and 30 cm had temperature values generally between the top and bottom sensor temperatures. The boreholes and spring close to the transect line yielded values between 27.8 to 28.4 °C.

Subsurface temperature trends generally followed a well damped profile of the surface water temperature. Sensors at the SWI yielded the highest variability particularly at array A located in the upper intertidal zone close to P2. Sensors located deeper within the sediments had values more similar to the spring and borehole temperature. Surface water temperatures were cooler during the rainy period and steadily decreased towards the middle of the field campaign (Jun 25-27). The trend increased after the rainy period fluctuating diurnally during the non-rainy campaign. Sensors at 15 cm in all arrays also showed a slight decrease in temperature and followed the temperature increase after the rainy period. Sensors at 30 and 50 cm showed similar temporal trends but the variability was only about half a degree.

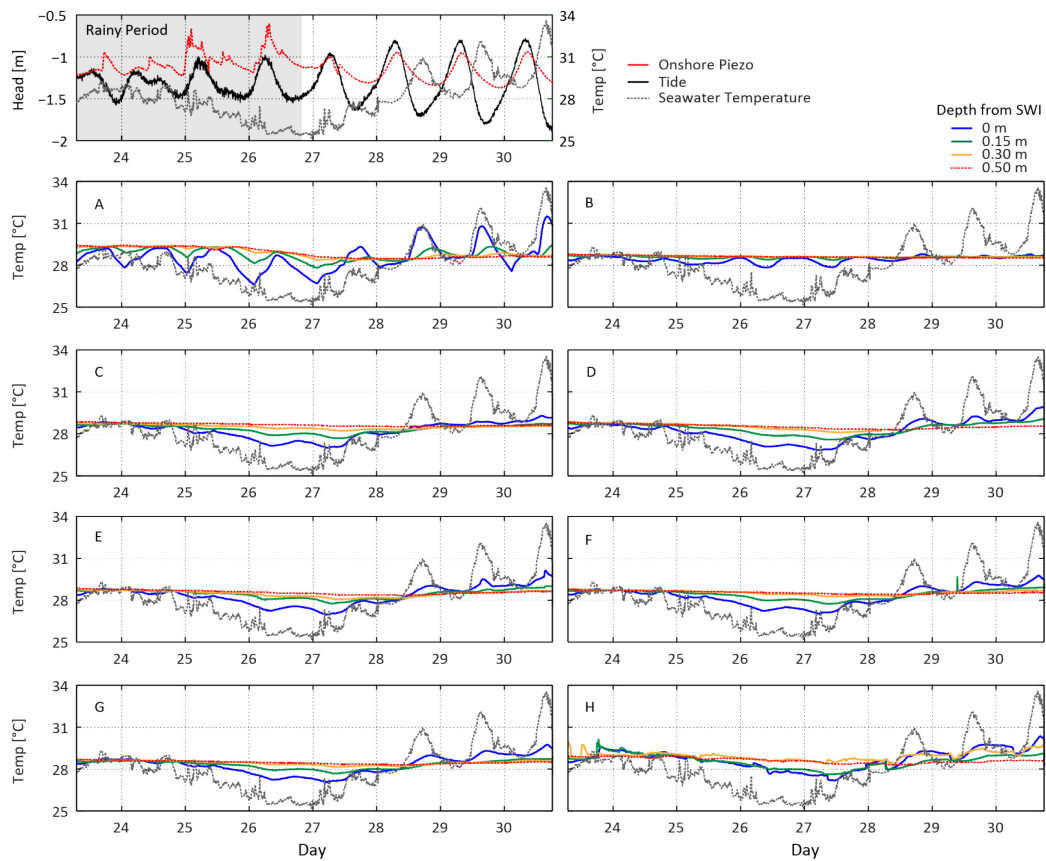


Figure 4.7. Subsurface and seawater temperature profiles.

4.4.4. Rn-based Seepage Rates

Seawater ^{222}Rn concentration measured during the field campaign ranged from 2 to 20 Bq m^{-3} (Figure 4.8). This range is an order of magnitude lower than was previously measured at this site (Chapter 2). This was expected as the location of the pumped water was farther offshore relative to the previous survey. ^{226}Ra measurements yielded values below 2.5 Bq m^{-3} including samples from springs discharging along the shoreline which suggests low contribution from supported ^{222}Rn (analysis conducted by Isaac Santos of Southern Cross University and results relayed through personal communication). ^{222}Rn concentration increased from neap to spring tide with high levels generally observed at ebb during the neap tidal cycle. This trend however was not observed during spring tide.

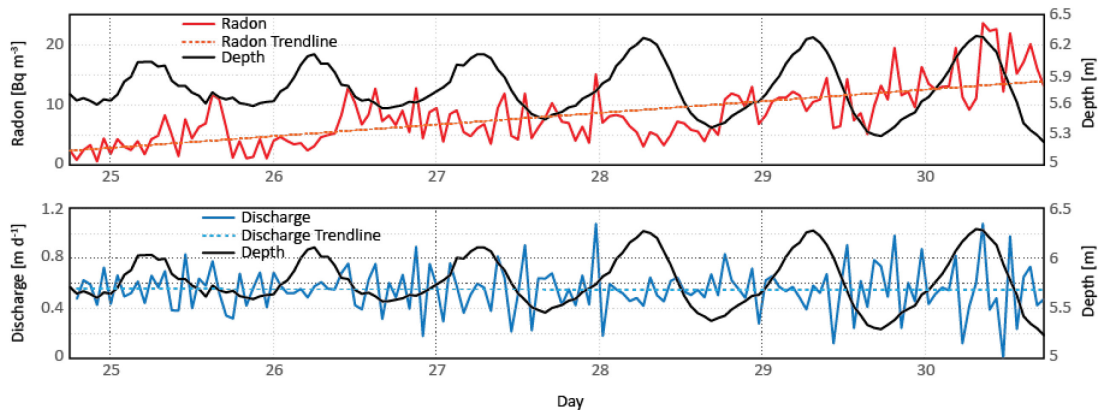


Figure 4.8. (Top) Radon concentration in seawater through time and (Bottom) net groundwater discharge estimates.

Volumetric water fluxes were estimated using the hourly ^{222}Rn measurements. Flux estimates from the measured ^{222}Rn concentration ranged from 0.1 to 1.1 m d^{-1} with an average of 0.55 m d^{-1} . ^{222}Rn porewater values used in the calculation were from seepage meters collected during a separate field campaign which was at $3.0 \times 10^3 \text{ Bq m}^{-3}$. This range agrees well with the estimated potential fluxes using groundwater head measurements. The overall temporal trend did not show an increasing discharge rate with

increasing tidal range (Figure 4.8). However, the seepage rate variability increased towards spring tide.

4.5. DISCUSSION

4.5.1. Subsurface Flow and Sources

The generally seaward-inclined head gradients based on piezometers P1 and P2 in the upper intertidal zone indicates seaward discharge (Figure 4.5). The “outflow gap” which is the width of the potential discharge zone seaward from the shoreline based on Glovers [1959] approximation is about a 6 meters from the shoreline assuming a seaward flux of 0.1 m d⁻¹ and a saturated sediment thickness of 5 m. However, consistently higher heads in piezometers P4 and P6, which are 15 and 30 m away from the high tide line, even at high tide, suggest additional groundwater source that can drive higher groundwater levels aside from the beach water table. Considering a fluctuating shoreline with tides, piezometer P4 being in the lower intertidal zone can be affected by the beach water table gradient however P6 should still be outside the influence of the discharge forced by the beach water table. Karst conduits or discontinuities in the limestone matrix where groundwater can seep out can produce an upward pressure gradient which can elevate the head in piezometers installed within its zone of influence which is likely the case at the study site (Figure 4.9A). Sediments receiving freshwater from discrete seepage from the underlying bedrock have been reported in other areas with fractured or karstified bedrocks [Holliday et al., 2007; Bokuniewicz et al., 2008; Ramessur et al., 2013]. Small springs close to the transect around piezometer P2 were observed during the field campaign which indicate the presence of discrete seepage sources from the bedrock. Furthermore, sand boils were found farther offshore from the high tide line 10 m west of the transect line which corroborates additional groundwater sources. Groundwater heads measured from

piezometers P3 and P5 were consistently lower than sea level suggesting downwelling/infiltration at these locations. Models of groundwater flow around freshwater plumes from discrete zones of discharge develop seawater circulation cells along the boundaries of the plume where seawater can infiltrate into the subsurface (Chapter 2). Recirculation cells at the vicinity of P3 and P5 are also likely present as evident from the consistent downward flux potential.

4.5.2. Enhanced Coastal Groundwater Discharge with Episodic Rainfall

The daily variability of groundwater discharge increased moving from neap to spring tide during the field survey evident from the overall groundwater discharge based on ^{222}Rn and from the potential fluxes based on groundwater head measurements. However, the net groundwater discharge did not appear to change with tidal amplitude (Figure 4.8). Coastal groundwater discharge typically increases at higher tidal range due to the increase in recirculation near the intertidal zone and a lower sea level which increases the seaward groundwater gradient [Robinson *et al.*, 2007a; Santos *et al.*, 2012b]. Although there were no spikes in the ^{222}Rn based groundwater discharge corresponding to individual rain events, the combined effect of these rain episodes may have elevated seepage rates that there was no increase towards spring tide. Rain events have been previously reported to increase submarine groundwater discharge in other places where groundwater flows through preferential flow paths in the bedrock [Burnett *et al.*, 2008; Povinec *et al.*, 2012; Ramessur *et al.*, 2013].

Although the response in the overall groundwater discharge from rainfall events appears to be in the order of days, the on-shore beach water table showed a rapid response to episodic rainfall (Figure 4.4 and 4.5). The elevated heads increased seaward groundwater gradients which increased fluxes out of the discharging beach water table.

This effect is seen in the temperature profiles where closer to groundwater temperatures were measured even with the thermistors at the SWI. Surface water temperatures were lowered by 4 °C during the period with stronger rain events (Jun 26-27) while sensors at the SWI only recorded a 2 °C drop in temperature. This suggests stronger ambient upward groundwater flow maintaining warmer temperatures on sensors exposed to lower surface water temperature. Rapid rises in groundwater heads with rainfall events have been reported in other areas where rapid infiltration is facilitated through preferential flow paths or in sediments with high permeability [Kim, 2003; Sawyer *et al.*, 2014]. The well sorted beach sand in the site with its karstified limestone bedrock presents a scenario where rapid responses to episodic rainfall is likely. Anecdotal accounts from people using the coastal spring close to the study site for their potable freshwater supply suggest increased spring discharge during rain events.

4.5.3. Subsurface Salinity Distribution and Flushing of the Intertidal Mixing Zone

The general upward increase in porewater salinity for both periods (Figure 4.2 and 4.3) indicates that penetration of saltier seawater along the intertidal subsurface forms an intertidal saline plume [Robinson *et al.*, 2007a]. Higher salinities at deeper sampling ports during the first campaign suggests a deeper saline plume development during neap tide. Relatively higher sea level during neap tide with a smaller amplitude of fluctuation may have allowed more time for seawater to penetrate into the intertidal subsurface. The freshening trend observed with succeeding salinity measurements even at higher tide counters the idea of increased seawater infiltration during higher tides. The flushing of the saline plume is likely associated with episodic rainfall which abruptly increased the seaward gradients during this period (Figure 4.5). The typical development of the intertidal saline plume including flushing have been reported on a seasonal [Heiss and Michael,

2014], monthly [Abarca *et al.*, 2013] to fortnightly [Robinson *et al.*, 2007b; Heiss and Michael, 2014] time scale. Here, I observe an intertidal saline plume being flushed within a day with episodic rainfall. Prior to the rainfall events, the relatively high permeability of the beach deposits and neap tidal conditions allowed more time for seawater infiltration which formed the saline plume in the lower intertidal zone (Figure 4.9A). Strong rain episodes increased the seaward gradient which flushed the intertidal saline plume (Figure 4.9B). During the fair-weather period which coincided with spring tide, seawater

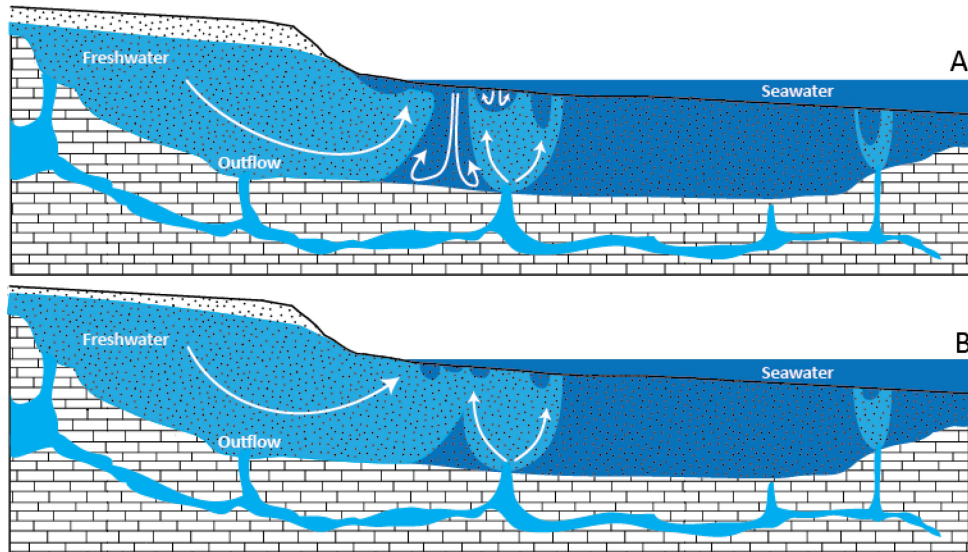


Figure 4.9. Conceptual model of the field site. (A) Fair-weather conditions (B) Flow and salinity distribution after strong rain events.

infiltration was confined in the upper 20 cm occurring only at high tide which was flushed rapidly at low tide. I interpret this relatively shallow infiltration of saltwater in the subsurface during high tide as mixing of denser seawater with the lighter upward flowing fresh groundwater due to salt fingering [Bokuniewicz, 1992; Santos *et al.*, 2012b]. Propagation of the small scale density fingers is in the order of 0.06-0.3 m d⁻¹ based on a

seawater density of 1027 kg m^{-3} and hydraulic conductivities between 1 to 5 m d^{-1} [Gosink and Baker, 1990; Bokuniewicz, 1992]. This puts the leading edge of density fingers between 3 to 15 cm from the SWI from mid-flood to mid-ebb tide which is the depth where saltier porewater was found during spring tide.

4.6. SUMMARY

I captured the ‘subterranean flooding’ response of a subterranean estuary to episodic rainfall events. The karstified Pleistocene bedrock with submarine outlets mantled with permeable beach sediments allowed for a rapid response of the beach water table to strong rain events. The groundwater response was observed as a rapid rise in head with slower recession rate in the onshore piezometer. Head measurements in piezometers along a shoreline perpendicular transect yield water levels that are either consistently higher or lower than sea level throughout the field survey. These observations are consistent with the presence of upwelling freshwater plumes and recirculation cells associated with groundwater flow in sediments underlain by discrete groundwater outflows. Temperature profiles along a line in the intertidal zone parallel to the piezometer transect yield temperatures closer to groundwater relative to seawater which suggest consistent groundwater discharge along the intertidal zone. Porewater salinities showed an intertidal saline plume that was continuously flushed even at high tide during a rain event. The flooding of this subterranean estuary occurred within a day which could have potentially delivered materials cycled within the STE as instantaneous doses in response to the strong rain events. Porewater in intertidal and nearshore subtidal zones remained fresh after the rainy period with seawater infiltration in the upper 20 cm during high tide and flushed rapidly during ebb tide. This rapid exchange is likely associated with “salt fingering” of denser seawater which overlies the fresh porewater in a relatively upward flux dominated

zone. Thus, the episodic flooding of the subterranean estuary from below should also be considered in future studies, particularly those focused on the role of the subterranean estuary in controlling surface and subsurface water quality and biogeochemistry.

4.7. ACKNOWLEDGEMENTS

The Geological Society of America student grant to PBZ and the Geology Foundation at the University of Texas provided financial support for the conduct of this research. I thank Dr. Edgardo Gomez for providing the Rn monitor and for logistical assistance in this study and Dr. Isaac Santos for analyzing the samples for radium. I also thank Nino Paulo Zamora and Jackery Rengel for their invaluable help during the field campaign.

Chapter 5: Biogeochemical Implications

Dissolved materials in groundwater along the land-ocean interface can react with seawater that infiltrates into coastal aquifers [Moore, 1999]. In turn, reaction products can return to the ocean through submarine groundwater discharge (SGD). Thus, it has been recognized that SGD can contribute significant amounts of nutrients to coastal water, which can lead to coastal eutrophication [Johannes, 1980; Moore, 1996; Burnett *et al.*, 2003]. Both the absolute and relative concentrations of Nitrogen (N) and Phosphorus (P) are of particular interest as they are essential nutrients for primary producers in surface waters. The ratio of these nutrients determines which component is limiting, which can also control the rate of primary production. The concentration of N and P in SGD is controlled by (1) the sources of N and P, (2) the redox condition in the coastal aquifer, and (3) the residence time of groundwater [Slomp and Van Cappellen, 2004].

Natural sources of N and P in coastal aquifers mainly come from leaching of soils and decay of aquifer organic matter. These typically contribute N and P at lower concentrations. Additional P can be released from Fe-oxides under reducing conditions and chemical weathering of aquifer solids. Higher concentrations of N and P come from anthropogenic sources including fertilizers, sewage and, leachate from animal manure. Atmospheric contribution of N may only be possible in extreme cases like acid rain in highly urbanized areas.

The generally oxic condition in the vadose zone renders N species entering the phreatic zone to be in the form NO_3 and P as PO_4 . Nitrate is often transported conservatively in oxic aquifers and later removed through denitrification in the absence of oxygen when organic carbon is readily available. Ammonium (NH_4) N in groundwater typically occurs in more reducing conditions with significant enrichment possible only through direct input of high NH_4 leachate. Phosphate concentrations in well oxygenated

aquifers attenuate rapidly due to sorption and co-precipitation with dissolved Ca, Al and, Fe. Under anoxic conditions PO_4 is removed at a slower rate and is generally mobile when the soil removal capacity is exceeded. High ionic strength fluids can induce ion exchange and release sediment bound PO_4 .

Groundwater flow path length and velocity influences the residence time of nutrients in groundwater. Higher residence times in longer flow paths or low pore fluid velocities allow more time for microbially-mediated reactions like denitrification to occur. Furthermore, the different rates of removal and mobility of NO_3 and PO_4 with the redox condition of the aquifer cause changes in the N:P ratio throughout the flow path prior to discharge.

The succeeding discussion in this chapter considers hypothetical scenarios that highlight the biogeochemical implications affected by different groundwater flow and mixing regimes in coastal aquifers where there are different redox states of groundwater and seawater. Unless otherwise stated, the discussion takes a general case where the groundwater end member is naturally supplied with C, P and N with a generally oligotrophic seawater end member.

5.1 DISCRETE GROUNDWATER UPWELLING ZONES

The dynamic flow and salinity in sediments with groundwater upwelling studied in Chapter 2 present a condition where freshwater from a relatively longer flow path discharges as vertical plumes with seawater recirculating along the plume boundaries. In a system where the upwelling rate is constant with no tides, the interaction between freshwater and seawater occurs along a constant but narrow mixing zone. Hence, the nutrient transformations and fluxes across the sediment water interface are dependent on the diffusion of solutes through the mixing zone. On the other hand, permeable sediments

with seasonally changing groundwater upwelling rate and tidal influence are systems where mixing is generally dispersive from the seasonal expansion and contraction of the freshwater plume and the smaller scale changes in the upper edge of the plume with tides. The generated mixing zone becomes wider when the plume contracts and flushed with freshwater when the plume expands.

Well oxygenated conditions in both freshwater and recirculating seawater in a steady state system will have NO_3 as the primary form of N released through the freshwater plume and the recirculating cell. Correspondingly, the transport of NO_3 in the mixing zone and across the sediment water interface will be conservative. The concentration of PO_4 will be small relative to NO_3 as longer residence times and oxic conditions enhance the adsorption and co-precipitation of PO_4 . Hence, the N:P ratio of the SGD from both the freshwater plume and the mixing zone will be high. Higher but constant upwelling strength only widens the freshwater plume but does not affect the cycling of N and P. The N:P ratio only decreases in this system when a high PO_4 source is present. A dynamic upwelling system with oxidizing conditions in both end members will also have NO_3 and PO_4 as the main N and P component. The increase in salinity of the mixing zone when the freshwater plume contracts can release PO_4 sorbed in Fe-oxides which increases the PO_4 concentration in the mixing zone. This decreases the N:P ratio released through SGD from the mixing zone when the freshwater plume begins to expand.

In conditions where the upwelling freshwater is oxic and the recirculating seawater is anoxic in eutrophic coastal waters at steady state, NH_4 and PO_4 are supplied to the mixing zone by seawater recirculation whereas NO_3 comes from the freshwater plume. NH_4 is oxidized and subsequently denitrified along with the NO_3 coming with the freshwater plume. PO_4 from the plume in cases with high groundwater P supply will behave conservatively as it is not efficiently removed in anoxic high ionic strength conditions. N:P

in the mixing zone SGD for the steady state case may be generally low depending on the N and P concentration of the groundwater source. A dynamic upwelling system in this redox scenario will have enhanced nitrification and denitrification when the plume is contracting as the mixing zone widens. Relatively low N:P porewater is released across the SWI above the mixing zone when the plume expands. Some tidal variation in the N:P may be observed as seawater infiltrates and mixes with the upwelling groundwater just beneath the SWI at high tide with low N:P porewater flushed out during low tide.

In conditions where groundwater is anoxic and with a high supply of N and P, typically in wastewater leachate, and seawater is in a well oxygenated state, NH_4 and PO_4 become the dominant form of N and P in the freshwater plume and NO_3 in the recirculation cell. Coupled nitrification and denitrification at the boundary of a steady state plume may proceed whereas PO_4 is adsorbed and precipitated. The N:P ratio of the porewater in the mixing zone in this scenario may also vary depending on the supply of N and P from the freshwater end member but may be low in most cases as PO_4 removal is inefficient in anoxic systems [Slomp and Van Cappellen, 2004]. During the contraction of the dynamic plume, oxygenated seawater mixes with anoxic freshwater with high NH_4 which enhances nitrification-denitrification. When the plume expands, low N:P porewater is released along the mixing zone SWI.

When anoxic groundwater meets anoxic seawater, both end members will have high NH_4 and PO_4 in both the seawater recirculation cell and freshwater plume. N and P will travel conservatively in the steady state system, with the N:P ratio of the discharged porewater following both seawater and groundwater concentrations. A contracting and expanding freshwater plume would not enhance the release of PO_4 as the removal efficiency is low in both end members. Coupled nitrification and denitrification is also

hindered as oxygen is limited in both freshwater groundwater and seawater. The N:P ratio will be similar to the source concentrations as with the steady state system.

The overall impact of this system on the nearshore biogeochemistry may be similar to the typical mixing zone along shorelines. However, offshore upwelling zones discharging in relatively oligotrophic shelf waters can have a significant impact in the immediate vicinity of these freshwater upwelling plumes. The effects are particularly significant in cases where anoxic groundwater limited in organic C and high NH_4 and NO_3 is released to a relatively oxic environment similar to the study site in Chapter 2. This scenario induces conversion of NH_4 to NO_3 which is the more preferred species of N by primary producers. This is supported by anecdotal accounts from the local staff of the Bolinao Marine Science Institute where the study was conducted where they observed a persistent bloom of blue green algae year round along the vicinity of submarine springs.

5.2 SUBTERRANEAN ESTUARY UNDER AN ESTUARY

Different salinity zones in aquifers adjacent to surface estuaries are biological niches that have corresponding biogeochemical functions. In Chapter 3, hyporheic zones, groundwater discharge hotspots, and deep mixing zones were identified as distinct subsurface salinity zones in the subterranean estuary under the estuary.

Zones close to the sediment water interface (SWI) where hyporheic exchange predominates such as sediment bedforms or riffles in shallow areas would have both the geochemical and physical characteristics of the overlying estuarine water. However the lower rate of fluid flow in the aquifer relative to the surface water imposes a lag in both the physical and geochemical characteristics of water going through the hyporheic flow paths. This lag allows the development of steep geochemical gradients within the hyporheic flow paths and across the SWI.

Well oxygenated conditions in both river and seawater with the availability of C in the sediments would allow nitrification to occur in the hyporheic zones but would hinder denitrification since oxygen is present. This makes the sediments a net source of NO_3 . PO_4 is generated with the decomposition of organic matter but will be attenuated rapidly with the enhanced removal efficiency of P in oxic conditions. The encroachment of seawater at high tide will increase the ionic strength of the overlying water which could release sediment bound PO_4 . The net N:P ratio in water exiting hyporheic flow paths may be high as generation of NO_3 will likely predominate.

In scenarios where the freshwater is oxic and seawater is anoxic with ample supply of C from the sediments, nitrification will generate a higher concentration of NO_3 in the porewater whereas PO_4 will be mostly sorbed in the sediments during low tide. During the rising tide, the prevalence of anoxic surface waters would allow denitrification to occur at the infiltrating front of the anoxic seawater and flush the existing NO_3 -rich porewater from the hyporheic zone. Sediment bound PO_4 will be released enriching porewater with P. This scenario produces relatively high N:P water in the hyporheic zone as the NO_3 rich porewater is replaced by the incoming anoxic seawater. N:P then becomes lower as the front of the infiltrating seawater reaches the end of the hyporheic flow path. This process is reversed at lower tides when fresher oxic river water overlies the hyporheic zones.

The condition where fresh river water is anoxic and seawater is oxic will have NH_4 as the predominant species of N, whereas PO_4 will be transported conservatively in the hyporheic flow paths during lower tide when river flow overlies the hyporheic zones. Incoming oxygenated seawater during higher estuarine stages will flush the high NH_4 and PO_4 -rich porewater, with coupled nitrification and denitrification occurring at the infiltrating front within the hyporheic zone. Although removal efficiency of PO_4 increases with oxic conditions, the high ionic strength of seawater may leave PO_4 in solution. At the

beginning of low tide, low N:P porewater is released from the hyporheic zone and eventually replaced by higher N:P anoxic freshwater.

Anoxic conditions in both freshwater and seawater will have NH_4 and PO_4 dominating the hyporheic zones. At low tide when fresh river water flows over the sediment surface, NH_4 and PO_4 will travel conservatively through the sediments with some PO_4 still sorbed in sediment particles. When seawater is flowing over the estuary, more PO_4 is unbound and slightly lower N:P water is released in the hyporheic zone. However, the overall N:P will be mainly dependent on the N:P of the freshwater and seawater end members.

Groundwater discharge hot spots in estuaries, either produced from channel morphology-focused groundwater flow or through local preferential flow paths, represent a condition where an outcrop of the aquifer is juxtaposed with surface water processes. This also provides a system where the geochemical components of groundwater are conservatively released through SGD due to a much high groundwater flux rate. This condition does not allow much time for nutrients to transform at the SWI except during very high estuarine stages that can overcome the estuary-ward groundwater gradient [*Wong et al.*, 2013]. Hence N:P in groundwater discharge hotspots depends on the aquifer redox condition and supply of C to groundwater.

The zone underneath the hyporheic exchange-dominated shallow areas and juxtaposed with groundwater discharge hotspots is the mixing zone of the subterranean estuary under an estuary. Porewater in this mixing zone is released along the SWI through a density-driven cell that begins in the middle of the channel and ends close to the shoreline [*Smith and Turner*, 2001]. This mixing zone integrates the average salinity of surface water infiltrating through the larger scale hyporheic zones (point bar in Chapter 4) with the fresh groundwater from the banks (point bar ponds in Chapter 4). Since the mixing zone would

have deeper and longer flow paths, N:P trends may be more seasonal in nature. If both groundwater and estuarine water are well oxygenated, the mixing zone would be nitrifying closer to the SWI and become denitrifying deeper into the flow path, while PO₄ is rapidly attenuated. Hence, the mixing zone is a nutrient sink in a relatively oxic system.

When one end member is oxic and the other anoxic with ample supply of C, the mixing zone will have coupled nitrification and denitrification close to the SWI, effectively removing N in the system. PO₄ is released to the porewater and travels conservatively through the mixing zone. This results in a system with a relatively low N:P.

In a system where both estuarine water and groundwater are anoxic and organic C supply is not limited, NH₄ and PO₄ will be transported conservatively through the mixing zone. N:P in the mixing zone will depend on the relative concentration of both nutrients from the source.

The impact of this subsurface zonation on the biogeochemistry of estuarine waters also depends on its trophic status. Estuaries experience shifts in their limiting nutrient with seasonal changes in the estuarine water hydrodynamics. A river dominated system would be more P limited and vice versa. Hence, the sources of N and P in groundwater and how they are cycled through the mixing zone is likely to have significant impact on estuarine water biogeochemistry. Hyporheic zones in general, including the shallow areas close to the depositional bank at the Werribee Estuary, would have a more dynamic nutrient flux composition relative to the groundwater discharge hotspots which should be a persistent source of nutrients. The mixing zone between the hyporheic and groundwater discharge zone would have a more seasonal nutrient flux variability.

5.3 FLUSHING OF THE INTERTIDAL SALINE PLUME

In Chapter 4, the rapid attenuation of an intertidal mixing zone was observed with episodic rainfall. The flushing was initiated by the rapid rise in the beach water table with rain water rapidly infiltrating the permeable beach sediments. The system is a scenario where a relatively well-oxygenated but nutrient-deficient rainwater interacts with a groundwater-seawater mixture.

Rain water is relatively oxic with trace amount of N as NO_3 . In conditions where the saline plume in the intertidal subsurface is generally oxic, N will be in the form of NO_3 which is released in a conservative manner across the intertidal zone. In a scenario where the intertidal saline plume (ISP) is anoxic, infiltrating rain water can interact with NH_4 and PO_4 rich porewater. This interaction can promote the conversion of NH_4 to NO_3 where rainwater is in contact with the recirculating seawater. PO_4 may also be slightly attenuated with increasing oxygenation. However, the relatively rapid rise of the water table increases porewater advection rates and decreases mixing time between rainwater and salty porewater, which in turn will minimize interaction. As a result, conservative flushing of N and P will dominate the system in either case.

The impact of this rapid release to coastal waters depends on the trophic state of the nearshore waters. If the coastal water is generally oligotrophic and typically N limited, the released ISP plume where both the interacting seawater and groundwater are oxic will release porewater with a relatively high N:P ratio which can trigger algal blooms. If the ISP system is a mix of anoxic groundwater and oxic seawater, which makes N:P in the ISP low due to coupled nitrification-denitrification, then the released water will be enriched in PO_4 . PO_4 may not be limiting in nearshore waters but may be significant in estuaries which are more P limited. In a scenario where the ISP is anoxic with high NH_4 and PO_4 concentrations, the conservative release of these nutrients might not induce a significant

impact on coastal water biogeochemistry. However, the infiltrating oxic rain water will induce nitrification and denitrification which can reduce N concentrations after the initial episodic rainfall pulse is released.

Because infiltrating seawater in the intertidal zone mixes with air as it drains into the mixing zone, intertidal saline plumes are generally well oxygenated. Thus, the process of nitrification and denitrification may be typical, which renders the system an N sink. Rapid recharge from episodic rainfall and the subsequent flushing of the intertidal mixing zone short-circuits this coupled process which could release more N as NO_3 to coastal waters.

Chapter 6: Summary

6.1 SYNTHESIS

Groundwater-surface water mixing zones or “subterranean estuaries” are coastal subsurface features where terrestrial and oceanic materials can react and transform. Although aquifer characteristics and primary forcing mechanisms such as waves, tides, and seasonal recharge variability in coastal watersheds influence groundwater-seawater mixing dynamics, local geologic, geomorphic and hydrologic heterogeneities modify these dynamics and the associated exchange fluxes across the sediment water interface.

This thesis investigates scenarios that are local in nature but have geographically relevant implications. In Chapter 2, I explored the mixing dynamics related to the occurrence of groundwater upwelling in sediments which are not spatially continuous as typical alongshore groundwater discharge but may be ubiquitous and far reaching, cutting across the shoreline to the shelf edge. This type of system brings subterranean estuarine processes farther offshore which can impact the biogeochemistry of the overlying coastal waters. In Chapter 3, I studied the effect of geomorphology and surface water hydrodynamics on porewater salinity and temperature in a subterranean estuary under a small river estuary. These small coastal catchments have been reported to generate significant nutrient load to coastal waters which are either internally cycled within the surface water estuary or exported out into the ocean [Destouni *et al.*, 2008]. I monitored the response of the intertidal subterranean estuary in Chapter 4 with episodic rainfall. The potential of this mechanism in delivering a high dose of dissolved materials like nutrients or essential dissolved metals in coastal waters can substantially change the biogeochemistry of nearshore waters, with potentially significant consequences such as triggering algal blooms that can lead to coastal water anoxia.

6.2 KEY FINDINGS AND RECOMMENDATIONS

I find that upwelling in sediments underlain by discrete groundwater outlets develop freshwater plumes and seawater recirculation cells along the boundary of the plumes. STEs that form along the plume and recirculation cell boundary are influenced by tides, upwelling variability, and to a lesser extent the thickness of the sediments. Future studies should include sensitivity studies of this mixing system to aquifer properties such as dispersivity and permeability the lack of which was a limitation of this study. Furthermore, the effect of discrete seepage aperture size and density should be explored as they may be important controls of mixing zone and freshwater plume geometries.

I also find that channel meander cut banks are zones where fresh groundwater discharge can be persistent whereas point bars and straight channel reaches are dominated by hyporheic exchange. Future research should look into the effect of bidirectional current flows over different scale bedforms also accounting for variation in fluid density with changing salinity. Although this aspect was originally planned for this thesis the computational and time requirements for such work were beyond the scope of this research and hence recommended for future work.

I observe the flooding of the intertidal STE within a 24 hour period which was previously observed to wane on fortnightly to seasonal time scales. Future studies should look into the sensitivity of the intertidal mixing zones to aquifer properties and rain rates to determine the STE flushing times as a function of sediment characteristics.

Finally, it is recommended that geochemical processes in the context of the studied cases be included in future research activities as chemical cycling and fluxes link these dynamic subsurface processes with important biological activities.

REFERENCES

- Abarca, E., and T. Prabhakar Clement (2009), A novel approach for characterizing the mixing zone of a saltwater wedge, *Geophys. Res. Lett.*, 36(6), L06402, doi:10.1029/2008GL036995.
- Abarca, E., J. Carrera, X. Sánchez-Vila, and M. Dentz (2007), Anisotropic dispersive Henry problem, *Adv. Water Resour.*, 30(4), 913–926, doi:10.1016/j.advwatres.2006.08.005.
- Abarca, E., H. Karam, H. F. Hemond, and C. F. Harvey (2013), Transient groundwater dynamics in a coastal aquifer: The effects of tides, the lunar cycle, and the beach profile, *Water Resour. Res.*, 49(5), 2473–2488, doi:10.1002/wrcr.20075.
- Allan, R. P., and B. J. Soden (2008), Atmospheric warming and the amplification of precipitation extremes., *Science*, 321(5895), 1481–1484, doi:10.1126/science.1160787.
- Anderson, M. P. (2005), Heat as a ground water tracer, *Ground Water*, 43(6), 951–968, doi:10.1111/j.1745-6584.2005.00052.x.
- Anderson, W. P., and R. M. Lauer (2008), The role of overwash in the evolution of mixing zone morphology within barrier islands, *Hydrogeol. J.*, 16(8), 1483–1495, doi:10.1007/s10040-008-0340-z.
- Archie, G. E. (1942), The Electrical Resistivity Log as an Aid in Determining Some Reservoir Characteristics, in *Pet. Technol.*, vol. 146, pp. 54–62, Society of Petroleum Engineers.
- Ataie-Ashtiani, B., R. E. Volker, and D. A. Lockington (1999), Tidal effects on sea water intrusion in unconfined aquifers, *J. Hydrol.*, 216(1–2), 17–31, doi:10.1016/S0022-1694(98)00275-3.
- Azanza, R. V., Y. Fukuyo, L. G. Yap, and H. Takayama (2005), *Prorocentrum minimum* bloom and its possible link to a massive fish kill in Bolinao, Pangasinan, Northern Philippines, *Harmful Algae*, 4(3), 519–524, doi:10.1016/j.hal.2004.08.006.
- Badon Ghijben, W. (1889), *Nota in verband met de voorgenomen putboring nabij Amsterdam.*
- Barnett, B., G. Hoxley, and T. Kennedy (2005), Groundwater extraction in the Werribee Irrigation District and the potential for salt water intrusion,

- Bear, J. (2012), *Hydraulics of groundwater*, Courier Dover Publications.
- Befus, K. M., M. B. Cardenas, D. V. Erler, I. R. Santos, and B. D. Eyre (2013), Heat transport dynamics at a sandy intertidal zone, *Water Resour. Res.*, 49(6), 3770–3786, doi:10.1002/wrcr.20325.
- Befus, K. M., M. B. Cardenas, D. R. Tait, and D. V. Erler (2014), Geoelectrical signals of geologic and hydrologic processes in a fringing reef lagoon setting, *J. Hydrol.*, 517, 508–520, doi:10.1016/j.jhydrol.2014.05.070.
- Boano, F., A. Demaria, R. Revelli, and L. Ridolfi (2010), Biogeochemical zonation due to intrameander hyporheic flow, *Water Resour. Res.*, 46(2), doi:10.1029/2008WR007583.
- Boano, F., J. W. Harvey, a. Marion, a. I. Packman, R. Revelli, L. Ridolfi, and a. Wörman (2014), Hyporheic flow and transport processes: Mechanisms, models, and biogeochemical implications, *Rev. Geophys.*, 52, 603–679, doi:10.1002/2012RG000417.
- Boehm, A. B., A. Paytan, G. G. Shellenbarger, and K. a. Davis (2006), Composition and flux of groundwater from a California beach aquifer: Implications for nutrient supply to the surf zone, *Cont. Shelf Res.*, 26(2), 269–282, doi:10.1016/j.csr.2005.11.008.
- Bokuniewicz, H. J. (1980), Groundwater seepage into Great South Bay, New York, *Estuar. Coast. Mar. Sci.*, 10(4), 437–444, doi:10.1016/S0302-3524(80)80122-8.
- Bokuniewicz, H. J. (1992), Analytical Descriptions of Subaqueous Groundwater Seepage, *Estuaries*, 15(4), 458, doi:10.2307/1352390.
- Bokuniewicz, H. J., M. Taniguchi, T. Ishitoibi, M. A. Charette, M. Allen, and E. A. Kontar (2008), Direct measurements of submarine groundwater discharge (SGD) over a fractured rock aquifer in Flamengo Bay Brazil, *Estuar. Coast. Shelf Sci.*, 76(3), 466–472, doi:10.1016/j.ecss.2007.07.047.
- Boufadel, M. C., Y. Xia, and H. Li (2011), Modeling solute transport and transient seepage in a laboratory beach under tidal influence, *Environ. Model. Softw.*, 26(7), 899–912, doi:10.1016/j.envsoft.2011.02.005.
- Bouwer, H., and R. C. Rice (1976), A slug test for determining hydraulic conductivity of unconfined aquifers with completely or partially penetrating wells, *Water Resour. Res.*, 12(3), 423, doi:10.1029/WR012i003p00423.

- Bratton, J. F. (2010), The Three Scales of Submarine Groundwater Flow and Discharge across Passive Continental Margins, *J. Geol.*, *118*(5), 565–575, doi:10.1086/655114.
- Breier, J. A., C. F. Breier, and H. N. Edmonds (2005), Detecting submarine groundwater discharge with synoptic surveys of sediment resistivity, radium, and salinity, *Geophys. Res. Lett.*, *32*(23), 1–4, doi:10.1029/2005GL024639.
- Burnett, W. C., and H. Dulaiova (2003), Estimating the dynamics of groundwater input into the coastal zone via continuous radon-222 measurements, *J. Environ. Radioact.*, *69*(1-2), 21–35, doi:10.1016/S0265-931X(03)00084-5.
- Burnett, W. C., M. Taniguchi, and J. Oberdorfer (2001), Measurement and significance of the direct discharge of groundwater into the coastal zone, *J. Sea Res.*, *46*(2), 109–116, doi:10.1016/S1385-1101(01)00075-2.
- Burnett, W. C., H. J. Bokuniewicz, M. Huettel, W. S. Moore, and M. Taniguchi (2003), Groundwater and pore water inputs to the coastal zone, *Biogeochemistry*, *66*(1), 3–33, doi:10.1023/B:BIOG.0000006066.21240.53.
- Burnett, W. C. et al. (2006), Quantifying submarine groundwater discharge in the coastal zone via multiple methods, *Sci. Total Environ.*, *367*(2-3), 498–543, doi:10.1016/j.scitotenv.2006.05.009.
- Burnett, W. C., R. Peterson, W. S. Moore, and J. de Oliveira (2008), Radon and radium isotopes as tracers of submarine groundwater discharge - Results from the Ubatuba, Brazil SGD assessment intercomparison, *Estuar. Coast. Shelf Sci.*, *76*(3), 501–511, doi:10.1016/j.ecss.2007.07.027.
- Cai, W. et al. (2014), Increasing frequency of extreme El Niño events due to greenhouse warming, *Nat. Clim. Chang.*, *4*(2), 111–116, doi:10.1038/nclimate2100.
- Cardenas, M. B. (2009a), A model for lateral hyporheic flow based on valley slope and channel sinuosity, *Water Resour. Res.*, *45*(1), W01501, doi:10.1029/2008WR007442.
- Cardenas, M. B. (2009b), Stream-aquifer interactions and hyporheic exchange in gaining and losing sinuous streams, *Water Resour. Res.*, *45*(6), doi:10.1029/2008WR007651.
- Cardenas, M. B. (2010), Thermal skin effect of pipes in streambeds and its implications on groundwater flux estimation using diurnal temperature signals, *Water Resour. Res.*, *46*(3), doi:10.1029/2009WR008528.

- Cardenas, M. B., and M. S. Markowski (2011), Geoelectrical imaging of hyporheic exchange and mixing of river water and groundwater in a large regulated river, *Environ. Sci. Technol.*, 45(4), 1407–1411, doi:10.1021/es103438a.
- Cardenas, M. B., and J. L. Wilson (2007a), Exchange across a sediment-water interface with ambient groundwater discharge, *J. Hydrol.*, 346(3-4), 69–80, doi:10.1016/j.jhydrol.2007.08.019.
- Cardenas, M. B., and J. L. Wilson (2007b), Hydrodynamics of coupled flow above and below a sediment-water interface with triangular bedforms, *Adv. Water Resour.*, 30(3), 301–313, doi:10.1016/j.advwatres.2006.06.009.
- Cardenas, M. B., P. B. Zamora, F. P. Siringan, M. R. Lapus, R. S. Rodolfo, G. S. Jacinto, M. L. San Diego-Mcglone, C. L. Villanoy, O. Cabrera, and M. I. Senal (2010), Linking regional sources and pathways for submarine groundwater discharge at a reef by electrical resistivity tomography, 222Rn, and salinity measurements, *Geophys. Res. Lett.*, 37(16), doi:10.1029/2010GL044066.
- Charette, M. A. (2002), Oxidative precipitation of groundwater-derived ferrous iron in the subterranean estuary of a coastal bay, *Geophys. Res. Lett.*, 29(10), 85–1–85–4, doi:10.1029/2001GL014512.
- Charette, M. A., and E. R. Sholkovitz (2006), Trace element cycling in a subterranean estuary: Part 2. Geochemistry of the pore water, *Geochim. Cosmochim. Acta*, 70(4), 811–826, doi:10.1016/j.gca.2005.10.019.
- Charette, M. a., E. R. Sholkovitz, and C. M. Hansel (2005), Trace element cycling in a subterranean estuary: Part 1. Geochemistry of the permeable sediments, *Geochim. Cosmochim. Acta*, 69(8), 2095–2109, doi:10.1016/j.gca.2004.10.024.
- Chui, T. F. M., and D. L. Freyberg (2009), Implementing Hydrologic Boundary Conditions in a Multiphysics Model, *J. Hydrol. Eng.*, 14(12), 1374–1377, doi:10.1061/(ASCE)HE.1943-5584.0000113.
- Coci, M., D. Riechmann, P. L. E. Bodelier, S. Stefani, G. Zwart, and H. J. Laanbroek (2005), Effect of salinity on temporal and spatial dynamics of ammonia-oxidising bacteria from intertidal freshwater sediment, *FEMS Microbiol. Ecol.*, 53(3), 359–368, doi:10.1016/j.femsec.2005.01.016.
- Du Commun, J. (1828), On the cause of fresh water springs, fountains, etc, *Am. J. Sci.*, 14, 174–176.

- Cooper, H. H. (1959), A hypothesis concerning the dynamic balance of fresh water and salt water in a coastal aquifer, *J. Geophys. Res.*, 64(4), 461, doi:10.1029/JZ064i004p00461.
- Coull, B. C. (1999), Role of meiofauna in estuarine soft-bottom habitats, *Aust. J. Ecol.*, 24(4), 327–343, doi:10.1046/j.1442-9993.1999.00979.x.
- Destouni, G., F. Hannerz, C. Prieto, J. Jarsjö, and Y. Shibuo (2008), Small unmonitored near-coastal catchment areas yielding large mass loading to the sea, *Global Biogeochem. Cycles*, 22(4), n/a–n/a, doi:10.1029/2008GB003287.
- Dimova, N. T., P. W. Swarzenski, H. Dulaiova, and C. R. Glenn (2012), Utilizing multichannel electrical resistivity methods to examine the dynamics of the fresh water-seawater interface in two Hawaiian groundwater systems, *J. Geophys. Res. Ocean.*, 117(2), C02012, doi:10.1029/2011JC007509.
- Dudley Williams, D. (2003), The brackishwater hyporheic zone: Invertebrate community structure across a novel ecotone, *Hydrobiologia*, 510(1-3), 153–173, doi:10.1023/B:HYDR.0000008642.64116.8f.
- Dulaiova, H., M. E. Gonneea, P. B. Henderson, and M. A. Charette (2008), Geochemical and physical sources of radon variation in a subterranean estuary - Implications for groundwater radon activities in submarine groundwater discharge studies, *Mar. Chem.*, 110(1-2), 120–127, doi:10.1016/j.marchem.2008.02.011.
- Fleury, P., M. Bakalowicz, and G. de Marsily (2007), Submarine springs and coastal karst aquifers: A review, *J. Hydrol.*, 339(1-2), 79–92, doi:10.1016/j.jhydrol.2007.03.009.
- Gardner, L. R., and A. M. Wilson (2006), Comparison of four numerical models for simulating seepage from salt marsh sediments, *Estuar. Coast. Shelf Sci.*, 69(3-4), 427–437, doi:10.1016/j.ecss.2006.05.009.
- Van Genuchten, M. T. (1980), A Closed-form Equation for Predicting the Hydraulic Conductivity of Unsaturated Soils1, *Soil Sci. Soc. Am. J.*, 44(5), 892, doi:10.2136/sssaj1980.03615995004400050002x.
- Glover, R. E. (1959), The pattern of fresh-water flow in a coastal aquifer, *J. Geophys. Res.*, 64(4), 457, doi:10.1029/JZ064i004p00457.
- Gosink, J. P., and G. C. Baker (1990), Salt fingering in subsea permafrost: Some stability and energy considerations, *J. Geophys. Res.*, 95(C6), 9575, doi:10.1029/JC095iC06p09575.

- Goswami, B. N., V. Venugopal, D. Sengupta, M. S. Madhusoodanan, and P. K. Xavier (2006), Increasing trend of extreme rain events over India in a warming environment., *Science*, 314(5804), 1442–5, doi:10.1126/science.1132027.
- Guo, W., and C. D. Langevin (2002), *User's Guide to SEAWAT: A Computer Program For Simulation of Three-Dimensional Variable-Density Ground-Water Flow: Techniques of Water-Resources Investigations 6-A7*, US Department of the Interior, US Geological Survey.
- Haylock, M., and N. Nicholls (2000), Trends in extreme rainfall indices for an updated high quality data set for Australia, 1910-1998, *Int. J. Climatol.*, 20(13), 1533–1541, doi:10.1002/1097-0088(20001115)20:13<1533::AID-JOC586>3.0.CO;2-J.
- Heiss, J. W., and H. A. Michael (2014), Saltwater-freshwater mixing dynamics in a sandy beach aquifer over tidal, spring-neap, and seasonal cycles, *Water Resour. Res.*, 50(8), n/a–n/a, doi:10.1002/2014WR015574.
- Henderson, R. D., F. D. Day-Lewis, E. Abarca, C. F. Harvey, H. N. Karam, L. Liu, and J. W. Lane (2010), Marine electrical resistivity imaging of submarine groundwater discharge: sensitivity analysis and application in Waquoit Bay, Massachusetts, USA, *Hydrogeol. J.*, 18(1), 173–185, doi:10.1007/s10040-009-0498-z.
- Herzberg, D. (1901), *Die wasserversorgung einiger nordseebäder*.
- Holliday, D., T. C. Stieglitz, P. V. Ridd, and W. W. Read (2007), Geological controls and tidal forcing of submarine groundwater discharge from a confined aquifer in a coastal sand dune system, *J. Geophys. Res. Ocean.*, 112(C4), C04015, doi:10.1029/2006JC003580.
- Hu, C., F. E. Muller-Karger, and P. W. Swarzenski (2006), Hurricanes, submarine groundwater discharge, and Florida's red tides, *Geophys. Res. Lett.*, 33(11), doi:10.1029/2005GL025449.
- Hubbert, M. K. (1940), The Theory of Ground-Water Motion, *J. Geol.*, 48(8), 785–944, doi:10.2307/30057101.
- Hwang, D.-W., Y.-W. Lee, and G. Kim (2005), Large submarine groundwater discharge and benthic eutrophication in Bangdu Bay on volcanic Jeju Island, Korea, *Limnol. Oceanogr.*, 50(5), 1393–1403, doi:10.4319/lo.2005.50.5.1393.
- Ii, H., A. Satoh, M. Taniguchi, M. Kitching, G. Croatto, B. Shelley, and G. Allinson (2012), Groundwater Contamination Due to Irrigation of Treated Sewage Effluent in

the Werribee Delta, *Int. J. GEOMATE Geotech. Constr. Mater. Environ.*, 3(1), 332–338.

- Jiang, R., K. P. Woli, K. Kuramochi, A. Hayakawa, M. Shimizu, and R. Hatano (2010), Hydrological process controls on nitrogen export during storm events in an agricultural watershed, *Soil Sci. Plant Nutr.*, 56(1), 72–85, doi:10.1111/j.1747-0765.2010.00456.x.
- Johannes, R. (1980), The Ecological Significance of the Submarine Discharge of Groundwater, *Mar. Ecol. Prog. Ser.*, 3(4), 365–373, doi:10.3354/meps003365.
- Jones, I. C., and J. L. Banner (2003a), Estimating recharge thresholds in tropical karst island aquifers: Barbados, Puerto Rico and Guam, *J. Hydrol.*, 278(1-4), 131–143, doi:10.1016/S0022-1694(03)00138-0.
- Jones, I. C., and J. L. Banner (2003b), Hydrogeologic and climatic influences on spatial and interannual variation of recharge to a tropical karst island aquifer, *Water Resour. Res.*, 39(9), 1253, doi:10.1029/2002WR001543.
- Jones, I. C., J. L. Banner, and J. D. Humphrey (2000), Estimating recharge in a tropical karst aquifer, *Water Resour. Res.*, 36(5), 1289–1299, doi:10.1029/1999WR900358.
- Kessler, A. J., R. N. Glud, M. B. Cardenas, and P. L. M. Cook (2013), Transport zonation limits coupled nitrification-denitrification in permeable sediments, *Environ. Sci. Technol.*, 47(23), 13404–13411, doi:10.1021/es403318x.
- Kim, G. (2003), Large submarine groundwater discharge (SGD) from a volcanic island, *Geophys. Res. Lett.*, 30(21), 2098, doi:10.1029/2003GL018378.
- King, J. N., a. J. Mehta, and R. G. Dean (2009), Generalized analytical model for benthic water flux forced by surface gravity waves, *J. Geophys. Res. Ocean.*, 114(C4), doi:10.1029/2008JC005116.
- Kohout, F. a. (1960), Cyclic flow of salt water in the Biscayne aquifer of southeastern Florida, *J. Geophys. Res.*, 65(7), 2133, doi:10.1029/JZ065i007p02133.
- Konikow, L. F., M. Akhavan, C. D. Langevin, H. A. Michael, and A. H. Sawyer (2013), Seawater circulation in sediments driven by interactions between seabed topography and fluid density, *Water Resour. Res.*, 49, 1386–1399, doi:10.1002/wrcr.20121.
- Kroeger, K. D., M. L. Cole, J. K. York, and I. Valiela (2006), Nitrogen loads to estuaries from waste water plumes: Modeling and isotopic approaches, *Ground Water*, 44(2), 188–200, doi:10.1111/j.1745-6584.2005.00130.x.

- Kroeger, K. D., P. W. Swarzenski, W. J. Greenwood, and C. Reich (2007), Submarine groundwater discharge to Tampa Bay: Nutrient fluxes and biogeochemistry of the coastal aquifer, *Mar. Chem.*, 104(1-2), 85–97, doi:10.1016/j.marchem.2006.10.012.
- Lambert, M. J., and W. C. Burnett (2003), Submarine groundwater discharge estimates at a Florida coastal site based on continuous radon measurements, *Biogeochemistry*, 66(1-2), 55–73, doi:10.1023/B: BIOG.0000006057.63478.fa.
- Lapointe, B. E., and W. R. Matzie (1996), Effects of Stormwater Nutrient Discharges on Eutrophication Processes in Nearshore Waters of the Florida Keys, *Estuaries*, 19(2), 422, doi:10.2307/1352460.
- Lapointe, B. E., J. D. O’Connell, and G. S. Garrett (1990), Nutrient couplings between on-site sewage disposal systems, groundwaters, and nearshore surface waters of the Florida Keys, *Biogeochemistry*, 10(3), 289–307, doi:10.1007/BF00003149.
- Lee, D. R. (1977), A device for measuring seepage flux in lakes and estuaries, *Limnol. Oceanogr.*, 22(1), 140–147, doi:10.4319/lo.1977.22.1.0140.
- Lenkopane, M., A. D. Werner, D. a. Lockington, and L. Li (2009), Influence of variable salinity conditions in a tidal creek on riparian groundwater flow and salinity dynamics, *J. Hydrol.*, 375(3-4), 536–545, doi:10.1016/j.jhydrol.2009.07.004.
- Li, H., M. C. Boufadel, and J. W. Weaver (2008), Tide-induced seawater-groundwater circulation in shallow beach aquifers, *J. Hydrol.*, 352(1-2), 211–224, doi:10.1016/j.jhydrol.2008.01.013.
- Linderfelt, W. R., and J. V. Turner (2001), Interaction between shallow groundwater, saline surface water and nutrient discharge in a seasonal estuary: The Swan - Canning system, *Hydrol. Process.*, 15(13), 2631–2653, doi:10.1002/hyp.302.
- Lloyd, L. N., B. G. Anderson, M. Cooling, C. J. Gippel, A. J. Pope, and J. E. Sherwood (2008), *Environmental Water Requirements of the Werribee River Estuary Final Estuary FLOWs Report*, Syndal, Vic.
- Lofi, J., P. Pezard, F. Bouchette, O. Raynal, P. Sabatier, N. Denchik, A. Levannier, L. Dezileau, and R. Certain (2013), Integrated onshore-offshore investigation of a mediterranean layered coastal aquifer, *Groundwater*, 51(4), 550–561, doi:10.1111/j.1745-6584.2012.01011.x.
- Loke, M. H. (1999), RES2DMOD version 2.2: rapid 2-D resistivity forward modeling using the finite-difference and finite-element methods,

- Loke, M. H., and R. D. Barker (1996), Rapid least-squares inversion of apparent resistivity pseudosections by a quasi-Newton method1, *Geophys. Prospect.*, 44(1), 131–152, doi:10.1111/j.1365-2478.1996.tb00142.x.
- Loveless, A. M., and C. E. Oldham (2010), Natural attenuation of nitrogen in groundwater discharging through a sandy beach, *Biogeochemistry*, 98(1-3), 75–87, doi:10.1007/s10533-009-9377-x.
- Lu, C., P. K. Kitanidis, and J. Luo (2009), Effects of kinetic mass transfer and transient flow conditions on widening mixing zones in coastal aquifers, *Water Resour. Res.*, 45(12), W12402, doi:10.1029/2008WR007643.
- Maemoku, H., and J. Paladio (1992), Raised coral reefs at Bolinao, northwestern Luzon, Island of the Philippines, *Geogr. Sci. (Chiri Kagaku)*, 47(4), 183–189.
- Mälkki, E. (2003), Groundwater flow conditions in the coastal bedrock area of the Gulf of Finland, *Geol. Q.*, 47(3), 299–306.
- Manheim, F. T., D. E. Krantz, and J. F. Bratton (2004), Studying ground water under delmarva coastal bays using electrical resistivity, *Ground Water*, 42(7), 1052–1068, doi:10.1111/j.1745-6584.2004.tb02643.x.
- McManus, J. W. (1997), Tropical marine fisheries and the future of coral reefs: a brief review with emphasis on Southeast Asia, *Coral Reefs*, 16(1), S121–S127, doi:10.1007/s003380050248.
- MGB (1974), *The Geology and Mineral Resources of Pangasinan Province*, Bureau of Mines. Philippines, Manila, Philippines.
- Michael, H. A., A. E. Mulligan, and C. F. Harvey (2005), Seasonal oscillations in water exchange between aquifers and the coastal ocean., *Nature*, 436(7054), 1145–1148, doi:10.1038/nature03935.
- Moore, W. S. (1996), Large groundwater inputs to coastal waters revealed by 226Ra enrichments, *Nature*, 380(6575), 612–614, doi:10.1038/380612a0.
- Moore, W. S. (1999), The subterranean estuary: A reaction zone of ground water and sea water, *Mar. Chem.*, 65(1-2), 111–125, doi:10.1016/S0304-4203(99)00014-6.
- Moore, W. S., and A. M. Wilson (2005), Advective flow through the upper continental shelf driven by storms, buoyancy, and submarine groundwater discharge, *Earth Planet. Sci. Lett.*, 235(3-4), 564–576, doi:10.1016/j.epsl.2005.04.043.

- Mulligan, A. E., R. L. Evans, and D. Lizarralde (2007), The role of paleochannels in groundwater/seawater exchange, *J. Hydrol.*, 335(3–4), 313–329, doi:10.1016/j.jhydrol.2006.11.025.
- Nidzieko, N. J., J. L. Hench, and S. G. Monismith (2009), Lateral Circulation in Well-Mixed and Stratified Estuarine Flows with Curvature, *J. Phys. Oceanogr.*, 39(4), 831–851, doi:10.1175/2008JPO4017.1.
- Null, K. a., K. L. Knee, E. D. Crook, N. R. de Sieyes, M. Rebolledo-Vieyra, L. Hernández-Terrones, and A. Paytan (2014), Composition and fluxes of submarine groundwater along the Caribbean coast of the Yucatan Peninsula, *Cont. Shelf Res.*, 77(0), 38–50, doi:10.1016/j.csr.2014.01.011.
- De Ocampo, R. S. P. (1983), Plio-Pleistocene geology of Bolinao, Pangasinan and vicinities,
- Peng, T. R., C. T. A. Chen, C. H. Wang, J. Zhang, and Y. J. Lin (2008), Assessment of terrestrial factors controlling the submarine groundwater discharge in water shortage and highly deformed Island of Taiwan, Western Pacific Ocean, *J. Oceanogr.*, 64(2), 323–337, doi:10.1007/s10872-008-0026-0.
- Peterson, R. N., W. C. Burnett, C. R. Glenn, and A. G. Johnson (2009), Quantification of point-source groundwater discharges to the ocean from the shoreline of the Big Island, Hawaii, *Limnol. Oceanogr.*, 54(3), 890–904, doi:10.4319/lo.2009.54.3.0890.
- Povinec, P. P. et al. (2012), Isotopic, geophysical and biogeochemical investigation of submarine groundwater discharge: IAEA-UNESCO intercomparison exercise at Mauritius Island, *J. Environ. Radioact.*, 104, 24–45, doi:10.1016/j.jenvrad.2011.09.009.
- Ramessur, R. T., K. Boodhoo, J. Balgobin, P. Povinec, and W. C. Burnett (2013), Dissolved Nutrients from Submarine Groundwater in Flic en Flac Lagoon, Mauritius, *West. Indian Ocean J. Mar. Sci.*, 10(2), 121–127.
- Ramos, N. T., and H. Tsutsumi (2010), Evidence of large prehistoric offshore earthquakes deduced from uplifted Holocene marine terraces in Pangasinan Province, Luzon Island, Philippines, *Tectonophysics*, 495(3-4), 145–158, doi:10.1016/j.tecto.2010.08.007.
- Reeves, H. W., P. M. Thibodeau, R. G. Underwood, and L. R. Gardner (2000), Incorporation of Total Stress Changes into the Ground Water Model SUTRA, *Ground Water*, 38(1), 89–98, doi:10.1111/j.1745-6584.2000.tb00205.x.

- Rivera, P. C. (1997), Hydrodynamics, Sediment Transport and Light Extinction Off Cape Bolinao, Philippines.
- Robinson, C., B. Gibbes, and L. Li (2006), Driving mechanisms for groundwater flow and salt transport in a subterranean estuary, *Geophys. Res. Lett.*, *33*(3), doi:10.1029/2005GL025247.
- Robinson, C., L. Li, and D. A. Barry (2007a), Effect of tidal forcing on a subterranean estuary, *Adv. Water Resour.*, *30*(12), 851–865, doi:10.1016/j.advwatres.2006.07.006.
- Robinson, C., B. Gibbes, H. Carey, and L. Li (2007b), Salt-freshwater dynamics in a subterranean estuary over a spring-neap tidal cycle, *J. Geophys. Res. Ocean.*, *112*(C9), doi:10.1029/2006JC003888.
- Robinson, C., L. Li, and H. Prommer (2007c), Tide-induced recirculation across the aquifer-ocean interface, *Water Resour. Res.*, *43*(7), doi:10.1029/2006WR005679.
- Robinson, M. A., and D. L. Gallagher (1999), A Model of Ground Water Discharge from an Unconfined Coastal Aquifer, *Ground Water*, *37*(1), 80–87, doi:10.1111/j.1745-6584.1999.tb00960.x.
- Robinson, M. A., D. L. Gallagher, and W. Reay (1998), Field Observations of Tidal and Seasonal Variations in Ground Water Discharge to Tidal Estuarine Surface Water, *Ground Water Monit. Remediat.*, *18*(1), 83–92, doi:10.1111/j.1745-6592.1998.tb00605.x.
- Rollón, R. N., E. D. De Ruyter Van Steveninck, and W. Van Vierssen (2003), Spatio-temporal variation in sexual reproduction of the tropical seagrass *Enhalus acoroides* (L.f.) Royle in Cape Bolinao, NW Philippines, *Aquat. Bot.*, *76*(4), 339–354, doi:10.1016/S0304-3770(03)00070-6.
- Russoniello, C. J., C. Fernandez, J. F. Bratton, J. F. Banaszak, D. E. Krantz, A. S. Andres, L. F. Konikow, and H. A. Michael (2013), Geologic effects on groundwater salinity and discharge into an estuary, *J. Hydrol.*, *498*(0), 1–12, doi:10.1016/j.jhydrol.2013.05.049.
- Sahan, E., and G. Muyzer (2008), Diversity and spatio-temporal distribution of ammonia-oxidizing Archaea and Bacteria in sediments of the Westerschelde estuary, *FEMS Microbiol. Ecol.*, *64*(2), 175–186, doi:10.1111/j.1574-6941.2008.00462.x.
- Salzman, S. (2010), The deltaic aquifer of the Werribee irrigation district (WID), , doi:http://dro.deakin.edu.au/view/DU:30036670.

- San Diego-McGlone, M. L., R. V. Azanza, C. L. Villanoy, and G. S. Jacinto (2008), Eutrophic waters, algal bloom and fish kill in fish farming areas in Bolinao, Pangasinan, Philippines, *Mar. Pollut. Bull.*, 57(6-12), 295–301, doi:10.1016/j.marpolbul.2008.03.028.
- Santoro, A. E. (2010), Microbial nitrogen cycling at the saltwater–freshwater interface, *Hydrogeol. J.*, 18(1), 187–202, doi:10.1007/s10040-009-0526-z.
- Santos, I. R., W. C. Burnett, J. Chanton, N. Dimova, and R. N. Peterson (2009), Land or ocean?: Assessing the driving forces of submarine groundwater discharge at a coastal site in the gulf of mexico, *J. Geophys. Res. Ocean.*, 114(C4), doi:10.1029/2008JC005038.
- Santos, I. R., P. L. M. Cook, L. Rogers, J. de Weys, and B. D. Eyre (2012a), The salt wedge pump: Convection-driven pore-water exchange as a source of dissolved organic and inorganic carbon and nitrogen to an estuary, *Limnol. Oceanogr.*, 57(5), 1415–1426, doi:10.4319/lo.2012.57.5.1415.
- Santos, I. R., B. D. Eyre, and M. Huettel (2012b), The driving forces of porewater and groundwater flow in permeable coastal sediments: A review, *Estuar. Coast. Shelf Sci.*, 98(0), 1–15, doi:10.1016/j.ecss.2011.10.024.
- Santos, I. R., J. de Weys, D. R. Tait, and B. D. Eyre (2013), The Contribution of Groundwater Discharge to Nutrient Exports from a Coastal Catchment: Post-Flood Seepage Increases Estuarine N/P Ratios, *Estuaries and Coasts*, 36(1), 56–73, doi:10.1007/s12237-012-9561-4.
- Sawyer, A. H., M. B. Cardenas, and J. Buttles (2011), Hyporheic exchange due to channel-spanning logs, *Water Resour. Res.*, 47(8), doi:10.1029/2011WR010484.
- Sawyer, A. H., L. A. Kaplan, O. Lazareva, and H. A. Michael (2014), Hydrologic dynamics and geochemical responses within a floodplain aquifer and hyporheic zone during Hurricane Sandy, *Water Resour. Res.*, 50(6), 4877–4892, doi:10.1002/2013WR015101.
- Schaap, M. G., F. J. Leij, and M. T. Van Genuchten (2001), Rosetta: A computer program for estimating soil hydraulic parameters with hierarchical pedotransfer functions, *J. Hydrol.*, 251(3), 163–176, doi:10.1016/S0022-1694(01)00466-8.
- Senal, M. I. S., G. S. Jacinto, M. L. San Diego-McGlone, F. Siringan, P. B. Zamora, L. Soria, M. B. Cardenas, C. L. Villanoy, and O. Cabrera (2011), Nutrient inputs from submarine groundwater discharge on the Santiago reef flat, Bolinao, Northwestern

Philippines, *Mar. Pollut. Bull.*, 63(5-12), 195–200,
doi:10.1016/j.marpolbul.2011.05.037.

Shaban, A., M. Khawlie, C. Abdallah, and G. Faour (2005), Geologic controls of submarine groundwater discharge: Application of remote sensing to north Lebanon, *Environ. Geol.*, 47(4), 512–522, doi:10.1007/s00254-004-1172-3.

Slomp, C. P., and P. Van Cappellen (2004), Nutrient inputs to the coastal ocean through submarine groundwater discharge: Controls and potential impact, *J. Hydrol.*, 295(1-4), 64–86, doi:10.1016/j.jhydrol.2004.02.018.

Smith, A. J., and J. V. Turner (2001), Density-dependent surface water-groundwater interaction and nutrient discharge in the Swan - Canning estuary, *Hydrol. Process.*, 15(13), 2595–2616, doi:10.1002/hyp.303.

Smith, C. G., J. E. Cable, and J. B. Martin (2008), Episodic high intensity mixing events in a subterranean estuary: Effects of tropical cyclones, *Limnol. Oceanogr.*, 53(2), 666–674, doi:10.4319/lo.2008.53.2.0666.

Sonrel, L. (1886), *Le fond de la mer*, Biblioth que des merveilles, Hachette, Paris.

Springer, R. K., and L. W. Gelhar (1991), *Characterization of large-scale aquifer heterogeneity in glacial outwash by analysis of slug tests with oscillatory response*, Cape Cod, Massachusetts.

Stieglitz, T. (2005), Submarine groundwater discharge into the near-shore zone of the Great Barrier Reef, Australia, *Mar. Pollut. Bull.*, 51(1–4), 51–59,
doi:10.1016/j.marpolbul.2004.10.055.

Stieglitz, T., M. Taniguchi, and S. Neylon (2008), Spatial variability of submarine groundwater discharge, Ubatuba, Brazil, *Estuar. Coast. Shelf Sci.*, 76(3), 493–500,
doi:10.1016/j.ecss.2007.07.038.

Swarzenski, P. W., and J. A. Izbicki (2009), Coastal groundwater dynamics off Santa Barbara, California: Combining geochemical tracers, electromagnetic seepmeters, and electrical resistivity, *Estuar. Coast. Shelf Sci.*, 83(1), 77–89,
doi:10.1016/j.ecss.2009.03.027.

Swarzenski, P. W., W. C. Burnett, W. J. Greenwood, B. Herut, R. Peterson, N. Dimova, Y. Shalem, Y. Yechieli, and Y. Weinstein (2006), Combined time-series resistivity and geochemical tracer techniques to examine submarine groundwater discharge at Dor Beach, Israel, *Geophys. Res. Lett.*, 33(24), doi:10.1029/2006GL028282.

- Taniguchi, M., W. C. Burnett, H. Dulaiova, F. Siringan, J. Foronda, G. Wattayakorn, S. Rungsupa, E. a. Kontar, and T. Ishitobi (2008), Groundwater Discharge as an Important Land-Sea Pathway into Manila Bay, Philippines, *J. Coast. Res.*, *24*, 15–24, doi:10.2112/06-0636.1.
- Turner, S. M., G. Malin, P. D. Nightingale, and P. S. Liss (1996), Seasonal variation of dimethyl sulphide in the North Sea and an assessment of fluxes to the atmosphere, *Mar. Chem.*, *54*(3), 245–262, doi:10.1016/0304-4203(96)00028-X.
- Underwood, G., J. Phillips, and K. Saunders (1998), Distribution of estuarine benthic diatom species along salinity and nutrient gradients, *Eur. J. Phycol.*, *33*(2), 173–183, doi:10.1080/09670269810001736673.
- Volker, R. E., and K. R. Rushton (1982), An assessment of the importance of some parameters for seawater intrusion in aquifers and a comparison of dispersive and sharp-interface modelling approaches, *J. Hydrol.*, *56*(3), 239–250, doi:10.1016/0022-1694(82)90015-4.
- Ward, A. S., M. N. Gooseff, and K. Singha (2010), Imaging hyporheic zone solute transport using electrical resistivity, *Hydrol. Process.*, *24*(7), 948–953, doi:10.1002/hyp.7672.
- Webster, I. T., S. J. Norquay, F. C. Ross, and R. a. Wooding (1996), Solute Exchange by Convection Within Estuarine Sediments, *Estuar. Coast. Shelf Sci.*, *42*(2), 171–183, doi:10.1006/ecss.1996.0013.
- Wentworth, C. K. (1948), Growth of the Ghyben-Herzberg transition zone under a rinsing hypothesis, *Eos, Trans. Am. Geophys. Union*, *29*(1), 97–98.
- Werner, A. D., and D. a. Lockington (2006), Tidal impacts on riparian salinities near estuaries, *J. Hydrol.*, *328*(3-4), 511–522, doi:10.1016/j.jhydrol.2005.12.011.
- Westbrook, S. J., J. L. Rayner, G. B. Davis, T. P. Clement, P. L. Bjerg, and S. J. Fisher (2005), Interaction between shallow groundwater, saline surface water and contaminant discharge at a seasonally and tidally forced estuarine boundary, *J. Hydrol.*, *302*(1–4), 255–269, doi:10.1016/j.jhydrol.2004.07.007.
- De Weys, J., I. R. Santos, and B. D. Eyre (2011), Linking groundwater discharge to severe estuarine acidification during a flood in a modified wetland, *Environ. Sci. Technol.*, *45*(8), 3310–3316, doi:10.1021/es104071r.

- Wilson, A. M., and L. R. Gardner (2006), Tidally driven groundwater flow and solute exchange in a marsh: Numerical simulations, *Water Resour. Res.*, 42(1), doi:10.1029/2005WR004302.
- Wilson, A. M., W. S. Moore, S. B. Joye, J. L. Anderson, and C. A. Schutte (2011), Storm-driven groundwater flow in a salt marsh, *Water Resour. Res.*, 47(2), doi:10.1029/2010WR009496.
- Wong, W. W., M. R. Grace, I. Cartwright, M. B. Cardenas, P. B. Zamora, and P. L. M. Cook (2013), Dynamics of groundwater-derived nitrate and nitrous oxide in a tidal estuary from radon mass balance modeling, *Limnol. Oceanogr.*, 58(5), 1689–1706, doi:10.4319/lo.2013.58.5.1689.
- Zhai, P., X. Zhang, H. Wan, and X. Pan (2005), Trends in total precipitation and frequency of daily precipitation extremes over China, *J. Clim.*, 18(7), 1096–1108, doi:10.1175/JCLI-3318.1.